NATIONAL TECHNICAL UNIVERSITY OF ATHENS
SCHOOL OF NAVAL ARCHITECTURE & MARINE ENGINEERING

APPLICATION OF CONTROL METHODS TO FLUID MECHANICS PROBLEMS: FLOW PAST A CYLINDER

A THESIS
for the Degree of
Doctor of Philosophy

Presented by
MARIOS E. MASTROKALOS
(Dipl. Naval Architect & Marine Engineer N.T.U.A.)

Born 24.06.1981
Citizen of Greece

PhD Advisory Committee
L. Kaiktsis, Associate Professor N.T.U.A. (Supervisor)
C.I. Papadopoulos, Assistant Professor N.T.U.A.
G.S. Triantafyllou Professor N.T.U.A.

PhD Examination Comittee
L. Kaiktsis, Associate Professor N.T.U.A. (Supervisor)
C.I. Papadopoulos, Assistant Professor N.T.U.A.
G.S. Triantafyllou Professor N.T.U.A.
E. Konstantinidis, Associate Professor U.W.M.
P. Koumoutsakos, Professor ETH Zurich
G. Papalambrou, Assistant Professor N.T.U.A.
G. Tzabiras, Professor N.T.U.A.

2016

Για τον Μανώλη τον Δάσκαλο

Abstract

The optimal suppression of the Kármán vortex street in flow past a circular cylinder, by use of either, passive, active open-loop or active feedback control schemes is investigated by coupling a CFD solver with an optimization tool. The control action consists of either application of slip conditions or mass transpiration on the cylinder surface. The results are interepreted by means of local and global instability calculations utilizing an Orr-Sommerfeld solver and signal processing based on the Stuart-Landau model, respectively. The study is limited to two-dimensional flow at low Reynolds numbers, $Re<180$, where the non-manipulated flow is either steady or characterized by vortex shedding.

Firstly, steady slip conditions are applied on a part or on the entire cylinder surface utilizing a passive control scheme. For slip conditions applied on the entire cylinder surface, the present results demonstrate the stabilizing effect of increasing the non-dimensional slip length, $b^*=b/D$, b being the slip length and D the cylinder diameter, in agreement with recent studies. In particular, the Kármán vortex street is supressed at a critical value of b^*, which is an increasing function of Re. Further, it is shown that, for the same levels of b^*, the wake can be stabilized by implementing slip conditions only on a part of the cylinder surface. Guided by this observation, the problem of fully or partially suppressing the Kármán vortex street by means of a partially hydrophobic cylinder is addressed by formulating a multi-objective optimization problem, in which the product of slip length and hydrophobic area quantifies the control effort; a second objective function, characterizing flow unsteadiness, is thereby introduced. The optimization results demonstrate that, both for full and partial suppression of the Kármán vortex street, a proper use of partial hydrophobicity can lead to a significant reduction in passive control effort, in comparison to the case of the fully hydrophobic cylinder. Computed optimal solutions of the Pareto front are characterized by means of local stability calculations based on an Orr-Sommerfeld solver. It is shown that flow stabilization is attained when a global intensity of absolute instability, involving local absolute growth rates and the streamwise extent of absolute instability, is sufficiently reduced. Further characterization of the flow stability is performed by means of transient lift coefficient signal analysis in the frame of the Stuart-Landau equation.

Secondly, steady mass transpiration is introduced on the cylinder surface. Three regimes on the cylinder surface are considered: (a) the front stagnation point region, (b) the rear stagnation point region, and (c) the region in-between. First, parametric studies are performed, by introducing suction or blowing on each of the three regimes, and assessing the effects on the global stability of the flow. Guided by these results, a multi-objective optimization problem is formulated, aiming at the partial or full suppression of the Kármán vortex street, at a minimal control effort. In this setup, blowing is applied on the rear stagnation point regime, while suction velocities of different magnitude are considered for the front stagnation point and the sideway regimes. A zero net transpiration flow rate is imposed. The absolute value of suction/blowing flow rate quantifies the control effort, while a second objective function, characterizing flow unsteadiness, is also introduced. The goal of optimization is to find proper combinations of the extent of the three regimes, as well as the corresponding suction/blowing velocities, which minimize simultaneously the two objective functions. The calculation of the optimal flow fields demonstrates that flow stabilization can be attained with a control effort substantially lower in comparison to previous literature studies. Optimal solutions are characterized by means of local stability analysis, as well as analysis of transient lift signals.

Finally, in order to attain partial or complete vortex street cancellation, by even lower levels of control effort, two proportional feedback control schemes are developed, utilizing both control actions introduced above. In the first feedback control scheme, actuation consists in time-dependent mass transpiration, while, in the second one, in time-dependent slip conditions. In both cases, the feedback signal is generated based on a velocity measurement in the near wake. Further, for both feedback control schemes, optimization problems are developed, aiming at the partial or full cancelation of the vortex street at a minimal control effort. In comparison to passive flow control, a reduction in control effort by two orders of magnitude is attained with the present optimized feedback control schemes.

Acknowledgments

First of all I would like to express my warm, sincere and deep thanks to my advisor, Associate Professor L. Kaiktsis, for the invaluable support he provided me up to the completion of my PhD studies. A collaborative relationship of teaching, partnering and encouragement has allowed me to achieve the level of knowledge required to accomplish my goals. I consider an honour for the National Technical University of Athens to have Professor Kaiktsis. He enables students to benefit from his experience and expertise, not only in their profession but also in life.

Furthermore, my gratitude is also extended to the other two members of the advisory committee, Professor G.S. Triantafyllou and Assistant Professor C.I. Papadopoulos, as well as to Associate Professor J. Prousalidis of the Department of Naval Architecture and Marine Engineering of N.T.U.A., for their substantial support and for fruitfull discussions. I would also like to express my special thanks to the other four members of the examination committee, Professor P. Koumoutsakos of ETH Zurich, Associate Professor E. Konstantinidis of the University of Western Macedonia, and Professor G. Tsabiras and Assistant Professor G. Papalambrou of the Department of Naval Architecture and Marine Engineering of N.T.U.A.

Many thanks go to D. Kazangas, P. Kontoulis, A. Charitopoulos, Dr. K. Aivalis and Dr. D. Fouflias, for their help and friendship during these five memorable years. I am more than grateful to my friends and to the people of my family. More precisely, to my friends D. Katsiopis, J. Gouzouasis and J. Kagiaftakis, to my cousin and friend A. Arapis, to Vasso, who is present patiently beside me, and to my mother Electra for her moral support during all the years of my studies. The present work is dedicated to my father Manolis, teacher of Mathematics, who passed away last January, for all the things he taught me and for contributing to what I am.

Contents

Chapter 1: Cylinder wake control problem 1

- 1.1 Bluff body flows and applications 1
- 1.2 Flow past a circular cylinder 1
- 1.3 Optimization concepts 2
- 1.4 Hydrodynamic instability concepts 5
  - 1.4.1 Local instability 6
  - 1.4.2 Global instability 11
- 1.5 Flow control: application to flow past a cylinder 13
- 1.6 Flow control methods implemented in the present study 14

Chapter 2 : Computational approach 17

- 2.1 Problem formulation 17
- 2.2 Resolution tests 20
  - 2.2.1 Mesh generation – spatial resolution tests 20
  - 2.2.2 Temporal resolution tests 22
- 2.3 Validation tests 23
- 2.4 Summary of Chapter 2 25

Chapter 3: Implementation of surface hydrophobicity 27

- 3.1 Application of slip on the entire cylinder surface 27
- 3.2 Application of slip on part of the cylinder surface 31
- 3.3 Flow past a partially hydrophobic cylinder: formulation and solution of optimization problem 34
  - 3.3.1 Design variables and search space 34
  - 3.3.2 Objective functions 34
  - 3.3.3 Optimization problem 35
  - 3.3.4 Optimization methods 35
  - 3.3.5. Optimization results 37
- 3.4 Characterization of flow instability 44
- 3.5 Summary of chapter 3 47

Chapter 4: Flow control by means of mass transpiration 49

- 4.1. Implementation of piecewise uniform suction/blowing 49
  - 4.1.1 Application of suction and blowing on the front stagnation point region, $0^o<\theta<40^o$ 51
  - 4.1.2 Application of suction and blowing on the sideway region, $40^o<\theta<150^o$ 55
  - 4.1.3 Application of suction and blowing on the rear stagnation point region, $150^o<\theta<180^o$ 58
- 4.2 Formulation of optimization problem with piecewise uniform suction/blowing profile 63

4.2.1 Design variables and search space 64
4.2.2 Objective functions 65
4.2.3 Optimization process 65
4.2.4 Optimization results 66
4.2.5 Optimal solutions: characterization of flow instability 75
4.4 Summary of chapter 4 78
Chapter 5: Feedback flow control: optimization of control schemes 79
5.1 Feedback control using mass transpiration: validation test 79
5.2 Optimization of feedback control with time-dependent mass transpiration 81
5.2.1 Design variables and search space 82
5.2.2 Objective functions 82
5.2.3 Optimization problem 82
5.2.4 Optimization results 83
5.3 Feedback control utilizing time-dependent slip conditions 86
5.3.1 Proportional control concept utilizing controllable wetting properties 86
5.3.2 Application of controllable wettability on the entire cylinder surface 87
5.4 Optimization of feedback control with time-dependent slip 92
5.4.1 Design variables and search space 93
5.4.2 Objective functions 93
5.4.3 Optimization problem 93
5.4.4 Optimization results 94
5.5 Summary of chapter 5 97
Chapter 6: Novelty of the present work and contribution to scientific research 99
6.1 Proposed methodology 99
6.2 New findings of the present thesis 100
Chapter 7: Conclusions 101
7.1 Conclusions 101
7.2 Suggestions for future work 102
Appendix A: Validation tests of instability analysis calculations 105
A.1 Local linear instability analysis calculations 105
A.2 Calculations of global linear growth rates 106
References 107

List of Figures

1. Fig. 1. Sketch of Pareto front for a minimization problem with two objective functions. 3
2. Fig. 2. Operations of: (a) crossover and (b) mutation. 4
3. Fig. 3. Evolutionary algorithm outline. 5
4. Fig. 4. Sketch of spatio-temporal evolution of a perturbation in a parallel flow: (a) absolutely unstable flow and (b) convectively unstable flow. Flow direction: left to right 6
5. Fig. 5. (a) Cylinder wake profiles of the family described by eq. (6) for N=100 (top-hat profile) and N=2 (parabolic profile), and (b) absolute and convective instability regions as a function of the wake velocity profile parameters, R, $1/N$ (Monkewitz 1988). 7
6. Fig. 6. Base flow past a circular cylinder, at Re=90: (a) iso-contours of streamwise velocity, U, (b) streamwise velocity profile at x/D=2, and corresponding Orr–Sommerfeld eigenvalues in terms of isocontours of (c) ω_r and (d) ω_i, in the complex wavenumber plane. Here, $\omega_0 = 0.762 + 0.195 \cdot i$, corresponding to absolute instability. 10
7. Fig. 7. Re=60, uncontrolled flow past a circular cylinder: (a) Computed lift coefficient signal, C_L(t), (b) Lift coefficient magnitude versus time, $|C_L(t)|$, and (c) semi-log plot of lift coefficient versus time, $\log_{10}|C_L(t)|$. Here, σ_r=0.04137, St_g=0.121. 13
8. Fig. 8. Sketch of the flow domain. 18
9. Fig. 9. Definition of slip length, b, in flow past a hydrophobic surface. 19
10. Fig. 10. (a) Application of slip on the entire cylinder surface: sketch of velocity profile near the cylinder, for a slip length b. (b) Application of slip on an arc lying between θ_{min} and θ_{max}. 19
11. Fig. 11. (a) Application of blowing on a part of the cylinder surface, (b) application of suction on a part of the cylinder surface and blowing on the remaining part. 20
12. Fig. 12. Decomposition of the flow domain into three, five and eleven sub-domains. 21
13. Fig. 13. Detail of a finite volume mesh close to the cylinder (the number of finite volumes osculating to cylinder surface is close to 100). 21
14. Fig. 14. Spatial resolution tests for uncontrolled flow at Re=90. Computed values of force coefficients: (a) time-averaged drag coefficient, (b) drag coefficient amplitude, and (c) lift coefficient amplitude, versus the number of finite volumes, N. A time step value of Δt=0.01 is utilized. 22
15. Fig. 15. Temporal resolution tests for uncontrolled flow at Re=90. Computed values of force coefficients: (a) time-averaged drag coefficient, (b) drag coefficient amplitude, and (c) lift coefficient amplitude, versus the numerical time step, Δt. A grid consisting of 54,000 finite volumes is utilized. 23
16. Fig. 16. Variation of computed flow quantities with Reynolds number for uncontrolled flow past a circular cylinder, for the present study and literature studies: (a) Time-averaged drag coefficient, $\langle C_D \rangle$, (b) Strouhal number, St. 24
17. Fig. 17. Variation of computed flow quantities with Reynolds number for uncontrolled base flow past a circular cylinder, for the present study and literature studies: (a) Non-dimensional recirculation zone length, x_R/D, and (b) separation point angle, θ_s (the reference point is the front stagnation point). 25

18. Fig. 18. Computational results for *Re*=120, for uncontrolled flow and for two values of *b**. (a) Base flow slip velocity distributions and instantaneous streamline patterns of asymptotic flow states. (b) Drag and lift coefficient signals. Slip is applied at a no non-dimensional time of 300 units. 29
19. Fig. 19. Flow quantities versus *Re*, for different values of *b**: (a) non-dimensional recirculation length of base flow, (b) base flow separation angle, (c) time-averaged drag coefficient, (d) RMS fluctuation intensity of drag coefficient, and (e) RMS fluctuation intensity of lift coefficient.. 30
20. Fig. 20. *Re*=90, *b**=0.17: distribution of slip velocity, u_θ, on the cylinder surface for base flow, and lift coefficient signal, for the cases where slip condition is applied: (a) on a region extending ±37.5° from the front stagnation point, and (b) on a region extending ±37.5° from the rear stagnation point. Slip is applied at *t*=300. 31
21. Fig. 21. Sketch of slip condition application on the cylinder surface, for a flow from left to right: slip is applied in the arc ranging from θ_{min} to θ_{max}............................... 32
22. Fig. 22. *Re*=90, *b**=0.17: distribution of slip velocity, u_θ, on the cylinder surface for base flow, and lift coefficient signal, for the case where slip condition is applied on the entire cylinder surface and for three cases with partial slip. Slip is applied at *t*=300. The corresponding values of base flow separation point angle, θ_s, are also reported. 33
23. Fig. 23. Optimization flow chart. 36
24. Fig. 24. *Re*=90: objective function J_1 vs. objective function J_2, and sketch of the corresponding Pareto front. Three cases of full slip are also included and are compared to the corresponding optimal cases of partial slip, with the decrease in control effort highlighted.. 37
25. Fig. 25. *Re*=90: computed slip velocity profiles of base flow corresponding to solutions 1 to 4, the uncontrolled case and the case of stabilized flow with full slip, depicted in Fig. 24 (left column), and color-coded contours of instantaneous vorticity in the non-linear flow state (right column). 39
26. Fig. 26. *Re*=90: Drag and lift coefficient signals for solutions 1 to 4, the uncontrolled case and the case of stabilized flow with full slip, depicted in Fig. 24. Passive control is implemented at *t*=300. 40
27. Fig. 27. *Re*=90: design variables and separation point angle of base flow versus objective function J_2, for solutions along the Pareto front. The case of stabilized flow with full slip is also included. 41
28. Fig. 28. *Re*=180: objective function J_1 vs. objective function J_2, and sketch of the corresponding Pareto front. Four cases of full slip are also included and are compared to the corresponding optimal cases of partial slip, with the decrease in control effort highlighted. 42
29. Fig. 29. *Re*=180: computed slip velocity profiles of base flow corresponding to solutions 1 to 4, the uncontrolled case and the full slip case, depicted in Fig. 28 (left column), and color-coded contours of instantaneous vorticity in the non-linear flow state (right column).. 43
30. Fig. 30. *Re*=90: characterization of streamwise velocity profiles, for solutions 1 to 4, the uncontrolled case and the case of stabilized flow with full slip, depicted in Fig. 24. These solutions correspond to different levels of control effort, expressed in terms of the objective function J_2. (a) Velocity ratio vs. streamwise coordinate, (b) vorticity thickness vs. streamwise coordinate, and (c) velocity ratio vs. profile parameter 1/*N*. 45

31. Fig. 31. *Re*=90: values of local stability properties vs. streamwise coordinate, for solutions 1 to 4, the uncontrolled case and the case of stabilized flow with full slip, depicted in Fig. 24. These solutions correspond to different levels of control effort, expressed in terms of the objective function J_2. (a) Absolute frequency, and (b) absolute growth rate. 46
32. Fig. 32. Sketch of uniform suction and blowing profiles applied on different regions of the cylinder surface: (a) front stagnation point region, $\theta_1=0^o<\theta<\theta_2=40^o$, (b) sideway region, $\theta_1=40^o<\theta<\theta_2=150^o$, and (c) rear stagnation point region, $\theta_1=150^o<\theta<\theta_2=180^o$. 50
33. Fig. 33. *Re*=90: flow statistics versus suction coefficient, for suction/blowing applied on the front stagnation point region: (a) Strouhal number, *St*, (b) time-averaged drag coefficient, $<C_D>$, (c) amplitude of lift coefficient, $C_{L,ampl}$, and (d) amplitude of drag coefficient, $C_{D,ampl}$. 51
34. Fig. 34. *Re*=90: colour-coded contours of instantaneous vorticity, for different values of suction coefficient, C_{suc}, for suction/blowing applied on the front stagnation point region. (Negative values of C_{suc} correspond to blowing, and positive values to suction.) 52
35. Fig. 35. *Re*=90, suction/blowing applied from $\theta_1=0^o$ to $\theta_2=40^o$: base flow separation point angle, θ_s, vs. suction coefficient, C_{suc}. 53
36. Fig. 36. *Re*=90, suction/blowing applied from $\theta_1=0^o$ to $\theta_2=40^o$: base flow velocity ratio, *R*, vs. streamwise coordinate, for different values of suction coefficient, C_{suc}, for (a) suction, and (b) blowing. 54
37. Fig. 37. *Re*=90, suction/blowing applied from $\theta_1=0^o$ to $\theta_2=40^o$: base flow vorticity thickness, δ_w/D, vs. streamwise coordinate, for different values of suction coefficient, C_{suc}, for (a) suction, and (b) blowing. 54
38. Fig. 38. *Re*=90, suction/blowing applied from $\theta_1=0^o$ to $\theta_2=40^o$: base flow velocity ratio, *R*, vs. profile parameter 1/*N*, for different values of suction coefficient, C_{suc}, for (a) suction, and (b) blowing. Absolute instability boundary is illustrated by the red line (Monkewitz and Nguyen, 1987). 54
39. Fig. 39. *Re*=90: flow statistics versus suction coefficient, for suction/blowing applied on the cylinder sideway region: (a) Strouhal number, *St*, (b) time-averaged drag coefficient, $<C_D>$, (c) amplitude of lift coefficient, $C_{L,ampl}$, and (d) amplitude of drag coefficient, $C_{D,ampl}$. 55
40. Fig. 40. *Re*=90: colour-coded contours of instantaneous vorticity, for different values of suction coefficient, C_{suc}, for suction/blowing applied on the cylinder sideway region. (Negative values of C_{suc} correspond to blowing, and positive values to suction.) 56
41. Fig. 41. *Re*=90, with suction/blowing applied from $\theta_1=40^o$ to $\theta_2=150^o$: base flow separation point angle, θ_s, vs. suction coefficient, C_{suc}. 57
42. Fig. 42. *Re*=90, suction/blowing is applied from $\theta_1=40^o$ to $\theta_2=150^o$: base flow velocity ratio, *R*, vs. streamwise coordinate, for different values of suction coefficient, C_{suc}, for (a) suction, and (b) blowing. 57
43. Fig. 43. *Re*=90: suction/blowing applied from $\theta_1=40^o$ to $\theta_2=150^o$: base flow vorticity thickness, δ_w/D, vs. streamwise coordinate, for different values of suction coefficient, C_{suc}, for (a) suction, and (b) blowing. 58
44. Fig. 44. *Re*=90: suction/blowing is applied from $\theta_1=40^o$ to $\theta_2=150^o$: base flow velocity ratio, *R*, vs. profile parameter 1/*N*, for different values of suction coefficient,

C_{suc}, for (a) suction, and (b) blowing. Absolute instability boundary is illustrated by the red line (Monkewitz and Nguyen, 1987). 58
45. Fig. 45. Re=90: flow statistics versus suction coefficient, for suction/blowing applied on the rear stagnation point region: (a) Strouhal number, St, (b) time-averaged drag coefficient, $<C_D>$, (c) amplitude of lift coefficient, $C_{L,ampl}$, and (d) amplitude of drag coefficient, $C_{D,ampl}$........ 59
46. Fig. 46. Re=90: colour-coded contours of instantaneous vorticity, for different values of suction coefficient, C_{suc}, for suction/blowing applied on the rear stagnation point region. (Negative values of C_{suc} correspond to blowing, and positive values to suction.)........ 60
47. Fig. 47. Re=90, suction/blowing applied from θ_1=150° to θ_2=180°: base flow separation point angle, θ_s, vs. suction coefficient, C_{suc}. 61
48. Fig. 48. Re=90: suction/blowing applied from θ_1=150° to θ_2=180°: base flow velocity ratio, R, vs. streamwise coordinate, for different values of suction coefficient, C_{suc}, for (a) suction, and (b) blowing. 61
49. Fig. 49. Re=90, suction/blowing applied from θ_1=150° to θ_2=180°: base flow vorticity thickness, δ_w/D, vs. streamwise coordinate, for several values of suction coefficient, C_{suc}, for (a) suction, and (b) blowing. 62
50. Fig. 50. Re=90, suction/blowing applied from θ_1=150° to θ_2=180°: base flow velocity ratio R, vs. profile parameter $1/N$, for different values of suction coefficient, C_{suc}, for (a) suction, and (b) blowing. Absolute instability boundary is illustrated by the red line (Monkewitz and Nguyen, 1987). 62
51. Fig. 51. Sketch of transpiration velocity profile. 64
52. Fig. 52. Optimization flow chart. 66
53. Fig. 53. Re=90: objective function J_1 vs. objective function C_{suc} (suction coefficient). 67
54. Fig. 54. Re=90: computed transpiration velocity profiles corresponding to solutions 1-4, depicted in Fig. 53 (left column), and corresponding color-coded contours of instantaneous vorticity (right column). The case of uncontrolled flow is also included. 68
55. Fig. 55. Re=90: drag and lift coefficient signals for solutions 1-4, depicted in Fig. 53, and for the case of uncontrolled flow. Active open-loop control in terms of suction/blowing is implemented at t=300. 69
56. Fig. 56. Re=90: design variables versus objective function C_{suc}, for solutions along the Pareto front. The red square corresponds to stabilized flow at the minimal control effort, depicted by Point 4 in Fig. 53. 70
57. Fig. 57. Re=90: transpiration velocities versus objective function C_{suc}, for solutions along the Pareto front. The red square corresponds to stabilized flow at the minimal control effort, depicted by Point 4 in Fig. 53. 71
58. Fig. 58. Re=180: objective function J_1 vs. objective function C_{suc} (suction coefficient). 72
59. Fig. 59. Re=180: computed transpiration velocity profiles corresponding to solutions 1-4, depicted in Fig. 58 (left column), and corresponding color-coded contours of instantaneous vorticity (right column). The case of uncontrolled flow is also included. 73
60. Fig. 60. Re=180: drag and lift coefficient signals for solutions 1-4, depicted in Fig. 58, and for the case of uncontrolled flow. Active open-loop control in terms of suction/blowing is implemented at t=300. 74

61. Fig. 61. *Re*=90: characterization of streamwise velocity profiles, for solutions 1 to 4, depicted in Fig. 53, and for the case of uncontrolled flow. (a) Velocity ratio vs. streamwise coordinate, (b) vorticity thickness vs. streamwise coordinate, and (c) velocity ratio vs. profile parameter 1/*N*. 76
62. Fig. 62. *Re*=90: values of local stability properties vs. streamwise coordinate, for solutions 1 to 4, depicted in Fig. 53, and for the case of uncontrolled flow. (a) Absolute frequency, and (b) absolute growth rate. 77
63. Fig. 63. Proportional feedback loop control scheme (Park et al., 1994): the location of the feedback sensor, x_s, the extent of a transpiration slot, delimited by angles θ_{min} and θ_{max}, the proportional gain, k_p, as well as the control input signal, *u*(*t*), are depicted. 80
64. Fig. 64. Computational results of the present study and of Park et al. (1994) for *Re*=60, k_p=0.35, x_s=2.75: (a) instantaneous streamline pattern at a large time, and (b) signal of stream-wise velocity, *u*, at *x*=2.5, *y*=0.5. In the present simulation active feedback control in terms of time-dependent suction/blowing is implemented at *t*=300, and in the one of Park et al. (1994) at *t*=1200. 81
65. Fig. 65. *Re*=60, k_p=0.35, x_s=2.75: drag and lift coefficient signals. Active feedback control in terms of time-dependent suction/blowing is implemented at *t*=300.......... 81
66. Fig. 66. *Re*=60: objective function J_1 vs. objective function J_2. 84
67. Fig. 67. *Re*=60: drag and lift coefficient signals for solutions 1-4, depicted in Fig. 66. Active feedback control in terms of time-dependent suction/blowing is implemented at *t*=300.. 85
68. Fig. 68 *Re*=60: global frequencies for the uncontrolled case (open loop pole), as well as for solutions 1-4 (closed loop poles), depicted in Fig. 66. 85
69. Fig. 69. Sketch of the present proportional feedback loop control scheme. The non-dimensional location of the sensor, x_s/D, the actuation regime (hydrophobic area extends between θ_{min} and θ_{max}), the proportional gain, k_p, as well as the control input signal, *u*(*t*), are depicted. 87
70. Fig. 70. *Re*=60: flow quantities versus streamwise sensor location, x_s, at a proportional gain value of k_p=0.5: (a) Lift coefficient amplitude, $C_{L,ampl}$, (b) time-averaged drag coefficient, $<C_D>$, and (c) maximum value of non-dimensional slip length, b^*_{max}... 89
71. Fig. 71. *Re*=60, k_p=0.5: lift coefficient and slip length signals, for different streamwise locations of the sensor in the near wake. Active feedback control in terms of time-dependent slip conditions is implemented at *t*=300. 90
72. Fig. 72. *Re*=60, k_p=0.5: lift coefficient and slip length signals, for different streamwise locations of the sensor in the far wake. Active feedback control in terms of time-dependent slip conditions is implemented at *t*=300. 91
73. Fig. 73. *Re*=60: flow quantities versus proportional gain value, k_p, when the sensor is located at x_s=7: (a) Lift coefficient amplitude, $C_{L,ampl}$, (b) time-averaged drag coefficient, $<C_D>$, and (c) maximum value of non-dimensional slip length, b^*_{max}..... 92
74. Fig. 74. *Re*=60: objective function J_1 vs. objective function J_2, and sketch of the corresponding Pareto front. 94
75. Fig. 75. *Re*=60: lift coefficient and slip length signals for optimal solutions 1-4, depicted in Fig. 74. Active feedback control in terms of time-dependent slip is implemented at *t*=300. 95
76. Fig. 76. *Re*=90: objective function J_1 vs. objective function J_2, and sketch of the corresponding Pareto front. 96

77. Fig. 77. *Re*=90: lift coefficient and slip length signals for solutions depicted in Fig. 78 by Point a and Point b. Active feedback control in terms of time-dependent slip is implemented at *t*=300. 97
78. Fig. 78. *Re*=90: flow quantities vs. streamwise coordinate, for the base flow field of uncontrolled flow: (a) local linear absolute frequency, St_0, and (b) local linear absolute growth rate, $\omega_{0,i}$. The present results are compared against those of Pier (2002).. 105

List of Tables

1. Table 1 Computed values of statistical flow quantities, at different values of Reynolds number, for: (i) uncontrolled flow, (ii) stabilized flow at a critical value of non-dimensional slip length, also including a previous study (Legendre et al., 2009)...... 28
2. Table 2. *Re*=90: design variable values and corresponding objective function values, for the uncontrolled case, as well as for solutions 1 to 4 and the case of stabilized flow with full slip, depicted in Fig. 24. 38
3. Table 3 *Re*=90: time-averaged values of drag coefficient, $<C_D>$, and amplitude of lift coefficient, $C_{L,ampl}$, for the uncontrolled case, as well as for solutions 1 to 4 and the case of stabilized flow with full slip, depicted in Fig. 24. 38
4. Table 4. *Re*=180: design variable values and corresponding objective function values, for the uncontrolled case, as well as for solutions 1 to 4 and the full slip case, depicted in Fig. 28 44
5. Table 5. Quantities characterizing the flow local and global stability, for representative solutions of the optimization problem at *Re*=90. 46
6. Table 6. *Re*=90: Computed values of statistical flow quantities, at different values of the suction coefficient, C_{suc}, for the present and a previous study (Delaunay and Kaiktsis, 2001); computed values: time-averaged drag coefficient and Strouhal number. 49
7. Table 7. *Re* = 90: design variable values and corresponding objective function values, for the uncontrolled case, as well as for solutions 1-4, depicted in Fig. 53. 68
8. Table 8. *Re*=180: design variable values and corresponding objective function values, for the uncontrolled case, as well as for solutions 1-4, depicted in Fig. 58. 72
9. Table 9. Quantities characterizing the flow local and global stability, for representative solutions of the optimization problem at *Re*=90. 77
10. Table 10. *Re*=60: design variable values and corresponding objective function values, for the uncontrolled case, as well as for solutions 1-4, depicted in Fig. 66; the values of the components of the global frequency, *s*, i.e. the global linear growth rate, σ_r, and the linear frequency, σ_i, are also reported. 84
11. Table 11. *Re*=60: design variable values and corresponding objective function values, for the uncontrolled case, as well as for optimal solutions 1-4, depicted in Fig. 74... 95
12. Table 12. *Re*=90: values of design variables and objective functions, for the uncontrolled case, for solutions depicted by Points a and b in Fig. 76, as well as for solutions corresponding to the passive control scheme, utilizing steady slip conditions on a part (Points 1 and 2 of Fig. 24) and on the entire cylinder surface (Legendre et al. 2009); the values of ½$b^*\varphi$ magnitude, quantifying the control effort, are also reported. 97
13. Table 13. Coefficients of the Stuart-Landau equation at *Re*=50 and *Re*=60, corresponding to the present (computational) and previous, experimental (Schumm at al., 1994) and computational (Delaunay and Kaiktsis, 2001) studies. 106

Chapter 1: Cylinder wake control problem

1.1 Bluff body flows and applications

The practical importance of bluff body flows is remarkable due to their several applications in onshore, as well as in offshore applications. Typical examples of onshore applications include skyscrapers, high bridges, chimneys, TV antennas and light poles. On the other hand, offshore pipelines and oil risers are structures of great importance, exhibiting a bluff body behavior in terms of Vortex Induced Vibration (VIV). Further, several classical engineering applications exhibit a bluff body behavior, as for example the heat exchanger tubes.

In bluff body flows, the von Kármán vortex street is formed. Due to the resulting large fluctuating pressure forces, high amplitude time-dependent loads are exerted on the body. This dynamic loading can cause structural fatigue, ultimately leading to structural failure. Legendary failures of bluff body structures are the collapse of the Tacoma Narrows Bridge (1940) and the collapse of the cooling towers of the Ferrybridge power plant (1965). Thus, understanding and controlling the physics of bluff body flows is of high interest for a wide series of engineering applications.

1.2 Flow past a circular cylinder

Flow past a circular cylinder is a representative bluff body flow. As highlighted in Fornberg (1993), the cylinder wake belongs to those systems that are easy to define, but is difficult to solve and understand their behavior, making them only more attractive. During the last decades experimental and numerical studies were performed in order to identify the dynamics and physical properties of the uncontrolled flow in the steady as well as in the vortex shedding regime. Early experimental works were performed by Strouhal (1878) and von Kármán (1911). Later, Roshko (1954), Tritton (1959), Acrivos et al. (1968) and more recently Hammache and Gharib (1991), Green and Gerrard (1993) performed experimental studies in order to evaluate representative quantities characterizing the cylinder wake physics; these include the non-dimensional shedding frequency (Strouhal number), drag and lift coefficients, separation point angle, as well as length and width of the recirculation zone. Early computational studies of flow past a cylinder include the ones of Dennis and Chang (1970), Fornberg (1985), and Braza et al. (1986). More recently, the increase in computational power enabled three-dimensional Direct Numerical Simulation (DNS) studies. An extensive review of the problem, including both computational and experimental studies, was performed by Williamson (1996), who has significantly contributed to this field. Flow, flow past a circular cylinder has been studied extensively in the framework of local and global flow instability theory, as in the works of Jackson (1987), Zebib (1987), Barkley and Henderson (1996), and Mittal (2008). Along these lines, Monkewitz and Nguyen (1987), and Monkewitz (1988) performed a detailed instability analysis of properly defined families of wake profiles. More recently, the dynamics of spatially developing wakes has been interpreted by Pier and Huerre (2001), Pier (2002), and Gianneti and Luchini (2007), under the light of the latest findings in instability theory.

The dynamics of incompressible uncontrolled flow past a circular cylinder depends only on the Reynolds number, *Re* (commonly defined in terms of free stream velocity, the cylinder diameter and the kinematic viscocity of the fluid). Properties of this flow are well known for a wide range of Reynolds number, from creeping flows $(Re \to 0)$ to fully turbulent flows ($Re \approx 10^7$). At low Reynolds numbers, $Re<190$, the flow remains two-dimensional. In more detail, for $Re<6$, the flow is steady, with only one separation point, coinciding with the rear stagnation point (creeping flow). In the range $6<Re<47$, the flow is still steady, with a vortex pair forming immediately after the cylinder; its recirculation length increases linearly with Re, as reported in Takami and Keller (1969), Fornberg (1985) and in the more recent work of Gianneti and Luchini (2007). A periodic vortex shedding pattern is excited in the near wake as Re increases above a first critical value $Re_{2D,cr}=47$ (Jackson 1987). This transition corresponds to a Hopf bifurcation of the dynamical system (Jackson 1987). For $Re>Re_{2D,cr}$, the flow past a circular cylinder is characterized by global instability, whose non-linear state is the Kármán vortex street; the latter consists of a sequence of vortices, which are shed, two per shedding cycle. The onset of self-sustained flow oscillations has been commonly attributed to the presence of a sufficient intensity of local absolute instability in the near wake regime. The latter is expressed in terms of the magnitude of local positive absolute growth rates and the extent of the absolutely unstable regime (Chomaz et al. 1990). At $Re_{3D,cr}=188.5$, the cylinder wake undergoes a second bifurcation, and becomes three-dimensional (Barkley and Henderson 1996), due to a secondary instability in the spanwise direction. As the Reynolds number is further increased above $Re_{3D,cr}$, a number of other transitions occur. For $Re>1000$, the shear layers emanating from the cylinder become turbulent, resulting in the formation of a turbulent wake. Finally, for $Re > 5\times10^5$, the boundary layer becomes turbulent. Thus, the separation point is shifted downstream, resulting in the significant reduction of drag coefficient (drag crisis).

The present study is performed for the range $Re_{2D,cr}<Re<Re_{3D,cr}$, where the wake of uncontrolled flow exhibits an oscillatory behavior, but remains two-dimensional.

1.3 Optimization concepts

Optimization studies have been broadly employed in the last decades in several fields of engineering, including fluid mechanics applications. The goal of each optimization is to identify the values of proper variables (design variables) which maximize or minimize proper functions (objective functions). The latter can be associated with forces, performance, pollutant emissions, cost, etc. The domain of definition of the design variables forms the problem’s search space.

Optimization algorithms can be categorized into gradient based algorithms, algorithms based on evolutionary algorithms (EAs) and hybrid algorithms. Gradient based algorithms can be characterized by a high convergence speed; however, due to the poor exploration of the search space, the solution can converge to a local instead of the global optimum (maximum or minimum). EAs are semi-stochastic methods, based on an analogy with Darwin’s laws of natural selection. Since EAs belong to the multi-point search methods, a solution close to the global optimum can be determined even when the landscape of the objective function is multi-modal (characterized by several local minima). Moreover, EAs do not require the calculation of the gradient of the objective function; as a result, they can be applied to problems whose search space is discrete (in contrast to gradient-based search methods). Overall, evolutionary algorithms are very powerful and effective optimization tools, especially for multi-objective optimization problems. Finally, hybrid methods combine the advantages of both families of algorithms, by utilizing an EA at first in order to identify the region of the optimum, and subsequently a gradient based algorithm, to converge fast to the optimal solution(s).

Optimization problems can be categorized into Single Objective Optimization (SOO) ones, in the case of one objective function, and Multi Objective Optimization (MOO) ones, in the case of two or more objective functions.

In multi-objective optimization problems, a vector of n design variables, $\vec{x}$, is sought, which minimizes a vector $\vec{f}$ of k objective functions. The choice of design variables may be subject to constraints. Overall, a multi-objective optimization problem can be formulated as follows:

$$\left\{\begin{array}{l} min\ \vec{f}(\vec{x}) = \left(f_1(\vec{x}),\, f_1(\vec{x}), \ldots, f_k(\vec{x}) \right)^T \\ \vec{x} \in X = \left\{ \vec{x} \in \Re^n \right\} \\ f_i(\vec{x}) = f_i(x_1, x_2, \ldots, x_n), i = 1, \ldots, k \end{array}\right\} \tag{1}$$

In multi-objective minimization methodologies, we commonly seek Pareto optimal (or dominant) solutions, see Fig. 1. In the case of a minimization problem, a solution $\vec{x}_1$ is defined as dominant over $\vec{x}_2$ when:

$$\begin{array}{l} f_i(\vec{x}_1) \le f_i(\vec{x}_2), \forall i = 1, \ldots, k \\ f_i(\vec{x}_1) < f_i(\vec{x}_2), \exists i = 1, \ldots, k \end{array} \tag{2}$$

The collection of all non-dominated solutions is the *Pareto front*, sketched in Fig. 1 for the case of a minimization problem with two objective functions (k = 2).

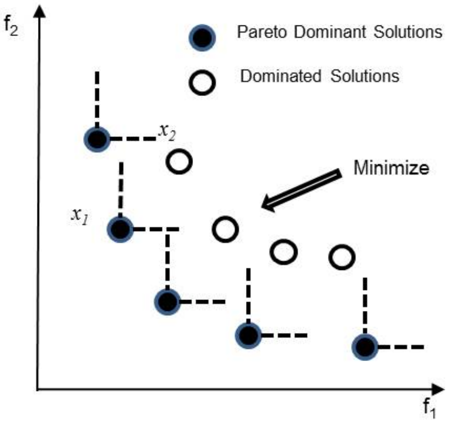

Fig. 1. Sketch of Pareto front for a minimization problem with two objective functions.

Alternatively, multi-objective optimization problems can be solved using a penalty based (weighted-sum) single objective optimization approach. Here, the solution corresponds to a single point on the Pareto front of the multi-objective strategy. Thus, in order to attain the final Pareto front, the single objective optimization problem should be solved for a large number of weight values, potentially requiring a substantially larger computational time in comparison to the Pareto-ranking multi-objective optimization approach. Another disadvantage of weigthed-sum methods is that, in the case of a non-convex Pareto front, a large set of optimal solutions cannot be attained (Deb, 2001). Thus, in the present study a Pareto-ranking multi-objective optimization strategy utilizing genetic algorithms is adopted.

Genetic algorithms (GAs) belong to the family of evolutionary algorithms. In the genetic algorithms terminology, a search point is called an individual (or chromosome). Individuals are composed by genes, which are the problem design variables, encoded using a floating point representation in the form of bit strings. Commonly, multi-objective optimization with genetic algorithms utilizes the following steps (see Andreadis et al. (2011) and references therein).

Step 1: The number of individuals of each generation, n, is chosen. These individuals are quasi-randomly initialized within the space of the design variables. As each individual is represented by a bit string, each bit can be determined by a random number generator. Throughout the present study each generation consists of 20 individuals.
Step 2: The evaluation code (also called evaluator or analyzer) is used to determine the objective functions, f_i, for each individual.
Step 3: The 'Pareto ranking' index is determined for each candidate solution by counting the number of individuals that dominate the examined candidate solution. The Pareto ranking, R, is equal to the above number increased by 1. Thus, for a non-dominated solution, the Pareto Ranking is equal to 1. Subsequently, a proper index, the 'fitness value', is assigned to each individual, based on its Pareto ranking and, depending on the algorithm used, on previously selected elite solutions. The optimization tool developed in the present work adopts the Non–dominated Sorting Genetic Algorithm NSGA-II for ranking solutions within a generation (Deb et al. 2002). The particular optimization tool utilizes the ParadisEO genetic algorithms library (Cahon et al. 2004), enabling, for the purposes of the present study, an effective coupling with the evaluator (here, the ANSYS CFX CFD code).
Step 4: If the terminal condition of the problem is not satisfied, the routine selects the parents (Step 5), and uses them to create offspring (Step 6). The optimization procedure stops when a prescribed criterion is fulfilled; in the present work, termination is imposed after 50 generations.
Step 5: Parent selection takes place using a roulette wheel method. Each roulette wheel slot receives an individual from the current population; individuals with better fitness values are assigned with a larger wheel slot size. The procedure thus penalizes less fit individuals, still giving them the chance to participate in the reproduction process, hence maintaining diversity through the generations.
Step 6: A new individual is created using the operations of crossover and mutation (Fig. 2). In the crossover operation, some individuals are randomly selected among the parents determined in Step 5. If the operation of mutation is utilized, certain bits of an individual are randomly selected, and a new individual is created by reversing the selected bits, resulting in a new search point. In the present work the probability of crossover has a value 80%, whereas the probability of mutation has a value of 15%. Finally, a percentage of the new generation (5% in the present study) can be created by the process of elitism, i.e. by repeating a number of highly ranked (low fitness value) individuals.

The entire procedure is presented schematically in Fig. 3.

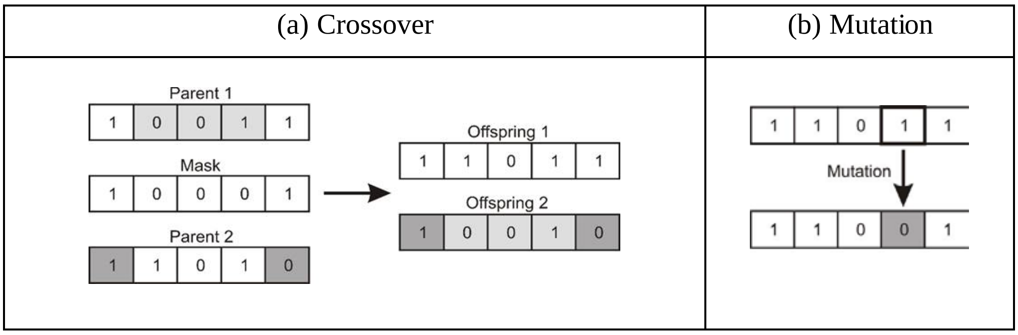

Fig. 2. Operations of: (a) crossover and (b) mutation.

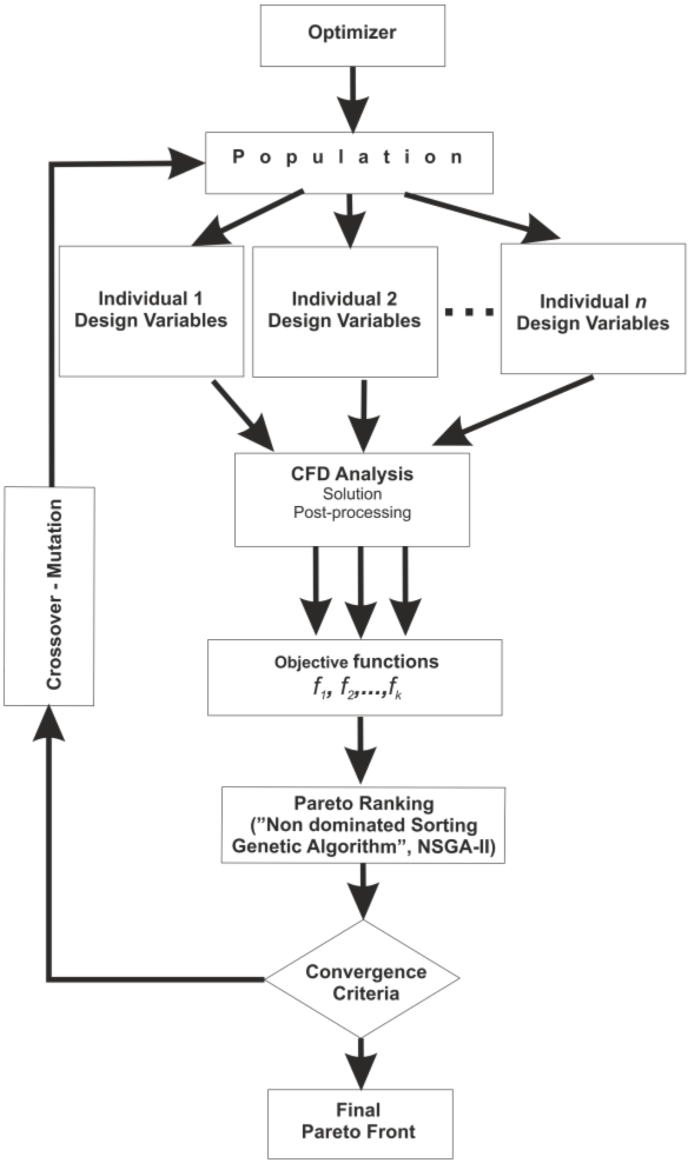
Optimizer
Population
Individual 1 Design Variables
Individual 2 Design Variables
Individual n Design Variables
CFD Analysis
Solution
Post-processing
Crossover - Mutation
Objective functions
$f_1, f_2, \ldots, f_k$
Pareto Ranking
("Non dominated Sorting Genetic Algorithm", NSGA-II)
Convergence Criteria
Final Pareto Front

Fig. 3. Evolutionary algorithm outline.

1.4 Hydrodynamic instability concepts

An extensive presentation of the subject of hydrodynamic instability is given in the book of Drazin and Reid (1981), while more recent theoretical advances can be found in the review papers of Huerre and Monkewitz (1990) and Chomaz (2005), as well as in the book of Schmid and Hennigson (2001). Open shear flows, as wake flows, are spatially developing, i.e. the mean velocity profile is not uniform in the streamwise direction. Thus, it is important to distinguish between the local and global instability properties, referring to the properties of a local velocity profile and the properties of the entire flow, respectively. Linear instability theory studies the evolution of small perturbations superimposed on a reference flow. A brief outline of concepts of linear local and global instability, used throughout the present study, is reported in the following two subsections.

1.4.1 Local instability

Local instability analysis can only be considered under the assumption of a parallel or locally parallel flow. In a parallel flow, the velocity field is unidirectional, and thus does not depend on the streamwise coordinate, as is for example in the case of the flow inside a long pipe. The cylinder wake flow, being of main interest in the present study, is a spatially developing flow, which is by definition non-parallel. In this case, the assumption of a locally parallel flow is valid if the wave-length, λ, of a typical instability is much shorter than the characteristic length scale, L, of the spatial evolution of the flow, i.e. $\lambda \ll L$. Here, L can be defined as

$$\frac{1}{L} \approx \frac{1}{\theta(x)} \cdot \frac{d\theta(x)}{dx} \tag{3}$$

where $\theta(x)$ represents a characteristic width. In flow past a cylinder, the vorticity thickness can be considered as a proper characteristic width.

Local instability analysis aims at studying the evolution of small amplitude perturbations, superimposed on the steady flow solution of a parallel flow, referred to as 'base flow'. A base flow can be characterized using the concepts of local absolute and local convective instability, introduced by Twiss (1952). The distinction between absolute and convective instability is based on the asymptotic impulse response of an infinitely extended parallel flow. If a linear impulse response grows exponentially in the location of its generation, the flow is characterized as absolutely unstable (Fig. 4a). If, on the other hand, a linear impulse response is convected away from the location of its generation, amplifying as it convects downstream (thus leaving the flow undisturbed at large times), the flow is characterized as convectively unstable (Fig. 4b). Equivalently, the two flows can be distinguished by the sign of temporal growth rate of the mode dominating the response at large times. Positive temporal growth rate corresponds to an absolutely unstable flow, whereas negative temporal growth rate corresponds to a convectively unstable flow.

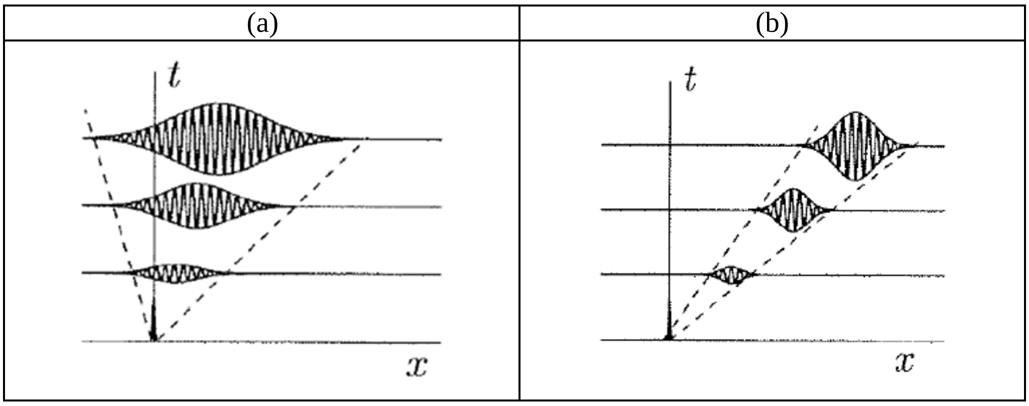

Fig. 4. Sketch of spatio-temporal evolution of a perturbation in a parallel flow: (a) absolutely unstable flow and (b) convectively unstable flow. Flow direction: left to right.

In open shear flows, important parameters of a velocity profile determining the convectively or absolutely unstable character of the flow are the velocity ratio, R, and and the vorticity thickness, δ_w, defined as follows:

$$R(x) = \left(U_{\max}(x) - U_{\min}(x)\right) / \left(U_{\max}(x) + U_{\min}(x)\right) \tag{4}$$

$$\delta_w(x) = \left(U_{\max}(x) - U_{\min}(x)\right) / \left(\left| \frac{dU(x)}{dY} \right|_{\max} \right) \tag{5}$$

where U_{max} and U_{min} are the maximum and minimum velocity values, respectively, at a streamwise location x. The velocity ratio, R, highlights the existence, as well as the intensity of back-flow. According to the above definition, for R>1, a velocity profiles includes a region of negative velocity, corresponding to back-flow. In particular, in flow past a circular cylinder, streamwise velocity profiles extracted from the region of the recirculation zone (see Fig. 6) are characterized by backflow; this results in R>1. On the other hand, the vorticity thickness characterizes the steepness of the velocity profiles under consideration. An increase in vorticity thickness corresponds to smoother velocity profiles, whereas a decrease corresponds to steeper profiles. Concerning the flow past a cylinder, in the near wake region the profiles are steeper (of the 'top hat' type), whereas in the far wake region the profiles exhibit are smoother (Fig. 5a).

As indicated in Monkewitz (1988), local linear instability is associated with the wake profile parameters, R, δ_w. In particular, absolute instability increases with velocity ratio (increasing back flow), while it also depends on vorticity thickness. In particular, in Monkewitz and Nguyen (1987), a family of velocity profiles was defined parametrically in terms of the velocity ratio, R and a parameter N; the latter is associated with the vorticity thickness, with steep profiles characterized by high values of N. The wake profile can thus be defined as a function of the the transverse coordinate, y, as follows:

$$U(y) = 1 - R + 2RF(y) \tag{6}$$

where

$$F(y) = \left[1 + \sinh^{2N}(y \sinh^{-1}(1))\right]^{-1} \tag{7}$$

For the above wake profiles, Monkewitz and Ngouyen (1987) performed a normal mode analysis, in order to identify the region characterized by absolute instability as a function of (R, N); the region corresponding to absolute instability is illustrated in Fig. 5b. In the present study, the velocity profiles under consideration are extracted from the base flow field, and are curve-fitted with the equation (6) calculating the corresponding values of R, $1/N$. Further, the R, $1/N$ pairs can be placed on the R-$1/N$ plot (Fig. 5b), thus immediately characterizing the nature of local instability (absolute or convective).

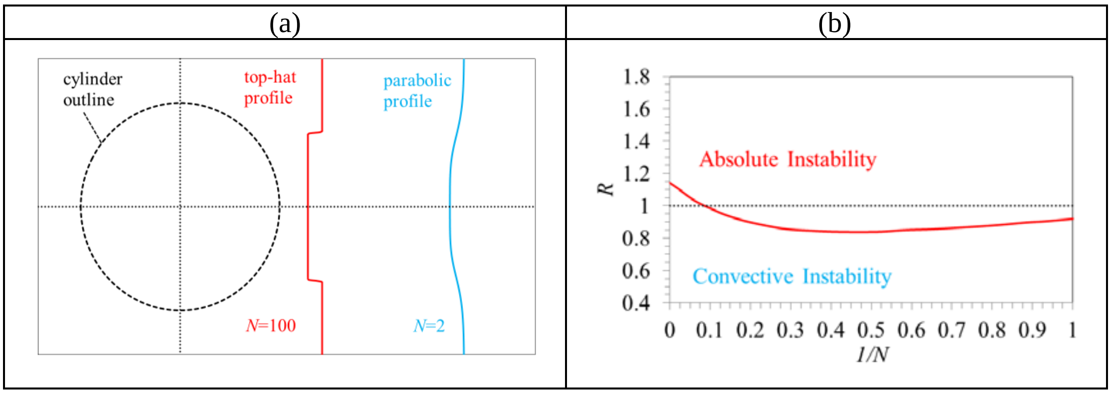

Fig. 5. (a) Cylinder wake profiles of the family described by eq. (6) for N=100 (top-hat profile) and N=2 (parabolic profile), and (b) absolute and convective instability regions as a function of the wake velocity profile parameters, R, $1/N$ (Monkewitz, 1988).

Local instability properties can be calculated from the solution of the Orr-Sommerfeld stability equation. The latter is derived from the Navier-Stokes equations, as outlined subsequently.

Linear hydrodynamic stability analysis of a shear flow, as the flow past a cylinder, considers a base flow, which is mathematically the solution of the steady flow equations. If the base flow is perturbed, the resulting instantaneous fields are characterized in two dimensions by the velocity field (u,υ) and the static pressure, p, expressed in terms of the coordinates of a cartesian system (x,y) and time, t. The partial differential equations governing the evolution of the base flow are the 2D Navier-Stokes equations:

$$\begin{aligned}
&\frac{\partial u}{\partial x}+\frac{\partial \upsilon}{\partial y}=0\\
&\frac{\partial u}{\partial t}+u\frac{\partial u}{\partial x}+\upsilon\frac{\partial u}{\partial y}+\frac{1}{\rho}\frac{\partial p}{\partial x}=\nu\left[\frac{\partial^2 u}{\partial x^2}+\frac{\partial^2 u}{\partial y^2}\right]\\
&\frac{\partial \upsilon}{\partial t}+u\frac{\partial \upsilon}{\partial x}+\upsilon\frac{\partial \upsilon}{\partial y}+\frac{1}{\rho}\frac{\partial p}{\partial y}=\nu\left[\frac{\partial^2 \upsilon}{\partial x^2}+\frac{\partial^2 \upsilon}{\partial y^2}\right]
\end{aligned} \tag{8}$$

The solution of the Navier-Stokes equations can be considered as a superposition of the base flow field (U,V,P) and a perturbation flow field (u',υ',p') as follows (Drazin and Reid, 1981):

$$\begin{aligned}
&u(x,y,t)=U(x,y)+u'(x,y,t)\\
&\upsilon(x,y,t)=V(x,y)+\upsilon'(x,y,t)\\
&p(x,y,t)=P(x,y)+p'(x,y,t)
\end{aligned} \tag{9}$$

Under the parallel flow assumption, discussed above, the velocity vector of a two-dimensional base flow reduces to ($U(y),0$), resulting in a superposition of the following form:

$$\begin{aligned}
&u(x,y,t)=U(y)+u'(x,y,t)\\
&\upsilon(x,y,t)=\upsilon'(x,y,t)\\
&p(x,y,t)=P(x,y)+p'(x,y,t)
\end{aligned} \tag{10}$$

After substituting the above expressions in equations (8), and neglecting the quadratic terms of velocity disturbances, the partial differential equations governing the perturbation dynamics are derived:

$$\begin{aligned}
&\frac{\partial u'}{\partial x}+\frac{\partial \upsilon'}{\partial y}=0\\
&\frac{\partial u'}{\partial t}+U\frac{\partial u'}{\partial x}+\upsilon'\frac{dU}{dy}+\frac{1}{\rho}\frac{\partial p'}{\partial x}=\nu\left[\frac{\partial^2 u'}{\partial x^2}+\frac{\partial^2 u'}{\partial y^2}\right]\\
&\frac{\partial \upsilon'}{\partial t}+U\frac{\partial \upsilon'}{\partial x}+\frac{1}{\rho}\frac{\partial p'}{\partial y}=\nu\left[\frac{\partial^2 \upsilon'}{\partial x^2}+\frac{\partial^2 \upsilon'}{\partial y^2}\right]
\end{aligned} \tag{11}$$

A combination of the previous equations eliminates the pressure contributions and can yield a system of two partial differential equations with unknowns the perturbations $u'(x,y,t)$ and $\upsilon'(x,y,t)$, with coefficients that are functions of only the transverse direction, y. The particular solutions for u' and υ' have the form $F(y)e^{i(kx-\omega t)}$, where $k=k_r+ik_i$ and $\omega=\omega_r+i\omega_i$ represent the complex wavenumber and frequency, respectively. The real part of the local linear complex frequency is the local linear frequency, ω_r, whereas its imaginary counterpart is the local linear temporal growth rate, ω_i. These particular solutions are called 'normal modes'. By considering that u' and υ' can be derived from the differentiation of a proper streamfunction, of the same functional form, the Orr-Sommerfeld stability equation can be derived:

$$(k\cdot U-\omega)\cdot(f''-k^2\cdot f)-k\cdot U''\cdot f+i\cdot v\cdot(f''''-2\cdot k^2\cdot f''+k^4\cdot f)=0 \qquad (12)$$

where differentitation of the amplitude function, *f*, is with respect to the coordinate *y*.

The Orr-Sommerfeld equation is a fourth order partial differential equation in *f*, which can be solved by imposing appropriate boundary conditions. In the case of wake flows, vanishing velocity perturbations can be used as boundary conditions at the profile boundaries, as long as the boundaries lie far enough, in a region where the effect of the bluff-body on the surrounding flow vanishes. Non-trivial solutions of the equation exist only for particular combinations of the parameters k, ω, v. These combinations are expressed by the dispersion relation, defined as follows:

$$F(v,k,\omega)=0 \qquad (13)$$

Typically, the viscosity, v, is known; therefore the above equation involves two complex unknown eigenvalues. Thus, in local stability calculations, one needs to assign the viscosity (equivalently the Reynolds number) and either k or ω, and solve for the eigenvalues of the other complex unknown. In the present study, the Orr-Sommerfeld equation is computationally solved, by utilizing a numerical solver based on high-order finite differences, developed by G.S. Triantafyllou (see Triantafyllou et al., 1986); the dispersion relation, $\omega=\omega(k)$, is thus attained. Further, the local linear absolute complex frequency, ω_0, is identified as a branch point singularity of the dispersion relation:

$$\left.\frac{d\omega(k)}{dk}\right|_{k=k_0}=0 \qquad (14)$$

The process of identifying the absolute frequency for a representative wake profile (Fig. 6b), extracted from the cylinder wake base flow (Fig. 6a), is illustrated in terms of the isocontours of ω_r and ω_i of Fig. 6c,d. As illustrated in Fig. 5d, this profile is characterized by a positive absolute growth rate, i.e. it is absolutely unstable.

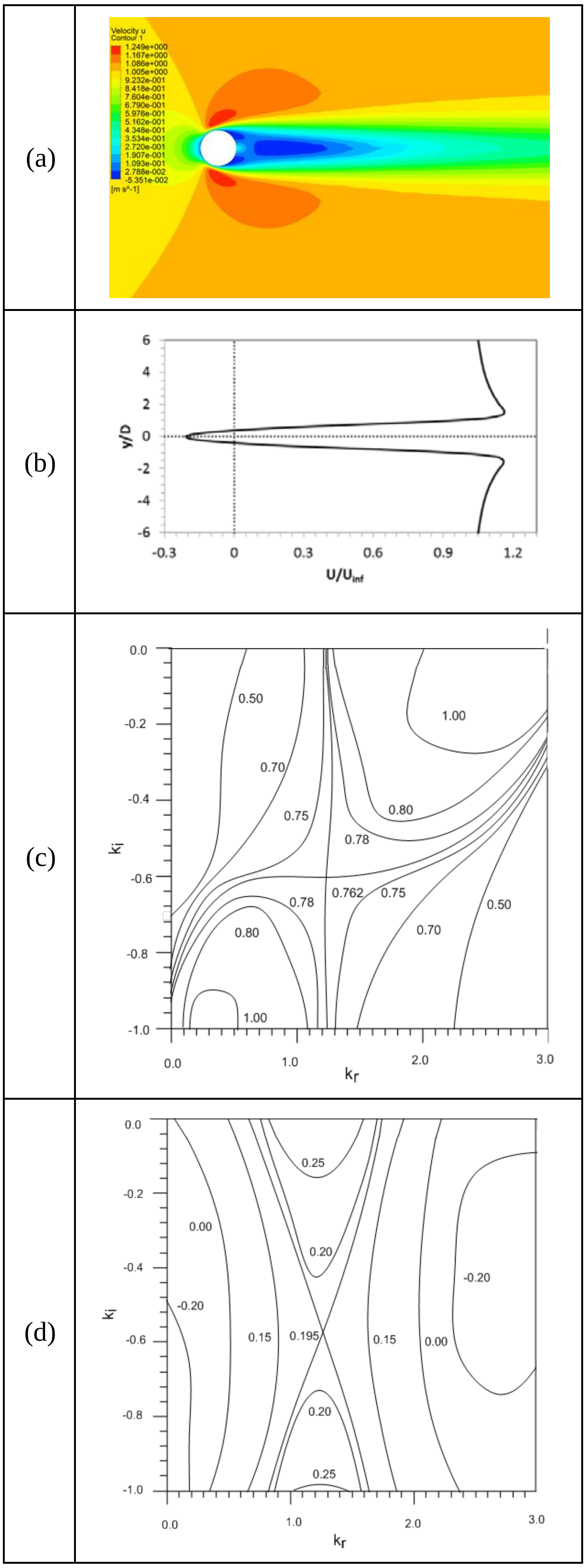

Fig. 6. Base flow past a circular cylinder, at *Re*=90: (a) iso-contours of streamwise velocity, *U*, (b) streamwise velocity profile at *x/D*=2, and corresponding Orr–Sommerfeld eigenvalues in terms of isocontours of (c) ω_r and (d) ω_i, in the complex wavenumber plane. Here, $\omega_0 = 0.762 + 0.195 \cdot i$, corresponding to absolute instability.

Finally, local instability properties can be correlated with the global flow instability, as demonstrated by the work of Chomaz et al. (1990). In spatially developing flows, a sufficient intensity of local absolute instability, depending on both the streamwise extent of absolute instability and the magnitudes of absolute growth rates, is necessary to trigger global instability. This concept is expressed by the criterion of Chomaz et al. (1990) for the onset of global instability:

$$I_g = \int_{x_a}^{x_b} \sqrt{\omega_{0,i}(x)}\,dx \geq \mathrm{O}(1) \tag{15}$$

where the absolutely unstable region is considered to extend from $x=x_a$ to $x=x_b$. The quantity, I_g, expresses the global intensity of absolute instability; this quantity must exceed a certain threshold to excite unstable global modes. In the present work, the stability of cylinder wakes is characterized by stability calculations, validated against literature data; corresponding validation studies are presented in Appendix A.1.

1.4.2 Global instability

As has been demonstrated in previous studies (Mathis et al. 1984, Provansal et al. 1987, Jackson 1987), the von Kármán vortex street is a direct consequence of a Hopf bifurcation. This type of bifurcation is characterized by the continuous growth of an unstable global mode towards a limit cycle, at supercritical values of the system parameter (here the Reynolds number). At slightly supercritical Reynolds number, the time variation of small disturbances superimposed on the steady solution can be divided into three stages. First, disturbances organize themselves into the most unstable mode, whereby all but one discrete frequencies are being damped. In general, this initial step lasts for a short time, in comparison to the second part, where the dominant eigenmode, or unstable global mode, grows exponentially, at a rate referred to as the "global" growth rate. The exponential growth of disturbances can be observed, as long as these remain small (i.e. if the square of disturbance terms remains negligible with respect to the other terms in the governing equations), so that the system dynamics is in very good approximation linear around the steady solution. In the third and final part, taking place after sufficient time, disturbances reach a non-negligible level, and non-linear effects (due to the quadratic terms of fluctuations) tend to moderate their growth, until their saturation. As shown in the experimental studies on the circular cylinder wake (Mathis et al. 1984, Provansal et al. 1987), the corresponding system dynamics can be described in terms of an evolution equation of a characteristic (complex) amplitude, *A(t)*, as the Stuart-Landau equation:

$$\frac{dA}{dt} = sA - lA|A|^2 + O\left(|A|^5\right) \tag{16}$$

In the present study the amplitude, A, can represent any global quantity (e.g. the drag coefficient, C_D, or the lift coefficient, C_L), or a local quantity (e.g. the v-velocity at a given point). The parameters of the Stuart-Landau equation are the global frequency, $s = \sigma_r + i\sigma_i$, and the Landau constant, $l = l_r + il_i$. The real part of the global frequency, σ_r is referred to as the global growth rate, whereas the imaginary part, σ_i, expresses the linear frequency. The global frequency depends, on the value of the bifurcation parameter, in particular the Reynolds number for the problems of the present study. While the global frequency, s, is a global (i.e. spatially-independent) quantity, the complex Landau constant, l, depends on spatial location (i.e. the choice of A), with the ratio l_r/l_i being spatially independent.

The procedure for calculating these coefficients from a raw (computational or experimental) signal, corresponding to the growth of an unstable mode, is presented in Schumm et al. (1994), and can be summarized as follows. For an amplitude represented by a proper signal, as that of the lift coefficient, $C_L(t)$, the global linear growth rate, σ_r, and the global linear frequency, St_g, can be calculated based on the signal magnitude, $|A(t)|$, and the signal phase, $a(t)$, respectively:

$$\sigma_r = \frac{1}{|A|}\frac{d|A|}{dt} \tag{17}$$

$$St_g = \frac{\sigma_i}{2\pi} = \frac{1}{2\pi}\frac{da}{dt} \tag{18}$$

As outlined in Schumm et al. (1994), to determine the complex signal $A(t) = A_r(t) + iA_i(t) = |A(t)|e^{ia(t)}$ from the raw signal, $A_r(t)$, the imaginary part of the signal, $A_i(t)$, should be calculated; this can be attained using the Hilbert transform of $A_r(t)$:

$$A_i = Hilbert(A_r) \tag{19}$$

An ideal Hilbert transform is an all-pass filter imposing a constant phase shift of $\frac{\pi}{2}$; the corresponding transfer function in the frequency domain is:

$$H(f) = \begin{cases} -i, if & f > 0 \\ +i, if & f < 0 \end{cases} \tag{20}$$

Finally, the signal magnitude, $|A(t)|$, and the signal phase, $a(t)$, are calculated as follows:

$$|A|(t) = \sqrt{A_r^2 + A_i^2} \tag{21}$$

$$a(t) = \arctan\left(\frac{A_i}{A_r}\right) \tag{22}$$

The process of identifying the global linear growth rate, σ_r, and the global linear frequency, St_g, by analyzing the lift coefficient signal, $C_L(t)$, of uncontrolled flow past a circular cylinder at *Re*=60 is illustrated in Fig. 7. Based on the computed lift signal, $C_L(t)$ (Fig. 7a), the lift signal magnitude $|C_L(t)|$ is calculated (Fig. 7b), by using equations (19, 21). The linear region (of exponential growth) is identified by plotting the lift signal magnitude in a logarithmic scale (Fig. 7c). Finally, the global linear growth rate, σ_r, and the global linear frequency, St_g, are calculated by applying equations (17) and (18), respectively.

The present methodology and tools developed for calculating global linear growth rate and frequency have been validated by comparing results from analyzing computed lift signals with literature data; an excellent agreement has been demonstrated (see Appendix A.2).

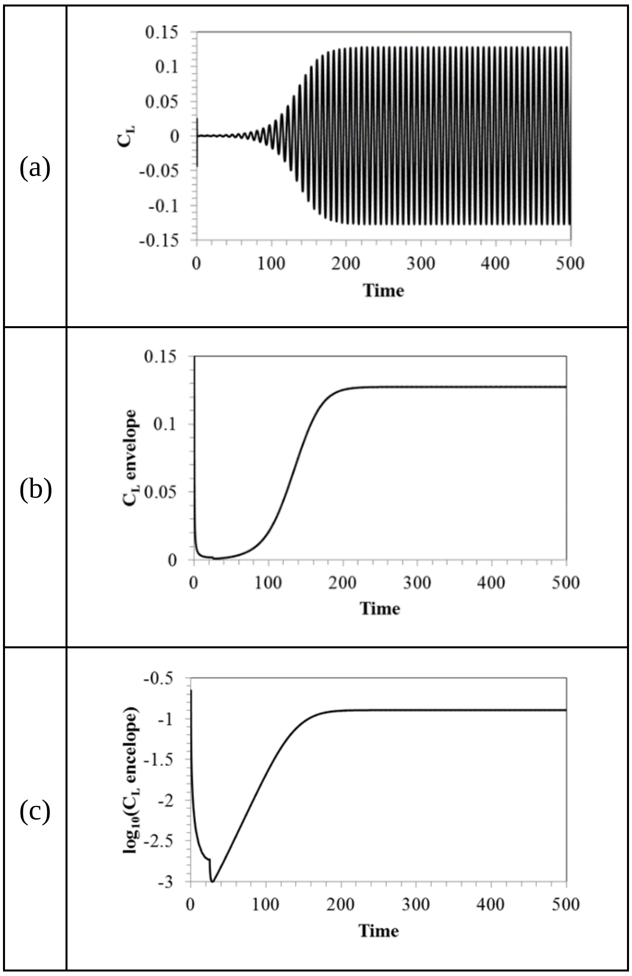

Fig. 7. *Re*=60, uncontrolled flow past a circular cylinder: (a) Computed lift coefficient signal, C_L(t), (b) Lift coefficient magnitude versus time, |C_L(t)|, and (c) semi-log plot of lift coefficient versus time, $\log_{10}|C_L(t)|$. Here, σ_r=0.04137, St_g=0.121.

1.5 Flow control: application to flow past a cylinder

Flow control can be defined as the action of manipulating a flow in order to obtain a beneficial change. When a control scheme is applied to a dynamical system, an actuator performs a control action, which is defined by a controller, in order to achieve a desired control goal. As analyzed in Gad-el-Hak (2007), control schemes can be classified in three categories: (a) passive control, (b) active open-loop control, and (c) active feedback control. In passive control, no energy input is introduced. The flow system is thereby properly transformed (e.g. in terms of a geometry modification), in order to achieve a prescribed goal. In active open-loop control, a steady energy input is required, in order to implement a predefined control action; the latter is independent of the system state. Finally, in active feedback control, the state of the system, as represented by one or more signals measured via sensors, is fed back to a controller, which determines the control action of an actuator, to approach a given control goal; the system state thus guides the control implemented. Feedback flow control concepts are analyzed in Aamo and Krstic (2003) and Bewley (2001), among others. Modern flow control studies trarget a wide range of applications: drag reduction in aircrafts, process control in chemical industries, route control in aircrafts, ships and vehicles, etc. Commonly, a control strategy is associated with undesired secondary effects (as drag increase with turbulence enhancement). Thus, flow control can be considered from an optimization point of view, i.e. achieving the control objective while also minimizing negative effects.

Regarding flow past a cylinder, several control strategies have been reported in literature studies, of all three types outlined above; an extensive review is presented in Choi et al. (2008). In particular, passive control studies include the one by Roshko (1955), who placed a splitter plate in the cylinder wake, to suppress the vortex street. Strykowski and Sreenivasan (1990), Mittal and Raghuvanshi (2001), and Yildirim et al. (2010) investigated the stabilizing effects induced by the placement of a smaller cylinder (control wire) in a cylinder wake. More recently, the effect of slip conditions on the cylinder surface, enabled by hydrophobic and superhydrophobic materials, has been investigated. It was demonstrated that a significant reduction in the intensity of lift and drag force oscillations can be attained (You and Moin, 2007), and even a full suppression of the vortex street (Legendre et al., 2009). Open-loop control studies have utilized cylinder rotation, steady or oscillatory, to affect the flow stability and dynamics, e.g. Tokumaru and Dimotakis (1991), Tokumaru and Dimotakis (1993), and Mittal and Kumar (2003). Wood (1964), Delaunay and Kaiktsis (2002), and Dong et al. (2008) have shown that the dynamics of cylinder wake can be substantially affected by means of mass transpiration from the cylinder surface. Of particular interest is the work of Milano and Koumoutsakos (2001). They have used two types of actuation in order to control flow past a cylinder: (a) steadily and tangentially to the cylinder surface moving belts, and (b) steady blowing/suction from the cylinder surface with a zero net mass constraint. Both control schemes have been optimized by means of a clustering genetic algorithm, aiming at the minimization of drag force. Other open-loop control schemes include cylinder heating (Lecordier et al. 1991), as well as the application of a Lorentz force (Chen and Aubry 2003). Finally, active feedback control strategies have included acoustic excitation of the wake (Roussopoulos 1993), time-dependent mass transpiration (Park et al., 1994, Min and Choi, 1999) and time-dependent cylinder rotary oscillations (Lee et al., 2009).

1.6 Flow control methods implemented in the present study

The goal of the present study is to achieve partial or full vortex street cancelation, by means of a minimal control effort. Since global stability is strongly affected by the local stability properties in the near wake region, one may device a control strategy consisting in the proper modification of the near wake velocity profiles. For this purpose, two appropriate control measures are applied on the cylinder surface, namely: (a) implementation of slip conditions, and (b) application of mass transpiration.

Firstly, slip conditions are applied on the surface of the cylinder, in the frame of a passive control scheme. The latter can be implemented in practice by hydrophobic and superhydrophobic materials. These materials enable fluid slip with respect to the solid surface. As indicated in Rothstein (2010), hydrophobic and superhydrophobic surfaces are promising candidates for drag reduction and possibly heat transfer enhancement in engineering flow applications. You and Moin (2007), Legendre et al. (2009), Muralidhar et al. (2011), and Seo and Song (2012) investigated the flow past a hydrophobic cylinder, aiming at identifying the effects of the resulting surface hydrophobicity on flow stability and dynamics. It was demonstrated that hydrophobicity reduces the intensity of lift and drag force oscillations (You and Moin, 2007), and may even lead to a complete suppression of the vortex street (Legendre et al., 2009). These effects of slip on flow dynamics can be correlated to the modification of the near wake structure of the base flow, and mainly to the decreased extent of the two recirculation zones, as highlighted in Muralidhar et al. (2011) and in Seo and Song (2012); this affects in turn the non-linear flow state. In flow past a cylinder, a major advantage in implementing surface hydrophobicity is the lack of any other intervention in terms of either energy input or geometry modification. As the manufacturing of hydrophobic and superhydrophobic surfaces is still quite expensive, minimizing the associated cost (e.g. by minimizing the hydrophobic/superhydrophobic area and the material cost per unit area) should be a main consideration of a corresponding design. The goal of the present study is thus to investigate whether a formal optimization procedure can lead to full or partial suppression of the Kármán vortex street by use of substantially lower control effort, in comparison to the previous studies. In the present study, this goal is achieved by implementing hydrophobicity on a part of the cylinder surface (partial slip), instead of the entire cylinder surface (full slip); the extent of this region is identified in the frame of an optimization study.

Secondly, steady mass transpiration is applied on the surface of the cylinder, utilizing an active open-loop control scheme. The stabilizing/destabilizing effects of steady mass transpiration were investigated in the representative previous literature studies of Wood (1964), Delaunay and Kaiktsis (2002), and Dong et al. (2008). In particular, the work of Delaunay and Kaiktsis (2002) was motivated by the fact that global instability is strongly affected by the local instability properties in the near wake region. Thus, suction or blowing was applied only in the rear stagnation point region. Delaunay and Kaiktsis (2002) demonstrated that vortex street can be completely suppressed, utilizing both suction and blowing. However, the suction control effort may be an order of magnitude greater than the corresponding blowing control effort, leading to the conclusion that the most effective method is blowing (Delaunay and Kaiktsis, 2002). Extending the approach of the above studies, with the aim of minimizing the total control effort, in the present work mass transpiration is not restricted in the rear stagnation point region, and includes the front stagnation point region, as well as in the sideway region. Further, in order to minimize the pumping requirements of mass transpiration and the corresponding power input, the minimization of the suction/blowing flow rate is of high interest; here, a practically relevant constraint of zero net flow rate is considered. To this end, an optimization problem is formulated, in order to arrive at optimal solutions corresponding to partial or full vortex street cancellation, at a minimal control effort.

The thesis is organized as follows. In chapter (2) we present the computational modeling of the problem and the numerical method used. In chapter (3) we present the passive control scheme which utilizes surface hydrophobicity, and the corresponding results of the optimization problem. In chapter (4) we present the active open-loop control scheme which utilizes mass transpiration, and the corresponding optimization results. In both chapters (3) and (4) the results are interpreted by stability analysis calculations. In chapter (5) two active feedback control schemes are applied, utilizing (a) active mass transpiration, and (b) active surface hydrophobicity; the parameters of both control schemes are optimized for minimum control effort. Finally, in chapter (6) the novelties of the present work and its contribution to scientific research are highlighted, and in chapter (7) the main conclusions are summarized, and suggestions are made for future work.

Chapter 2 : Computational approach

We consider an infinitely long circular cylinder of diameter D immersed in a uniform cross-flow of a Newtonian fluid, with free stream velocity U_{inf}. Two control setups are implemented. In the first setup, slip conditions are applied on the cylinder surface, whereas, in the second one, mass transpiration is implemented. Both control measures are perfectly symmetric with respect to the symmetry axis parallel to the free stream. These control measures are applied first on the entire cylinder surface and next on a part of it. In the present computational study, Direct Numerical Simulation (DNS) is utilized. The details of problem setup and numerical method, as well as results of resolution and validation tests perfomed, are given in the present chapter.

2.1 Problem formulation

We consider flow past a cylinder at low values of Reynolds number. The flow is governed by the two-dimensional incompressible Navier–Stokes equations, written here in non-dimensional form:

$$\nabla \cdot \vec{u} = 0 \tag{23}$$

$$\frac{\partial \vec{u}}{\partial t} + \vec{u} \cdot \nabla \vec{u} = -\nabla p + \frac{1}{Re} \Delta \vec{u} \tag{24}$$

where $\vec{u} = (u, \upsilon)$ is the velocity vector and p the static pressure. '∇' denotes $\left(\frac{\partial}{\partial x}, \frac{\partial}{\partial y} \right)$,

'Δ' is the Laplace operator, $\frac{\partial^2}{\partial x^2} + \frac{\partial^2}{\partial y^2}$, and '$\cdot$' denotes the scalar product. All variables are defined in a Cartesian coordinate system (x, y), whose origin is located at the cylinder center. Here, physical variables are non–dimensionalized with proper scales based on the cylinder diameter, D, the free stream velocity, U_{inf}, and the fluid density, ρ, whereas frequencies are non-dimensionalized as Strouhal numbers, $St = \frac{fD}{U_{inf}}$. The Reynolds number is defined as, $Re = \frac{U_{inf} D}{\nu}$, where ν is the kinematic viscosity of the fluid.

The numerical solution of the governing equations utilizes the ANSYS CFX CFD code. Here, a second-order finite volume approach, with quadrilateral finite volumes, is adopted.

The computational domain, illustrated in Fig. 8, extends 20D upstream from the cylinder center and 60D downstream, while the lateral boundaries lie 17D from y=0, the domain centerline (Fig. 8). The adequacy of this domain size has been demonstrated in relevant literature studies, as in Kaiktsis et al. (2007), Evangelinos and Karniadakis (1999), and Delaunay and Kaiktsis (2001), for uncontrolled flow. Furthermore, Delaunay and Kaiktsis (2001) demonstrated that, in the case of mass transpiration, the flow solution is not affected for a domain size of the order of the present one or bigger.

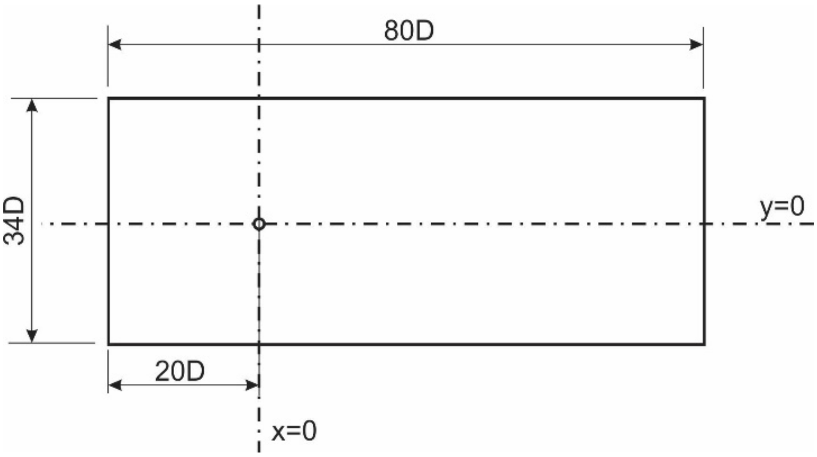

Fig. 8. Sketch of the flow domain.

The following conditions are prescribed at the domain boundaries.

Inflow and lateral boundaries: $u = U_{inf} = 1, \quad \upsilon = 0$

Outflow boundary: *p=0,* Neumann velocity boundary condition.

Depending on the control method, the following boundary conditions are applied on the cylinder surface:

(a) For uncontrolled flow, a no-slip condition is implemented on the cylinder surface: $u=\upsilon=0$.

(b) When slip conditions are applied on the entire cylinder surface or on a part of it (see chapter 3), the Navier model (Zhang et al. 2012) is adopted. The model assumes that the fluid flows against a fictitious (non-hydrophobic) surface, located at a distance *b* from the actual solid boundary; the distance *b* is called the slip length; a typical sketch demonstrating its physical importance is presented in Fig. 9. According to the Navier model, the slip velocity at the cylinder surface is proportional to the local values of shear stress and slip length. Thus, in the present problem, the boundary conditions on the cylinder surface can be defined in terms of the non-dimensional velocity components in the circumferential, u_θ, and radial direction, u_r, as follows:

$$u_\theta = \tau b^* Re = b^* \frac{\partial u_\theta}{\partial r}, \; u_r = 0 \tag{25}$$

where τ is the non-dimensional wall shear stress and $b^* = \dfrac{b}{D}$ is the non-dimensional slip length. In the present setup, slip conditions are applied first on the entire cylinder surface (Fig. 10a) and next on a part of it, i.e. on an arc lying between θ_{min} and θ_{max} (Fig. 10b); on the non-hydrophobic part of the surface, a no-slip condition (u=0, υ=0) is applied. It is noted that the value of slip length is assumed to be constant along the entire hydrophobic part of the cylinder surface.

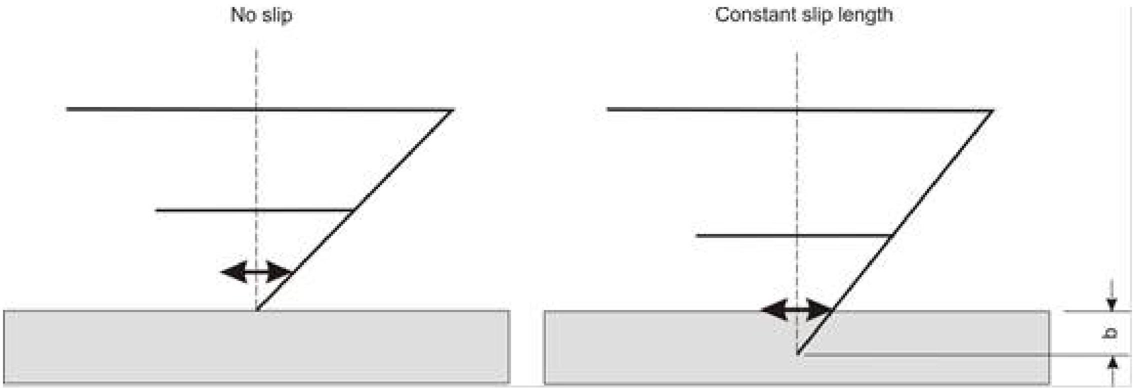
No slip
Constant slip length
b

Fig. 9. Definition of slip length, *b*, in flow past a hydrophobic surface.

(a)	(b)
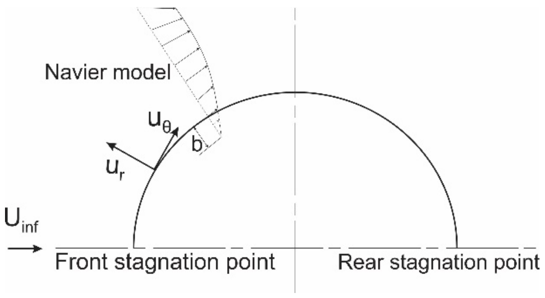	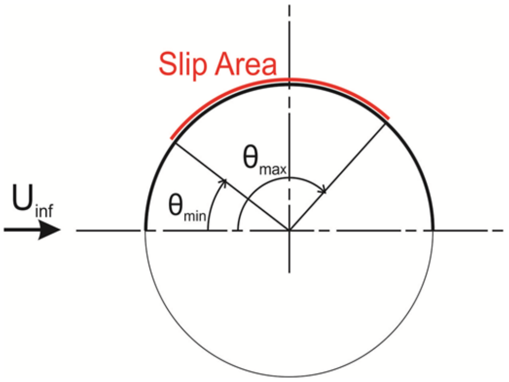

Navier model
u_θ
u_r
b
U_{inf}
Front stagnation point
Rear stagnation point
Slip Area
θ_{max}
U_{inf}
θ_{min}

Fig. 10. (a) Application of slip on the entire cylinder surface: sketch of velocity profile near the cylinder, for a slip length *b*. (b) Application of slip on an arc lying between θ_{min} and θ_{max}.

(c) When mass transpiration is applied on the cylinder surface, the corresponding suction or blowing velocity profile is specified on the cylinder boundary, and the direction of the velocity is radial. Here, two cases are considered: (a) suction or blowing is applied on a part of the cylinder surface (Fig. 11a), and (b) suction is applied on a part of the cylinder surface, whereas blowing is applied on the remaining part (Fig. 11b). In both cases, the control effort is quantified based on the suction flow rate, Q_{suc}, defined as follows:

$$Q_{suc} = -\int_{-\pi}^{\pi} u(\theta) R d\theta \tag{26}$$

where *R* is the cylinder radius. Taking into account the reference flow rate, $Q_{ref} = U_{inf} D$, the non-dimensional counterpart of Q_{suc}, the suction coefficient, C_{suc}, is defined:

$$C_{suc} = \frac{Q_{suc}}{Q_{ref}} \tag{27}$$

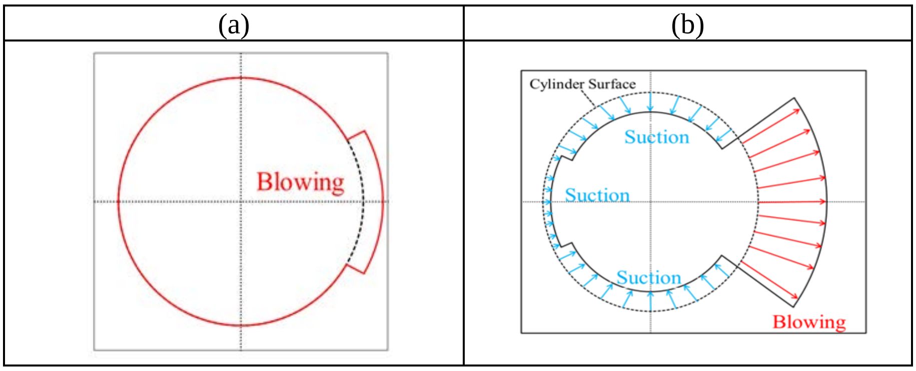

Fig. 11. (a) Application of blowing on a part of the cylinder surface, (b) application of suction on a part of the cylinder surface and blowing on the remaining part.

In flows past bluff bodies, the forces exerted on the body consist a main feature, which is of high importance for practical applications. The total force results from the summation of the pressure and the viscous force, $F_{Total} = F_{Pressure} + F_{Viscous}$. The pressure force, $F_{Pressure}$, and the viscous force, $F_{Viscous}$, on the cylinder surface are defined as follows:

$$F_{\text{Pressure}} = -\int_{Cylinder} p \cdot \vec{n} \cdot dA \tag{28}$$

$$F_{Viscous} = \int_{Cylinder} \mu \cdot \nabla \vec{u} \cdot \vec{n} \cdot dA \tag{29}$$

where $\nabla \vec{u}$: the velocity gradient on the cylinder surface, $\vec{n}$: the unitary normal vector to the surface, μ: the dynamic viscosity of the fluid. Forces are commonly expressed in non-dimensional form in terms of the drag and lift coefficients. For F_X and F_Y being, the x and y components of the total force per unit length, F_{total}, the drag coefficient, C_D, and the lift coefficient, C_L, are defined as follows:

$$C_D = \frac{2F_X}{\rho U_{\inf}^2 D}, \quad C_L = \frac{2F_Y}{\rho U_{\inf}^2 D} \tag{30}$$

Throughout the present study, the drag and lift forces are calculated by processing computed instantaneous flow fields.

2.2 Resolution tests

The numerical solution of the discretized Navier-Stokes equations utilizing the finite volume method, as presented in the previous section, is obtained by proper spatial discretization of the flow domain and temporal discretization of the time domain. In the following sub-sections a proper finite volume mesh, as well as a proper value of the numerical time step, are selected, by means of spatial and temporal resolution tests.

2.2.1 Mesh generation – spatial resolution tests

In the present study, due to the presence of the cylinder, the generation of a fine mesh can be based on the decomposition of the flow domain in sub-domains; here the flow domain is divided into three, five and eleven sub-domains (Fig. 12). The spatial resolution tests are performed for a numerical time step value Δt=0.01. For each of the grids considered, force coefficients are calculated for an uncontrolled flow at a Reynolds number value of 90, and are presented in Fig. 14. The time-averaged value of the drag coefficient, $<C_D>$ (Fig. 14a), the amplitude of the drag coefficient, $C_{D,ampl}$ (Fig. 14b), and the amplitude of the lift coefficient, $C_{L,ampl}$ (Fig. 14c), show practically negligible differences between the highest resolution (11 sub-domains – total of 113,000 finite volumes) and a medium resolution (5 sub-domains – total of 54,000 finite volumes). This demonstrates the adequacy of a spatial resolution consisting of 54,000 finite volumes in this range of Reynolds number, and is therefore used throughout the main body of the present thesis. It is also noted that, based on spatial resolutions tests, a number of about 100 finite volumes osculating to the cylinder surface is sufficient; a detail of such a mesh near the cylinder surface is presented in Fig. 13.

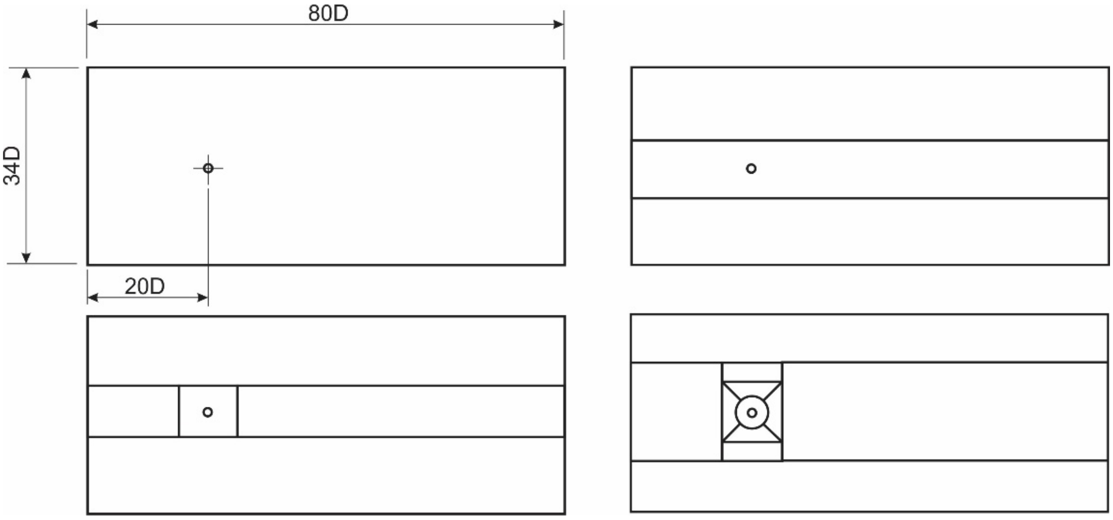

Fig. 12. Decomposition of the flow domain into three, five and eleven sub-domains.

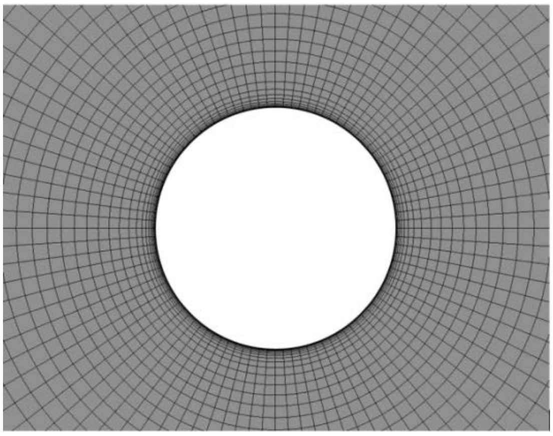

Fig. 13. Detail of a finite volume mesh close to the cylinder (the number of finite volumes osculating to cylinder surface is close to 100).

	Spatial discritization (Δt=0.01)
(a)	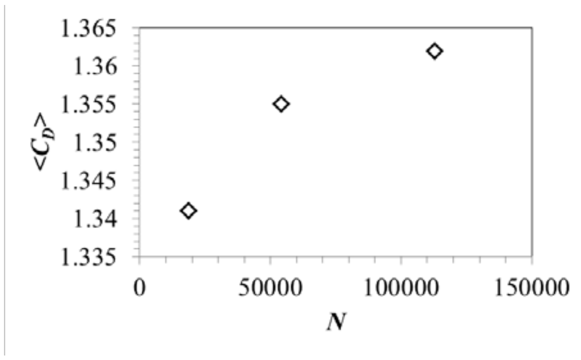
(b)	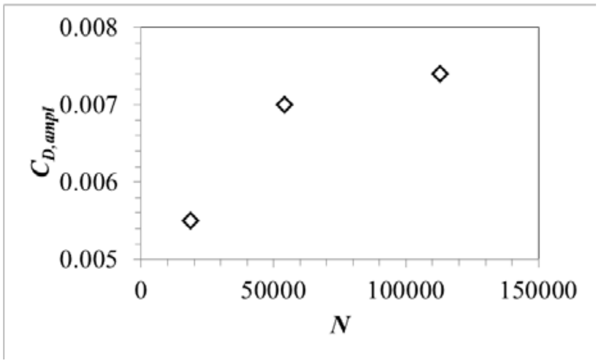
(c)	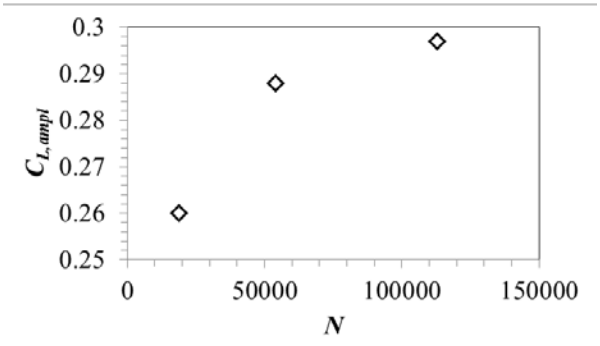

Fig. 14. Spatial resolution tests for uncontrolled flow at *Re*=90. Computed values of force coefficients: (a) time-averaged drag coefficient, (b) drag coefficient amplitude, and (c) lift coefficient amplitude, versus the number of finite volumes, *N*. A time step value of Δt=0.01 is utilized.

2.2.2 Temporal resolution tests

In the present sub-section, temporal resolution tests are reported for a grid consisting of 54,000 finite volumes. Four values of the numerical time step are tested, namely Δt = 0.005, 0.01, 0.02, and 0.05. The corresponding computed values of force coefficients are presented in Fig. 15. The results demonstrate that the deviation between the results of the highest resolution (Δt=0.005) and a lower one (Δt=0.01) is in the third decimal point, i.e. the flow fields computed for a time step of Δt=0.01 are acceptable; thus, this value of the time step is used in all simulations reported subsequently.

	Temporal discritization (N=54,000)
(a)	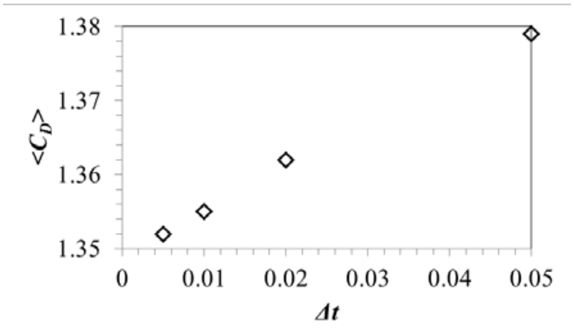
(b)	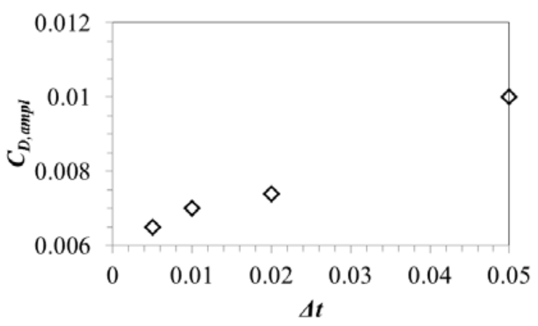
(c)	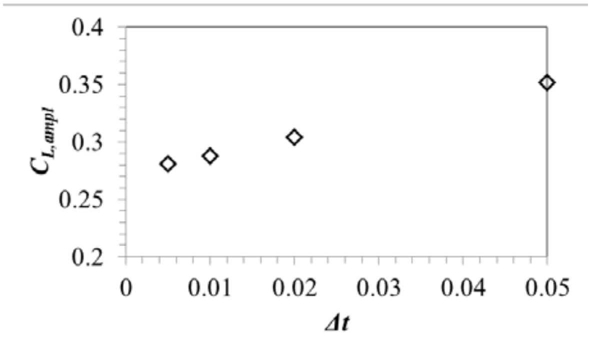

Fig. 15. Temporal resolution tests for uncontrolled flow at Re=90. Computed values of force coefficients: (a) time-averaged drag coefficient, (b) drag coefficient amplitude, and (c) lift coefficient amplitude, versus the numerical time step, Δt. A grid consisting of 54,000 finite volumes is utilized.

2.3 Validation tests

The present CFD results are validated by comparing high resolution simulations of the uncontrolled flow against published literature data; both the non-linear flow state and the base flow are considered. Here, the Reynolds number range Re=10 to 180 is simulated, for which the flow remains two-dimensional. First, results regarding the non-linear flow state are presented in Fig. 16. In particular, Fig. 16a presents the variation of time-averaged drag coefficient with Reynolds number, for the present study and that of Henderson (1995), and Fig. 16b the variation of non-dimensional shedding frequency (Strouhal number) for the present results and the ones of Barkley and Henderson (1996) and Fey et al. (1998); an excellent agreement between the present and the literature results is demonstrated. On the other hand, results concerning the base flow are presented in Fig. 17. In particular, Fig. 17a presents the variation of non-dimensional length of the recirculation zones with Reynolds number, for the present results and the ones of Delaunay and Kaiktsis (2001), and Gianneti and Luchini (2007); the well-known linear dependence is illustrated, with the present results being in excellent agreement with the previous studies. Finally, Fig. 17b presents the variation of separation point angle with Reynolds number, for the present results and the ones of Fornberg (1980), indicating an acceptable agreement. It is noted that, regarding the separation point of the base flow, several literature data are available, with deviations of up to 15^o degrees between them (Wu et al., 2004); the present results are characterized by values close to the middle of the range of reported values.

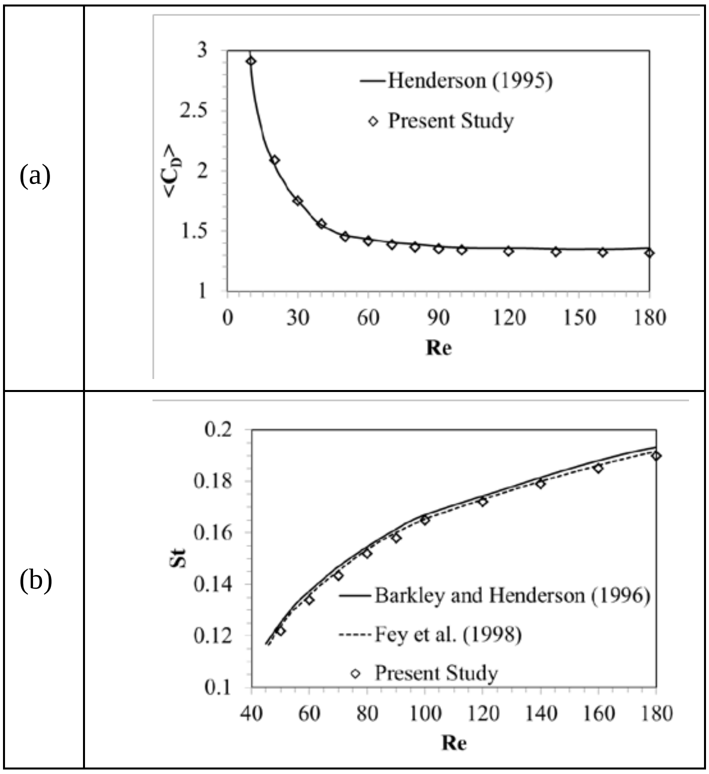

Fig. 16. Variation of computed flow quantities with Reynolds number for uncontrolled flow past a circular cylinder, for the present study and literature studies: (a) Time-averaged drag coefficient, $<C_D>$, (b) Strouhal number, *St*.

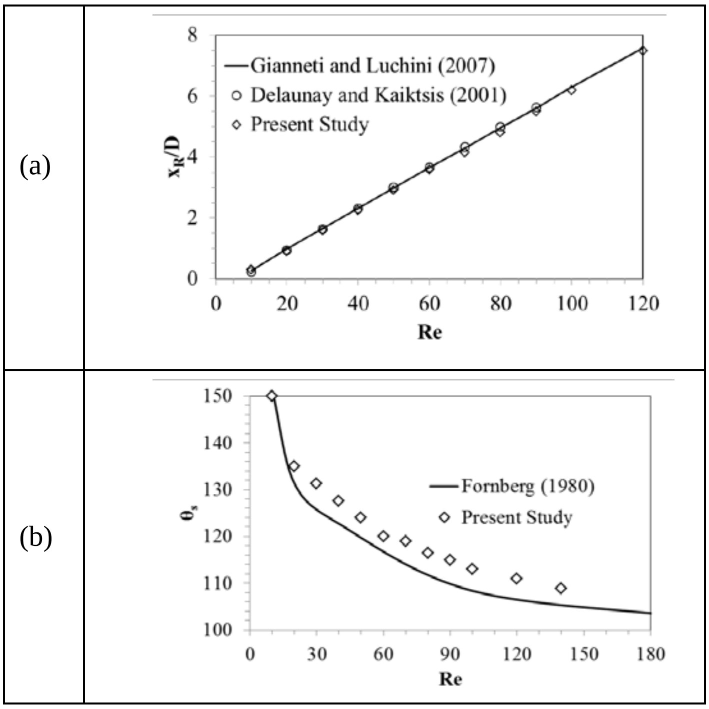

Fig. 17. Variation of computed flow quantities with Reynolds number for uncontrolled base flow past a circular cylinder, for the present study and literature studies: (a) Non-dimensional recirculation zone length, x_R/D, and (b) separation point angle, θ_s (the reference point is the front stagnation point).

2.4 Summary of Chapter 2

In this chapter, a computational model of the flow past a circular cylinder was developed. First, the geometry of the flow domain of a proper size was generated. Next, the governing equations and the boundary conditions of the problem were defined. In particular, regarding the cylinder surface, different boundary conditions, corresponding to different control approaches, were presented: (a) application of a slip condition, and (b) application of mass transpiration. Reference was made to the finite volume method of the ANSYS CFX used in the present work. Spatial and temporal resolutions tests were developed, and have demonstrated grid and time step independence. Finally, validation tests were performed, for both the non-linear and the base flow state, and demonstrated an excellent agreement between the present results and the ones of literature studies.

Chapter 3: Implementation of surface hydrophobicity

In the present chapter, a passive control scheme of a flow past a cylinder is implemented, aiming at a full or partial suppression of the Kármán vortex street. First, hydrophobicity is applied on the entire cylinder surface (full slip); the present results are in good agreement with those of previous literature studies. However, based on numerical experiments, it is found that implementing slip either in the front stagnation point region or in the rear stagnation point region has a destabilizing effect on the flow. Guided by this observation, slip is applied on a part of the cylinder surface (partial slip), and the stabilizing effects are compared to the corresponding case of full slip, illustrating the superiority of partial slip. Thus, a multi-objective optimization problem is formulated, aiming at arriving at desired levels of flow unsteadiness at a minimal control effort in terms of partial slip; this control effort is quantified by the product of slip length and hydrophobic area. Optimal solutions of the Pareto front correspond to a decrease in control effort of the order of 50%, in comparison to full slip. Finally, representative optimal solutions are characterized by means of local and global instability calculations.

3.1 Application of slip on the entire cylinder surface

In the present section, a slip condition is applied on the entire cylinder surface, and the corresponding computational results are presented; the concept of full slip has been defined in section 2.1. For given Reynolds number, the flow is computed for several values of b^*, as follows: Time dependent simulations are first performed for the uncontrolled case ($b^*=0$), until a limit cycle is reached. Subsequently, controlled cases ($b^*\neq 0$) are simulated, with a field on the limit cycle of uncontrolled flow as initial condition. This is equivalent to implementing a finite amplitude perturbation, for all controlled flow cases investigated. The corresponding base flows are also computed.

For all values of Re considered, it is found that the intensity of flow fluctuations decreases at increasing slip length, until stabilization of the global flow is attained at a critical value of b^*. The effects of full slip on the global flow are illustrated in Fig. 18, for a representative value of Reynolds number ($Re=120$). In particular, Fig. 18a shows the computed flow structure, for different values of b^*, in terms of instantaneous streamline patterns, illustrating the decrease of vortex intensity at a b^* value of 0.10, and the cancellation of the Kármán street at $b^*=0.20$. Slip velocity distributions for the base flow fields, also shown in Fig. 18a, demonstrate the increase in slip velocity magnitude at increasing b^*, with the maximum of distribution appearing at higher values of angle θ, in agreement with a corresponding dependence of base flow separation point angle (see below). Further, the drag and lift coefficient signals of Fig. 18b demonstrate a substantial decrease in average (drag) and fluctuating force components after the onset of slip control (at a non-dimensional time of

300 units). Force fluctuations become zero at large times in the case of global flow stabilization (b^*=0.20).

Table 1 summarizes important statistical quantities of the uncontrolled flow, as well as the critical b^* values for stabilization, and the corresponding drag coefficient values. It is verified that the control effort for stabilization, expressed by the critical value of b^*, is an increasing function of *Re*. The critical $b*$ values found in the present study are in good agreement with the ones of Legendre et al. (2009), also presented in Table 1. The computed values of drag coefficient, C_D, of stabilized flow are substantially lower than the reported time-averaged values, $<C_D>$, of uncontrolled flow.

Table 1 Computed values of statistical flow quantities, at different values of Reynolds number, for: (i) uncontrolled flow, (ii) stabilized flow at a critical value of non-dimensional slip length, also including a previous study (Legendre et al., 2009).

	Uncontrolled flow (present study)			Stabilized flow (present study)		Stabilized flow (Legendre et al., 2009)
Re	*St*	$<C_D>$	$C_{L,RMS}$	b^*	C_D	b^*
60	0.134	1.417	0.089	0.090	1.149	0.088
90	0.158	1.380	0.202	0.170	0.826	0.169
120	0.171	1.334	0.294	0.200	0.684	0.204
180	0.183	1.325	0.429	0.250	0.495	0.251

In more detail, Fig. 19 presents important global quantities of the base flow, as well as force RMS fluctuation intensities at the saturated non-linear state, for several combinations of the controlling parameters (*Re*, b^*). Fig. 19a demonstrates that the increase in slip length reduces the recirculation zone length, x_R/D, of the base flow, while maintaining the well-known linear dependence on Reynolds number of the uncontrolled flow, for low values of b^*. The observed decrease is, of course, a consequence of the delayed flow separation at increasing b^*, expressed in terms of the angle θ_s (Fig. 19b), which is enabled by the higher momentum in the boundary layer region. Finally, Fig. 19c, Fig. 19d and Fig. 19e illustrate the decrease in force coefficient levels at increasing b^*; for all values of b^*, fluctuation intensities remain increasing functions of *Re*. In summary, increasing the slip length for a given value of Reynolds number results in delayed separation in base flow, which in turn reduces the extent of recirculation zones (equivalently: modifies the near wake stability properties). As a result, the intensity of flow fluctuations in the saturated non-linear state decreases, and the flow is stabilized at a critical value of slip length.

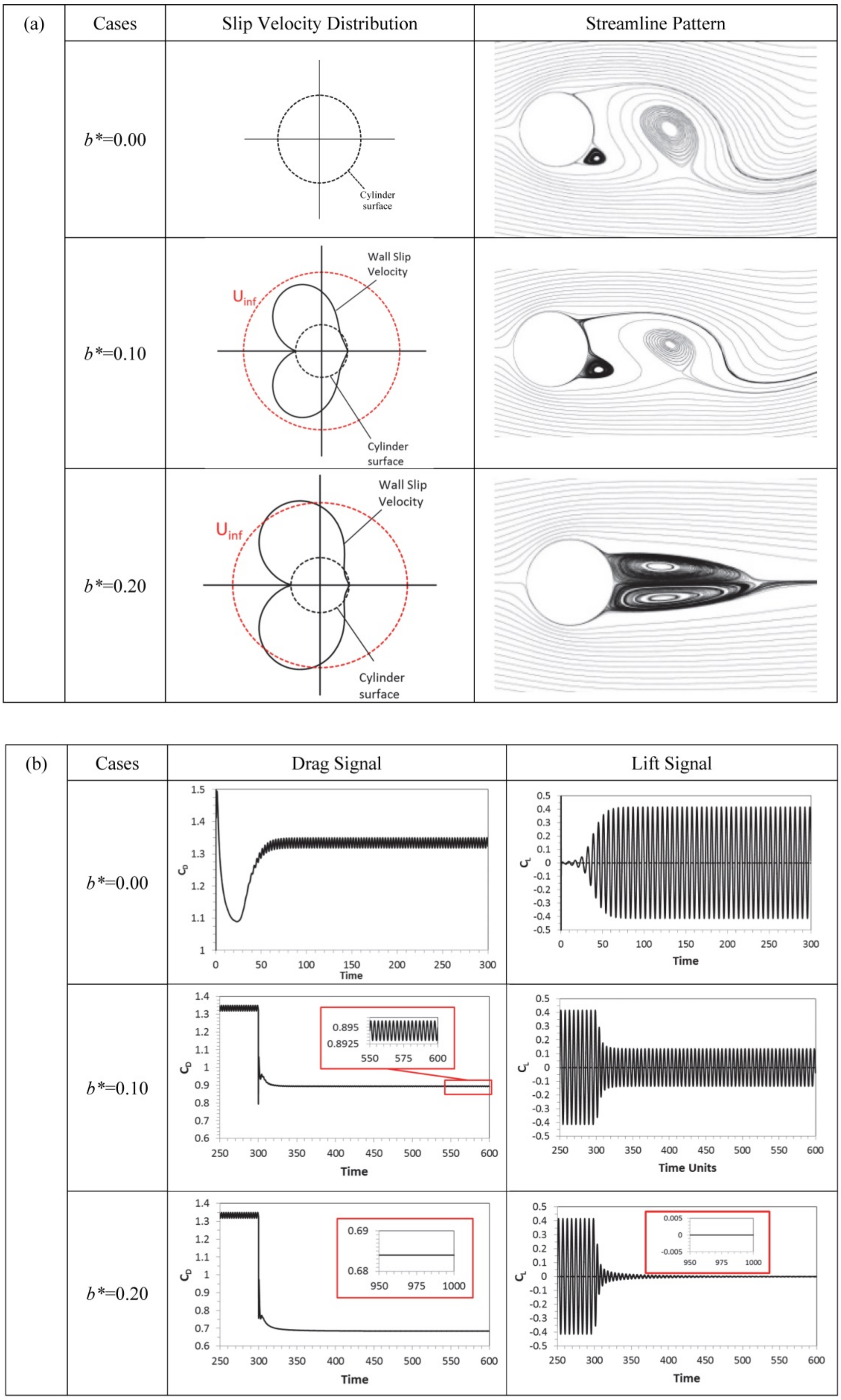

Fig. 18. Computational results for *Re*=120, for uncontrolled flow and for two values of b^*. (a) Base flow slip velocity distributions and instantaneous streamline patterns of asymptotic flow states. (b) Drag and lift coefficient signals. Slip is applied at a no non-dimensional time of 300 units.

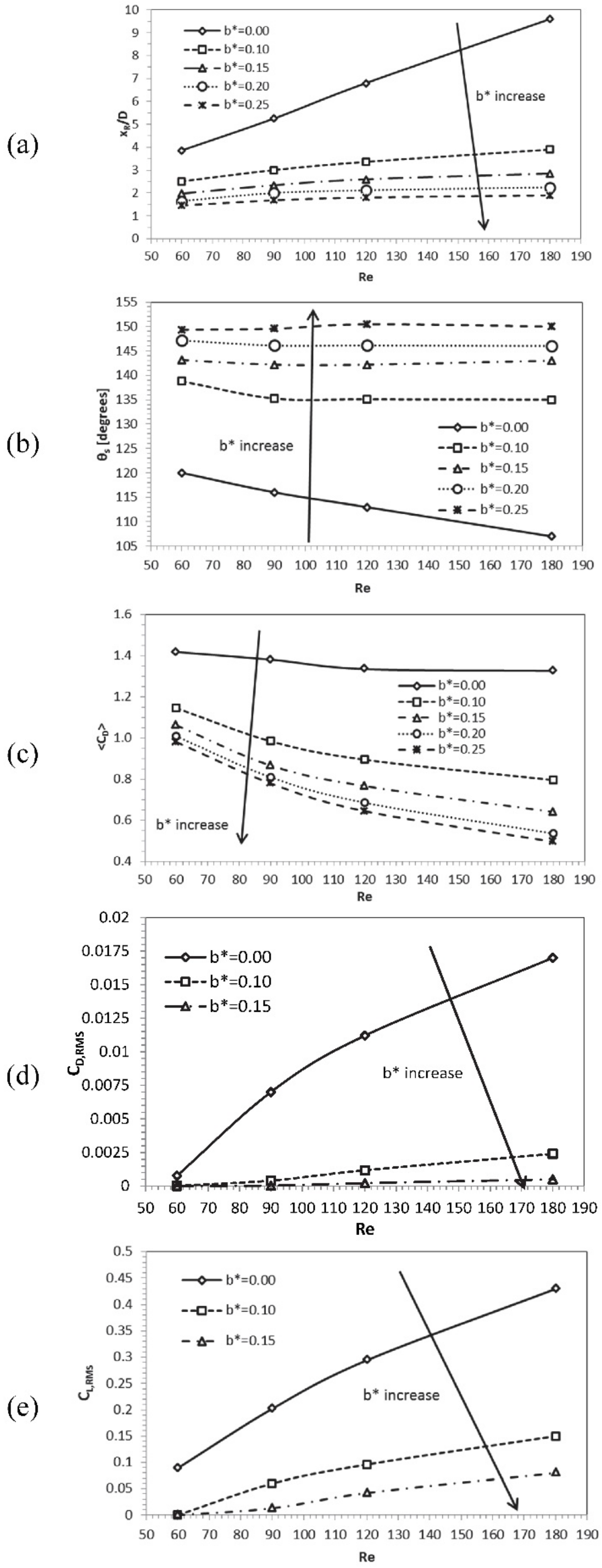

Fig. 19. Flow quantities versus *Re*, for different values of b^*: (a) non-dimensional recirculation length of base flow, (b) base flow separation angle, (c) time-averaged drag coefficient, (d) RMS fluctuation intensity of drag coefficient, and (e) RMS fluctuation intensity of lift coefficient.

3.2 Application of slip on part of the cylinder surface

The slip velocity distributions presented in Fig. 18a demonstrate that slip velocity magnitude remains at low levels in the front and (even lower) in the rear stagnation point region. To further investigate the effect of applying slip in these two regions of low slip velocity, simulations are performed for *Re*=90, in which slip conditions are applied exclusively: (a) on a region extending ±37.5^o from the front stagnation point, (b) on a region extending ±37.5^o from the rear stagnation point; the extent of ±37.5^o is selected taking into account the slip velocity distribution of base flow. In both cases, the representative value of non-dimensional slip length b^*=0.17 is utilized, which corresponds to global flow stabilization at *Re*=90 with application of full slip. Fig. 20 presents the computed wall slip velocity distributions of base flow, as well as lift coefficient time series. For the case of applying slip in the front stagnation point region, the results in Fig. 20 illustrate the presence of slip velocities substantially lower than the free stream velocity, as well as a slight increase in the lift amplitude, which is indicative of a weak destabilizing effect. For the case of applying slip in the rear stagnation point region, Fig. 20 demonstrates the presence of negative slip velocities, and an increase in lift amplitude. This increase is small in comparison to the lift amplitude of uncontrolled flow, nonetheless more pronounced in comparison to the corresponding increase for slip application in the front stagnation point region; thus, the destabilizing effect is stronger in the case of applying slip in the rear stagnation point region. The presence of negative slip velocities in the case of applying slip in the rear stagnation point region suggests that back flow is enhanced in the near wake. This contributes to an enhancement of local absolute instability (Monkewitz 1988), and thus to an enhancement of global flow instability. In summary, applying slip in both the front- and the rear stagnation point region has a destabilizing effect. This suggests that utilizing a hydrophobic surface in these areas could be avoided (use of partial slip), leading to a lower cost in an actual implementation.

Case	Slip Velocity Distribution	Lift Signal
(a) Slip at the Front Stagnation Point Region	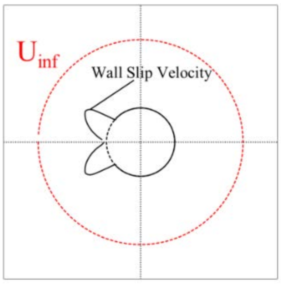	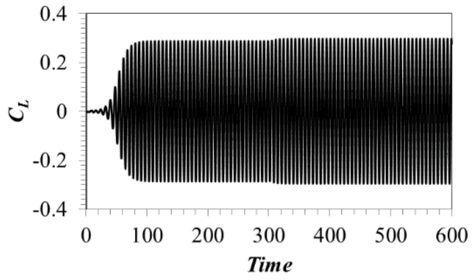
(b) Slip at the Rear Stagnation Point Region	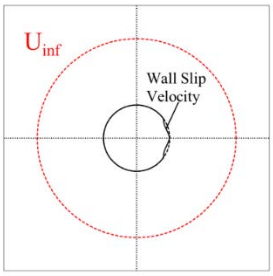	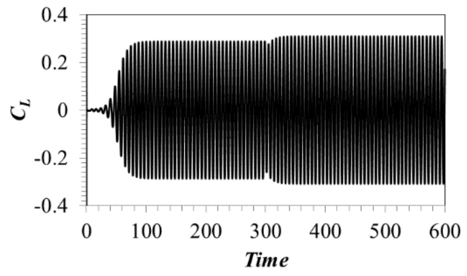

Fig. 20. *Re*=90, b^*=0.17: distribution of slip velocity, u_θ, on the cylinder surface for base flow, and lift coefficient signal, for the cases where slip condition is applied: (a) on a region extending ±37.5^o from the front stagnation point, and (b) on a region extending ±37.5^o from the rear stagnation point. Slip is applied at *t*=300.

To investigate in further detail the effects of implementing partial slip, different variations of slip application were tested at Re=90, for the representative value of non-dimensional slip length b^*=0.17, corresponding to global flow stabilization with application of full slip. Here, it is considered that slip is applied on an arc between angles θ_{min} and θ_{max}, both defined with respect to the front stagnation point (see Fig. 21). Subsequently, four cases are reported, in particular: (a) $\theta_{min}=0^o$, $\theta_{max}=180^o$ (full slip), (b) $\theta_{min}=0^o$, $\theta_{max}=142.5^o$ (no slip in the rear stagnation point region), (c) $\theta_{min}=37.5\ ^o$, $\theta_{max}=180\ ^o$ (no slip in the front stagnation point region), and (d) $\theta_{min}=37.5\ ^o$, $\theta_{max}=142.5\ ^o$ (no slip in both the front- and the rear stagnation point region). Evidently, cases (b) and (c) correspond to equal values of the slip area. Fig. 22 presents results of all four cases, in terms of the slip velocity distribution of base flow, and of the computed lift signal. Fig. 22a, corresponding to full slip, illustrates that the flow becomes steady at large times. Nonetheless, as shown in Fig. 22b, convergence to steady flow is faster for the case of no slip in the rear stagnation point region, i.e. the stabilizing effect of this particular implementation of partial slip is stronger than that of full slip. Fig. 22c shows that, in the case of no slip in the front stagnation point region, global flow stabilization is not achieved, although a substantial reduction in the amplitude of lift fluctuations, of nearly 90%, is attained. Finally, in the case of no slip in both the front and rear stagnation point regimes, the lift coefficient amplitude becomes nearly zero (equals 0.005) at large times (see Fig. 22d). This shows that, while maintaining the value of non-dimensional slip length, flow unsteadiness is practically suppressed by applying slip on an area less than 60% of the full cylinder surface. Overall, these results suggest that: (i) partial slip may be even more effective than full slip in suppressing the global flow instability, and (ii) in a passive control scheme, both angles θ_{min} and θ_{max} should be included as design parameters, for optimizing the control effort necessary for full or partial suppression of the Kármán vortex street.

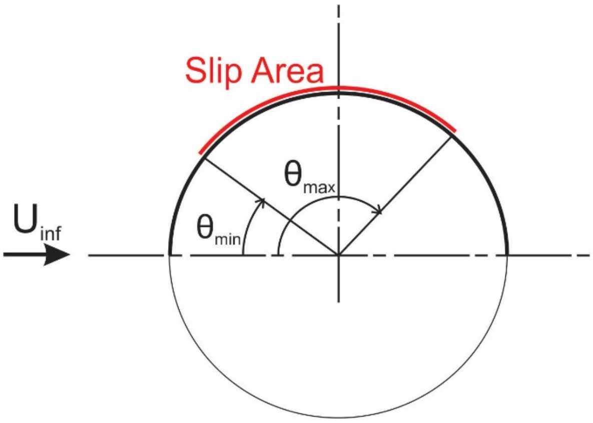

Fig. 21. Sketch of slip condition application on the cylinder surface, for a flow from left to right: slip is applied in the arc ranging from θ_{min} to θ_{max}.

Case	Slip Velocity Distribution	Lift Signal
(a) Full Slip $\theta_{min}=0^o$, $\theta_{max}=180.0^o$ $\theta_s=146^o$	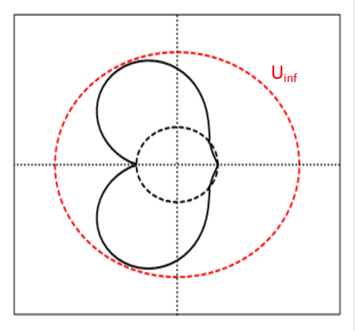	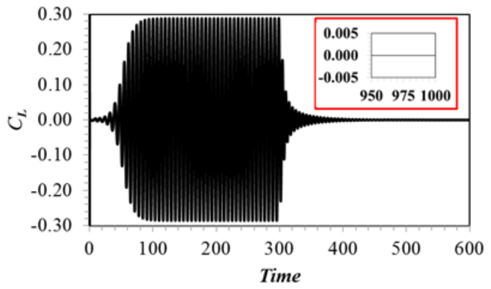
(b) Partial Slip: $\theta_{min}=0^o$, $\theta_{max}=142.5^o$ $\theta_s=146^o$	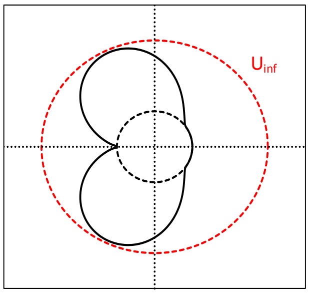	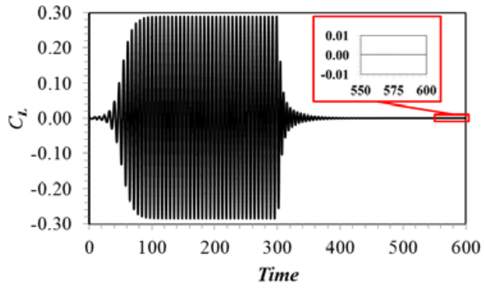
(c) Partial Slip: $\theta_{min}=37.5^o$, $\theta_{max}=180^o$ $\theta_s=142.5^o$	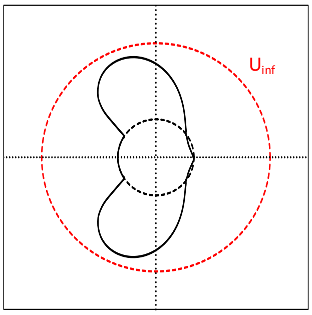	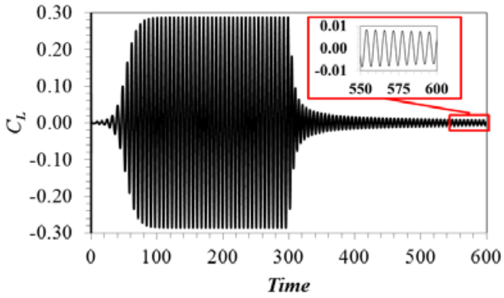
(d) Partial Slip: $\theta_{min}=37.5^o$, $\theta_{max}=142.5^o$ $\theta_s=146^o$	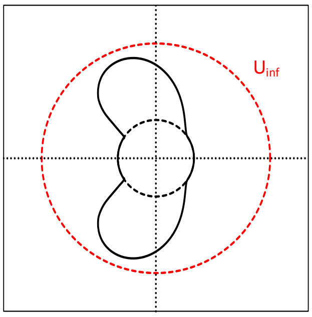	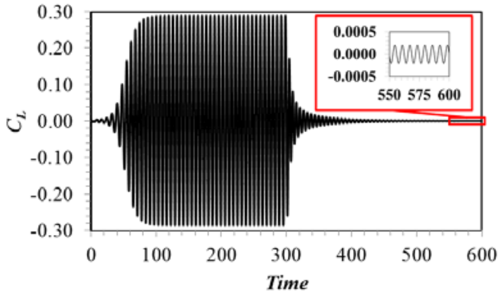

Fig. 22. Re=90, b^*=0.17: distribution of slip velocity, u_θ, on the cylinder surface for base flow, and lift coefficient signal, for the case where slip condition is applied on the entire cylinder surface and for three cases with partial slip. Slip is applied at t=300. The corresponding values of base flow separation point angle, θ_s, are also reported.

3.3 Flow past a partially hydrophobic cylinder: formulation and solution of optimization problem

The main goal of the present section is to attain optimal complete suppression or intensity reduction of the Kármán vortex street in flow past a cylinder, by means of a proper implementation of partial slip. The partial slip parameters consist of the corresponding cylinder arc, defined by θ_{min} and θ_{max} (see Fig. 21), and the corresponding non-dimensional slip length, b^*. Here, an optimal passive control is sought, associated with attaining desired flow states at a minimal control effort. To this end, a two-objective minimization problem is formulated. The first objective function is associated with the flow's global stability, while the second one quantifies the control effort, taking into account the slip length, b^*, and the extent of the slip region, which corresponds to the angle $\varphi=\theta_{max}-\theta_{min}$. Optimization results are reported for two values of Reynolds number, Re=90 and Re=180.

3.3.1 Design variables and search space

Three design variables are utilized in the present implementation: the non-dimensional slip length, b^*, and the angles θ_{min} and θ_{max}, defining the slip area. The application of slip is symmetrical with respect to the domain centerline (y=0). A broad domain of definition is considered for each of the three design variables:

$$0 \le b^* \le 0.5,\ 0 \le \theta_{\min} \le 70^o,\ 110^o \le \theta_{\max} \le 180^o \tag{31}$$

The selection of search space boundaries was guided by the simulations reported in section 3.2, corresponding to implementation of full and partial slip.

3.3.2 Objective functions

Two objective functions are introduced.

(a) First objective function, J_1:

The first objective function, J_1, is related to the flow's global stability. Here, a total of M points along the domain centerline (y=0) is considered, and the numerical signal of the transverse velocity (V-component) at large times is analyzed, for each point. For a total of N data points in time (N being a very large number, corresponding to several flow periods), the objective function J_1 is defined as the average of the standard deviation values, S_j, of the V-velocity signals, in the population of M points:

$$\overline{V_{x_j}} = \frac{1}{N}\sum_{i=1}^{N} V_{t_i,x_j} \tag{32}$$

$$S_j = \sqrt{\frac{1}{N-1}\sum_{i=1}^{N}\left(V_{t_i,x_j} - \overline{V_{x_j}}\right)^2} \tag{33}$$

$$J_1 = \frac{1}{M}\sum_{j=1}^{M} S_j \tag{34}$$

where V_{t_i,x_j} is the transverse velocity at point x_j calculated at time instant t_i, $\overline{V_{x_j}}$ the corresponding time-averaged value, and S_j its standard deviation at point x_j. In the present study, M=100, corresponding to equidistant points in the wake region $1<x/D<21$.

Unsteady wakes are characterized by non-zero instantaneous V-velocities along the wake centerline, with the magnitude of velocities being representative of the intensity of the global mode. On the other hand, steady wakes are symmetric along their centerline (V=0). Thus, the value of J_1 is expected to decrease for control actions corresponding to increased stabilizing effects, becoming zero for steady flow.

(b) Second objective function, J_2:

The second objective function, J_2, defines the control effort, which increases with both the non-dimensional slip length, b^*, and the normalized half-arc of the slip region. Thus, their product is taken as the objective function J_2:

$$J_2 = b^* \frac{(\theta_{\max} - \theta_{\min})}{2} = \frac{1}{2} b^* \varphi \tag{35}$$

where $\varphi = \theta_{max} - \theta_{min}$ is expressed in radians.

3.3.3 Optimization problem

The present optimization problem is stated as follows: find the optimum combinations of the problem design variables (b^*, θ_{min}, θ_{max}), which simultaneously minimize objective functions J_1, J_2. The optimization problem, as formulated here, is solved for two representative values of Reynolds number, Re=90 and Re=180, i.e. in a Reynolds number regime where the flow is two-dimensional.

3.3.4 Optimization methods

In the present optimization problem, each individual corresponds to a different slip condition (b^*), applied on a different part of the cylinder surface (defined by θ_{min}, θ_{max}), and is rated based on the resulting values of the problem objective functions. Here, the evaluator, finally giving the values of objective functions, is the CFD code ANSYS CFX, which is coupled to the optimization tool; the latter utilizes the ParadisEO genetic algorithms library (Cahon et al. 2004), and adopts the Non–dominated Sorting Genetic Algorithm NSGA-II for ranking solutions within a generation (Deb et al. 2002). The entire procedure for optimizing the partial slip setup is outlined in Fig. 23. In the present implementation, each generation consisted of 20 individuals. Each optimization problem converged to the final Pareto front after 22 generations. An individual CFD run has required approximately 2.5 hours of turnaround time, on 24 cores of a parallel cluster.

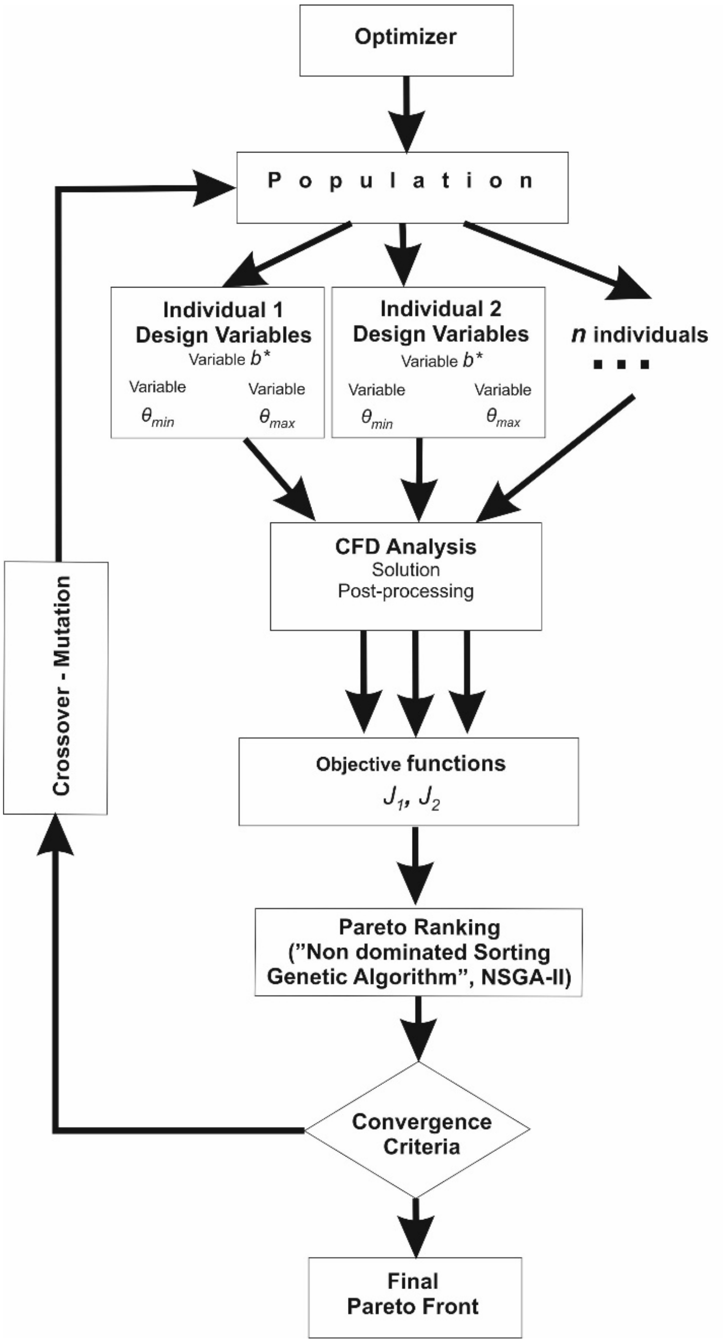
Optimizer
Population
Individual 1 Design Variables
Variable b*
Variable θmin
Variable θmax
Individual 2 Design Variables
Variable b*
Variable θmin
Variable θmax
n individuals
CFD Analysis
Solution
Post-processing
Objective functions
J1, J2
Pareto Ranking
("Non dominated Sorting Genetic Algorithm", NSGA-II)
Convergence Criteria
Final Pareto Front
Crossover - Mutation

Fig. 23. Optimization flow chart.

3.3.5. Optimization results

3.3.5.1 Optimization results for Re=90

The optimization results for *Re*=90 are presented in Fig. 24, in terms of the values of the problem objective functions, J_1, J_2. Each combination of the problem design variables (b^*, θ_{min}, θ_{max}) corresponds to a different slip setup, resulting in either unstable or stable flow (values of function J_1 positive or zero, respectively). Fig. 24 demonstrates that, in the set of optimal solutions, an increase in control effort results in a more stable flow (decrease of J_1). Results for full slip cases have been also added in Fig. 24; the decrease in control effort (J_2 value) of corresponding optimal flow cases (same level of J_1) is depicted in Fig. 24.

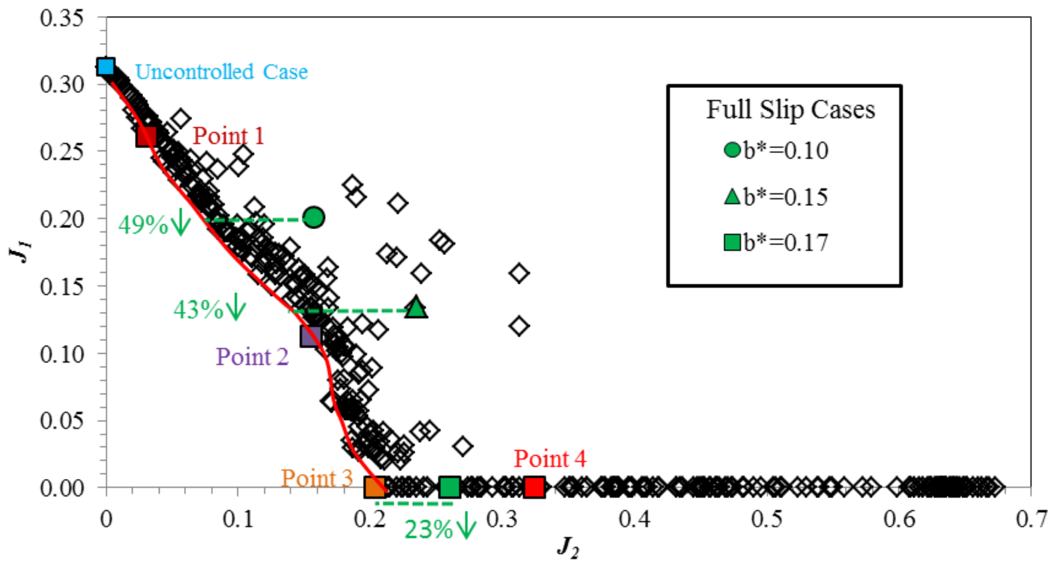

Fig. 24. *Re*=90: objective function J_1 vs. objective function J_2, and sketch of the corresponding Pareto front. Three cases of full slip are also included and are compared to the corresponding optimal cases of partial slip, with the decrease in control effort highlighted.

Four representative solutions of the Pareto front, as well as the case of uncontrolled flow, are highlighted in Fig. 24 with colored squares. The corresponding design variable and objective function values are reported in Table 2, also including the case of stabilized flow with full slip at minimum b^*. Further, the corresponding values of average drag coefficient, $<C_D>$, and lift coefficient amplitude, $C_{L,ampl}$, are presented in Table 3. For these representative solutions Fig. 25 presents the distribution of wall slip velocity in the base flow, as well as instantaneous vorticity contours, while Fig. 26 presents the computed signals of drag and lift coefficient. Fig. 26 demonstrates a rapid decrease of the drag coefficient after implementing the slip condition, i.e. by inducing high magitude slip velocities. The latter results in moving the separation point toward the rear stagnation point, as well as in a drastic reduction of the local values of shear stresses on the cylinder surface. Therefore, an increase in the slip length results in: (a) a rapid reduction of the pressure drag force, due to the corresponding decrease of the fore-aft asymmetry of the pressure distribution, caused by the increase in the separation point angle, and (b) a rapid reduction of the viscous drag force, due to the reduction of the local shear stresses. Thus, the steep decrease in drag force is caused by the substantial decrease in both of its components. Table 2 indicates that, for the optimal solutions considered, the increase in control effort mainly consists in an increase in slip length, b^*. As illustrated in Table 3, at increasing control effort, the lift oscillation amplitude decreases, becoming zero in the limit of global flow stabilization, while, due to the narrower wakes, a corresponding decrease of the average drag is also found. The variation of all three design variables along the Pareto front is presented in Fig. 27, in which stabilized flows correspond to squares. Fig. 27 verifies a more pronounced increase in the first component of the control effort, b^*, in comparison to the second one, φ, at increasing total control effort (J_2). In particular, regarding φ, its increase is due to the rapid increase in θ_{max}, which surpasses an average mild increase in θ_{min}. Finally, Fig. 27 illustrates that the increase in control effort delays flow separation in the base flow, which in turn reduces fluctuation intensities of the non-linear flow, and stabilizes the flow at a critical level of control effort.

In more detail, the solution giving global flow stabilization at a minimum control effort (Point 3 of Fig. 24) has a slip length value of b^*=0.207, higher than the one corresponding to stabilization with full slip (b^*=0.17). The decreased control effort in the former case is evidently due to the significant decrease of the hydrophobic region (extending from θ_{min}=33.57^o to θ_{max}=146.08^o). Thus, the drawback of a slightly higher value of slip length is counterbalanced by the decreased extent of the superhydrophobic surface, giving a reduction in control effort of 23%.

It is noted that, with current technology, a realistic value of slip length using superhydrophobic materials is of the order of 100 μm. Thus, in the case of implementing steady slip conditions at Re=90, vortex street cancellation is attained for cylinder diameters up to about D=0.58 mm for the full slip case (b^*=0.17), and up to D=0.48 mm for the optimal partial slip case (b^*=0.207).

Table 2. Re=90: design variable values and corresponding objective function values, for the uncontrolled case, as well as for solutions 1 to 4 and the case of stabilized flow with full slip, depicted in Fig. 24.

Case	b^*	θ_{min}	θ_{max}	$\varphi=\theta_{max}-\theta_{min}$	J_1	J_2
Uncontrolled	0.000	0.00^o	0.00^o	0.00^o	0.319	0.000
Point 1	0.041	40.89^o	129.19^o	88.29^o	0.261	0.031
Point 2	0.196	49.10^o	140.16^o	91.06^o	0.112	0.156
Point 3	0.207	33.57^o	146.08^o	112.51^o	0.000	0.203
Point 4	0.303	37.31^o	159.80^o	122.49^o	0.000	0.324
Full slip, stabilized flow	0.170	0.00^o	180.00^o	180.00^o	0.000	0.260

Table 3 Re=90: time-averaged values of drag coefficient, $<C_D>$, and amplitude of lift coefficient, $C_{L,ampl}$, for the uncontrolled case, as well as for solutions 1 to 4 and the case of stabilized flow with full slip, depicted in Fig. 24.

Case	$<C_D>$	$C_{L,ampl}$
Uncontrolled	1.3800	0.352
Point 1	1.1950	0.224
Point 2	0.9079	0.025
Point 3	0.8300	0.000
Point 4	0.7900	0.000
Full Slip, Stabilized Flow	0.8260	0.000

Case	Slip Velocity Distribution	Vorticity Isocontours
Uncontrolled Flow	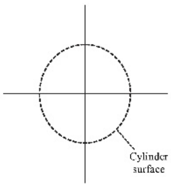	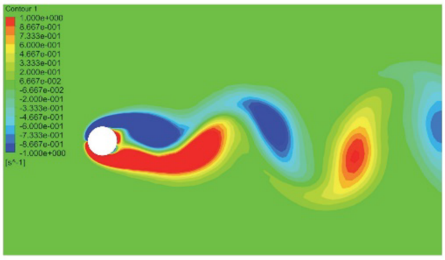
Point 1	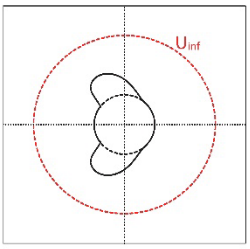	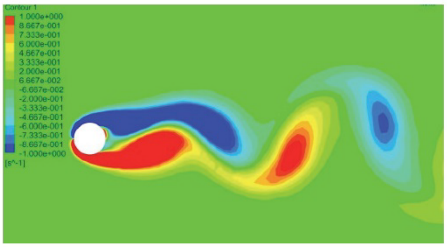
Point 2	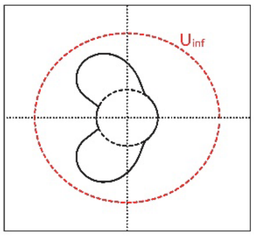	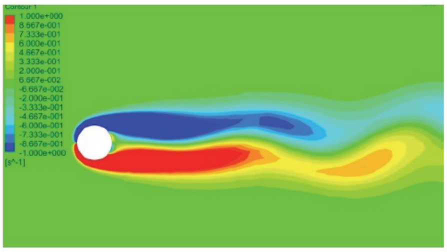
Point 3	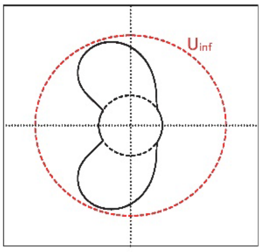	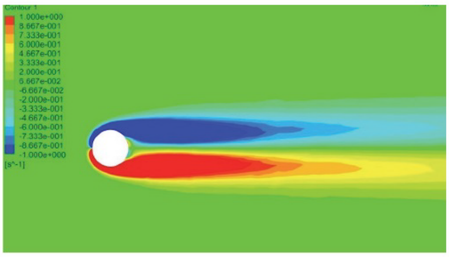
Point 4	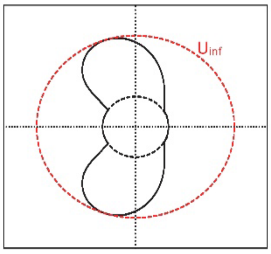	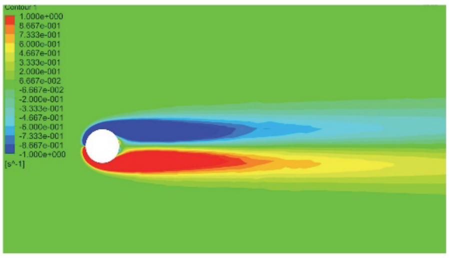
Full Slip, Stabilized Flow	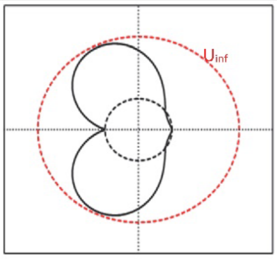	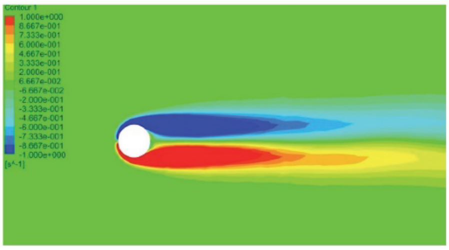

Fig. 25. *Re*=90: computed slip velocity profiles of base flow corresponding to solutions 1 to 4, the uncontrolled case and the case of stabilized flow with full slip, depicted in Fig. 24 (left column), and color-coded contours of instantaneous vorticity in the non-linear flow state (right column).

Case	Drag Signal	Lift Signal
Uncontrolled	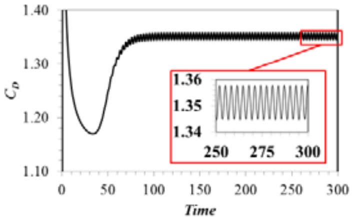	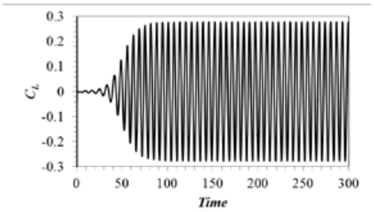
Point 1	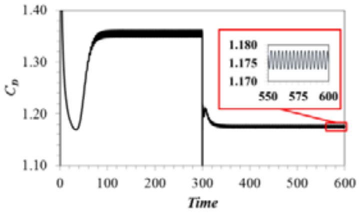	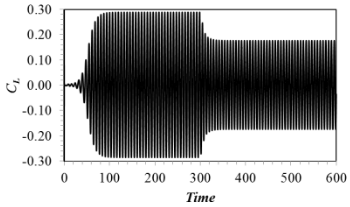
Point 2	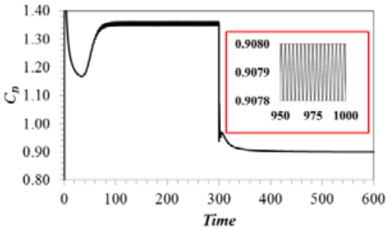	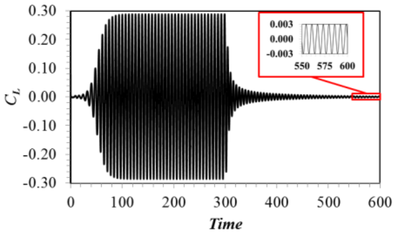
Point 3	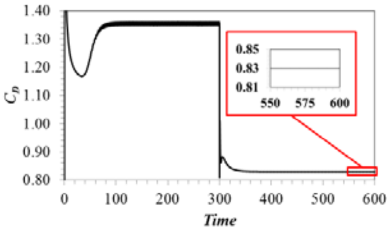	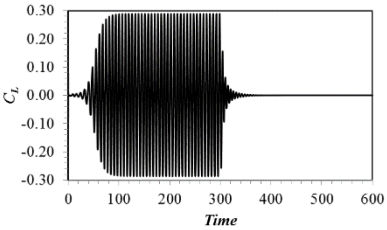
Point 4	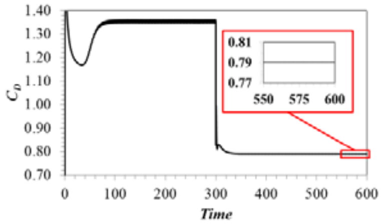	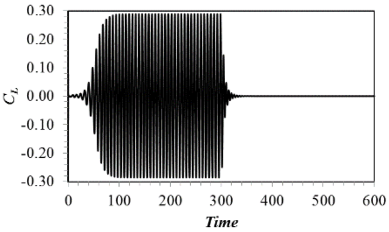
Full Slip, Stabilized Flow	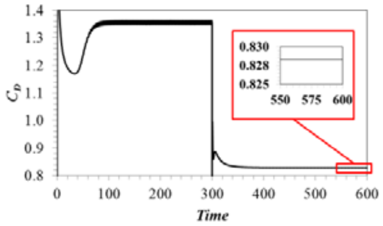	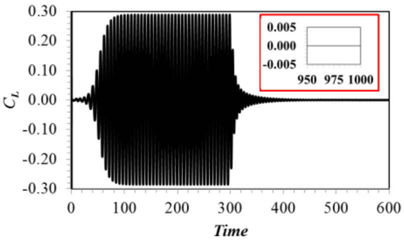

Fig. 26. *Re*=90: Drag and lift coefficient signals for solutions 1 to 4, the uncontrolled case and the case of stabilized flow with full slip, depicted in Fig. 24. Passive control is implemented at *t*=300.

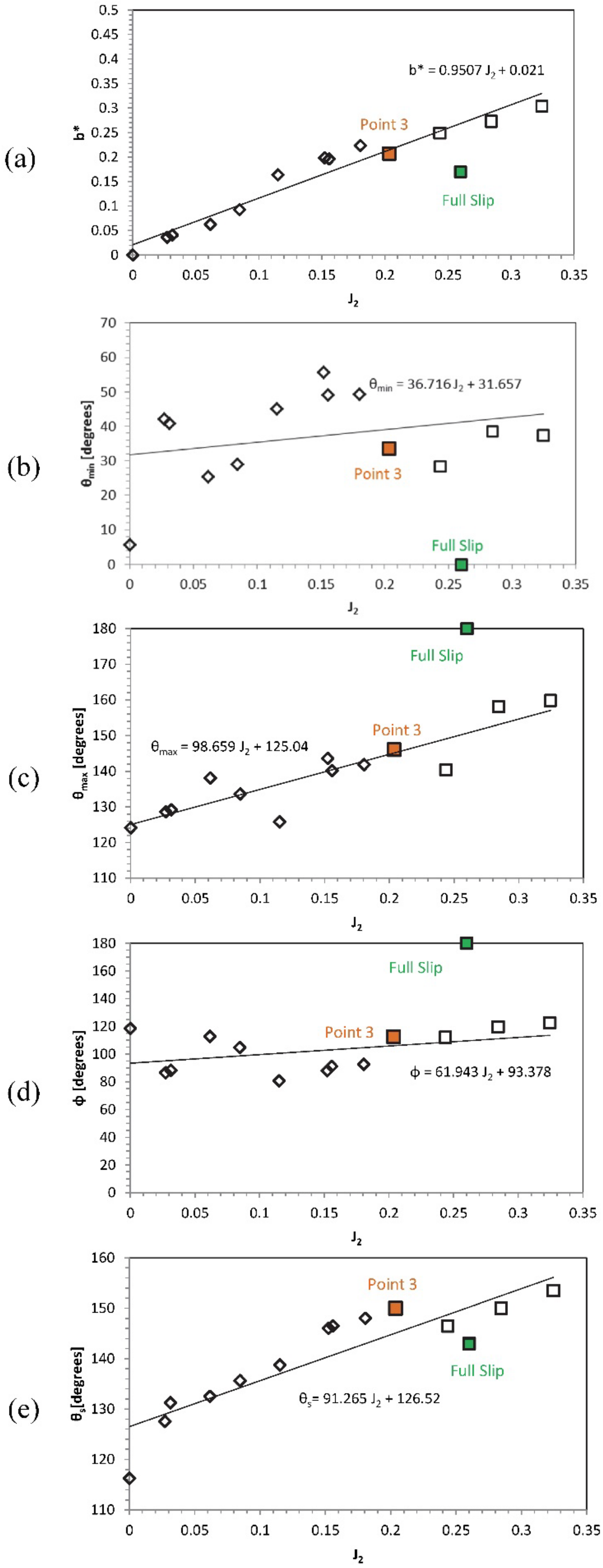

Fig. 27. *Re*=90: design variables and separation point angle of base flow versus objective function J_2, for solutions along the Pareto front. The case of stabilized flow with full slip is also included.

3.3.5.2 Optimization results for Re=180

Fig. 28 presents the computed objective function values for *Re*=180, also including a sketch of the Pareto front. In comparison to *Re*=90 (Fig. 24), a higher control effort (J_2) to arrive at a corresponding flow state, expressed by the value of J_1, is confirmed. Four cases corresponding to application of full slip have been added in Fig. 28, illustrating an increase in the required control effort, in comparison to cases of the Pareto front, to arrive at the same level of J_1. Further, four representative solutions of the Pareto front, as well as the one corresponding to uncontrolled flow, are depicted in Fig. 28. Table 4 includes the values of design variables and objective functions of these optimal cases, as well as the values corresponding to the case of stabilized flow with full slip at minimum b^*; the corresponding slip velocity distributions of base flow, as well as vorticity contours of instantaneous non-linear flow, are presented in Fig. 29. Fig. 29 demonstrates a substantial increase in slip velocities at increasing control effort, J_2. The vorticity contours are indicative of the corresponding return of the flow to a globally stable state.

Regarding global flow stabilization at minimum control effort (Point 3 of Fig. 28), it is associated with a slip length of $b^*=0.298$, implemented from θ_{min}=25.09° to θ_{max}=145.55°, giving J_2=0.314 (Table 4); in comparison to the full slip case, the control effort for flow stabilization (expressed by J_2) is reduced by 20%. A comparison with the optimization results for *Re*=90 (Table 2), shows that, at *Re*=180, optimal flow stabilization with partial slip requires an increase in control effort (J_2) of approximately 35%.

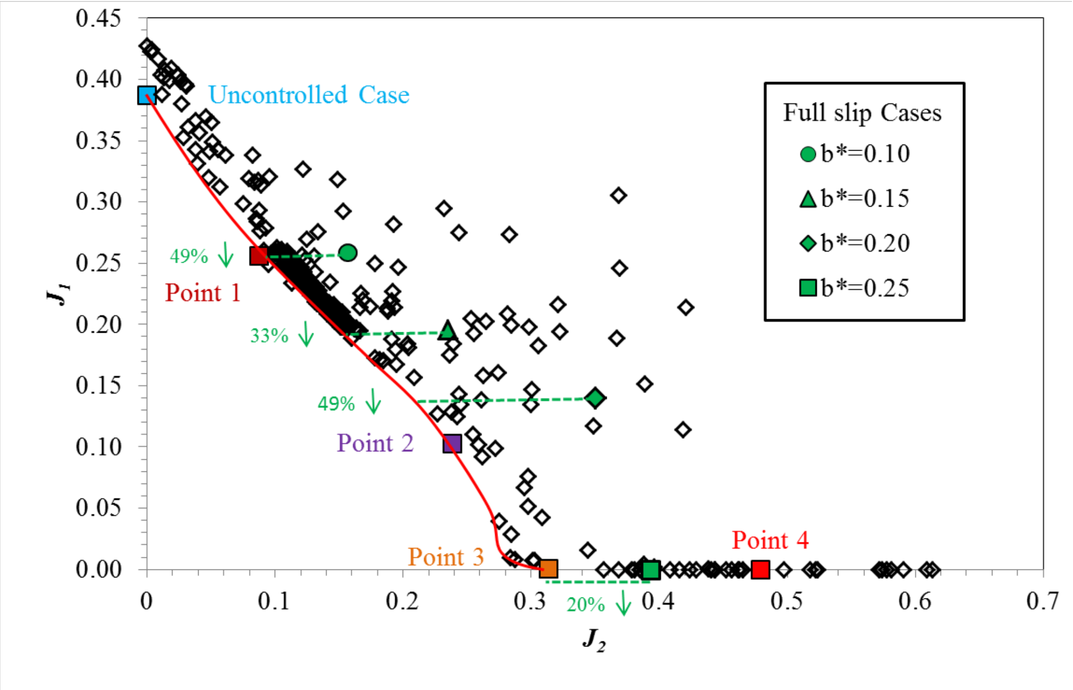

Fig. 28. *Re*=180: objective function J_1 vs. objective function J_2, and sketch of the corresponding Pareto front. Four cases of full slip are also included and are compared to the corresponding optimal cases of partial slip, with the decrease in control effort highlighted.

Case	Slip Velocity Distribution	Vorticity Isocontours
Uncontrolled Flow	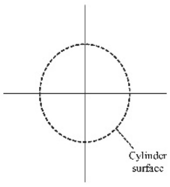	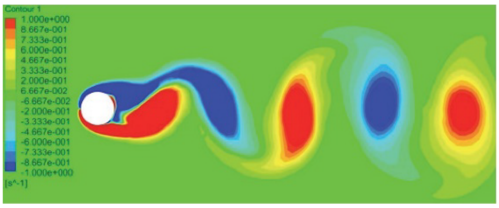
Point 1	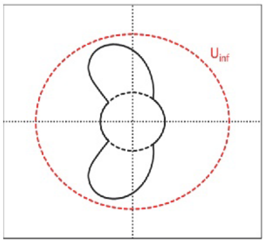	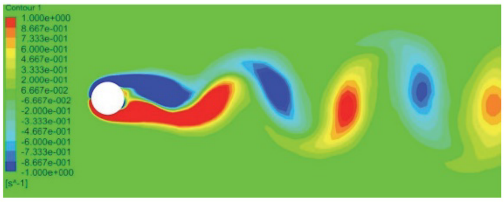
Point 2	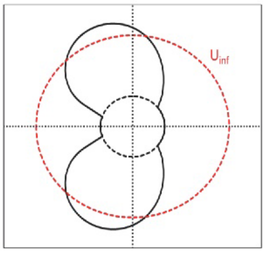	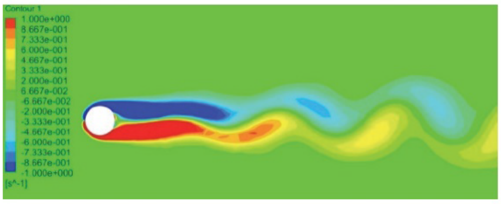
Point 3	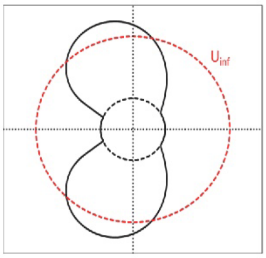	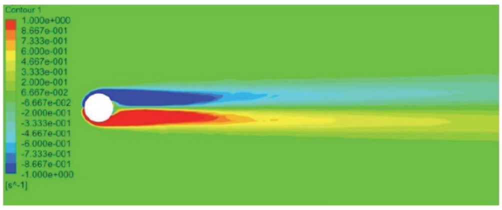
Point 4	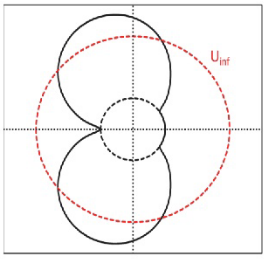	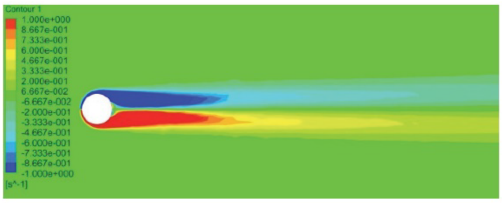
Full Slip, Stabilized Flow	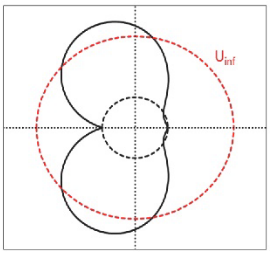	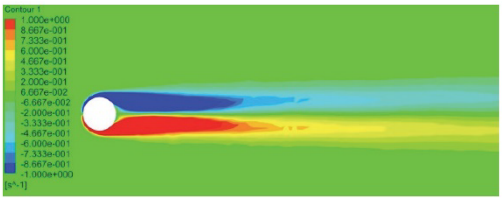

Fig. 29. *Re*=180: computed slip velocity profiles of base flow corresponding to solutions 1 to 4, the uncontrolled case and the full slip case, depicted in Fig. 28 (left column), and color-coded contours of instantaneous vorticity in the non-linear flow state (right column).

Table 4. Re=180: design variable values and corresponding objective function values, for the uncontrolled case, as well as for solutions 1 to 4 and the full slip case, depicted in Fig. 28.

Case	b^*	θ_{min}	θ_{max}	$\varphi=\theta_{max}-\theta_{min}$	J_1	J_2
Uncontrolled	0.000	0.00	0.00	0.00	0.387	0.000
Point 1	0.125	46.80	126.41	79.61	0.256	0.087
Point 2	0.238	23.34	138.19	114.84	0.102	0.238
Point 3	0.298	25.09	145.55	120.45	0.000	0.314
Point 4	0.399	3.56	141.12	137.56	0.000	0.479
Full slip, stabilized flow	0.250	0.00	180.00	180.00	0.000	0.393

3.4 Characterization of flow instability

In this section, results of linear local and global stability analysis calculations, outlined in section 1.4, are presented, for representative base flow fields, at Re=90. In particular, optimal solutions corresponding to different levels of control effort, as well as the cases of uncontrolled flow and stabilized flow with full slip at a minimum value of b^*, are analyzed. This analysis aims at a characterization of the stability of controlled flow, at different levels of optimal control action.

3.4.1 Linear local instability analysis

Firstly, the local wake profile parameters, i.e. the velocity ratio and the vorticity thickness, defined in section 1.4, are calculated. Next, these values are associated with the results of Monkewitz and Nguyen (1987) regarding stability of parallel wakes.

In particular, Fig. 30a and Fig. 30b present the values of velocity ratio, R, and non-dimensional vorticity thickness, δ_w/D, respectively, at different streamwise locations, x/D. Clearly, an increase in control effort, J_2, results in decreased velocity ratio values (reduced backflow), as well as in a decrease in vorticity thickness; backflow in the near wake is decreased due to the delay of separation (increase of separation point angle, θ_S). Further, the velocity profiles extracted from each base flow field, for different streamwise locations, x/D, are curve-fitted with reference to a two-parameter (R, N) profile, introduced by Monkewitz and Nguyen (1987) (see section 1.4.1). In Fig. 30c, the corresponding pairs (R, $1/N$) are placed on the plot of Monkewitz and Nguyen (1987), also presented in section 1.4.1 (Fig. 5b); this enables the identification of the extent of the region of absolute instability, an provides an indication of the relative magnitude of growth rates (distance from the absolute/convective instability border). Fig. 30c suggests that both the extent and intensity of absolute instability decrease at increasing control effort.

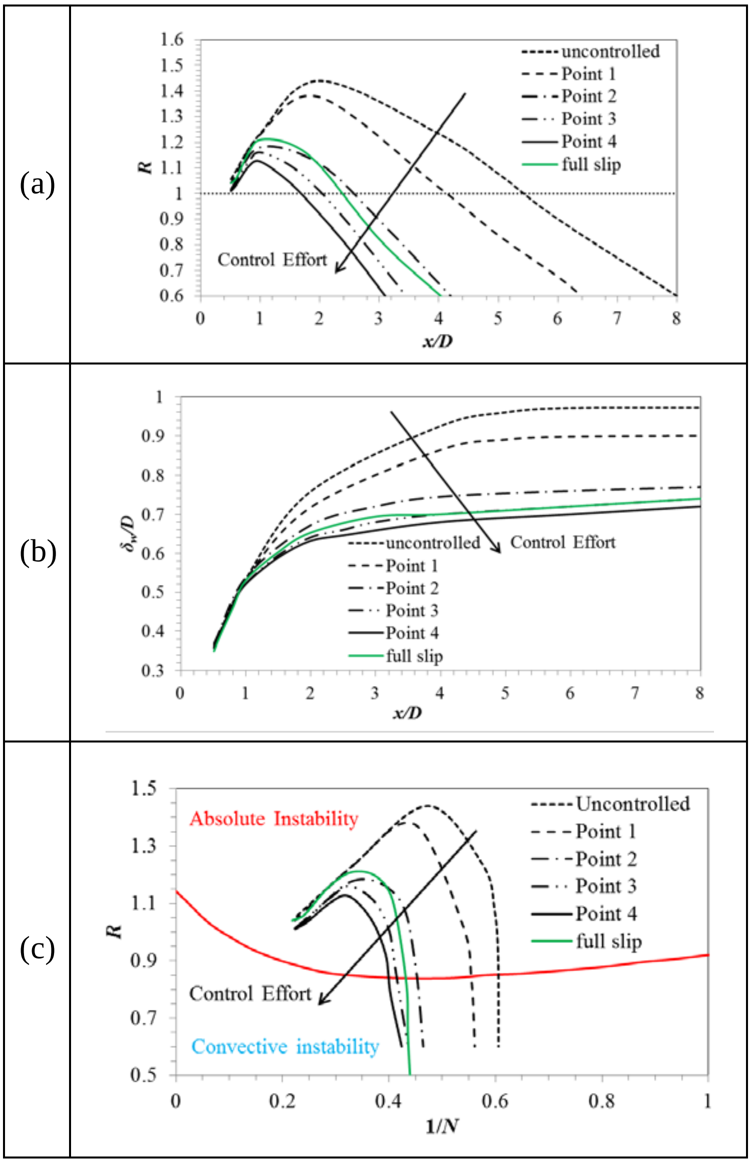

Fig. 30. *Re*=90: characterization of streamwise velocity profiles, for solutions 1 to 4, the uncontrolled case and the case of stabilized flow with full slip, depicted in Fig. 24. These solutions correspond to different levels of control effort, expressed in terms of the objective function J_2. (a) Velocity ratio vs. streamwise coordinate, (b) vorticity thickness vs. streamwise coordinate, and (c) velocity ratio vs. profile parameter 1/*N*.

Furthermore, normal mode local stability analysis calculations are performed, based on the procedure outlined in section 1.4.1. The computed values of absolute local linear frequency, $St_0=\omega_{0,r}/(2\pi)$, and asolute growth rate, $\omega_{0,i}$, are presented in Fig. 31. Fig. 31 shows that an increase in control effort, J_2, results in an increase of local linear frequency; its maximum and minimum values in the near wake ($x/D < 10$), $St_{0,max}$ and $St_{0,min}$, are presented in Table 5. The increasing trend of local linear absolute frequency curve, $St_0(x/D)$ with control effort, evident in Fig. 31, is in accordance with the corresponding increasing trend of the flow Strouhal number, reported in Table 5. Moreover, Fig. 31 demonstrates that the increase in control effort results in decreasing both the extent of the absolutely unstable regime, $x_a - x_b$, and the values of absolute growth rates; the maximum value of each case, $\omega_{0,i,max}$, is reported in Table 5. Finally, local instability quantities are associated with global flow unsteadiness by applying the criterion of Chomaz et. al (1990), introduced in equation (15) of section 1.4.1; the results of Table 5 show that the integral I_g attains a value close to 0.5 for solutions corresponding to global flow stabilization.

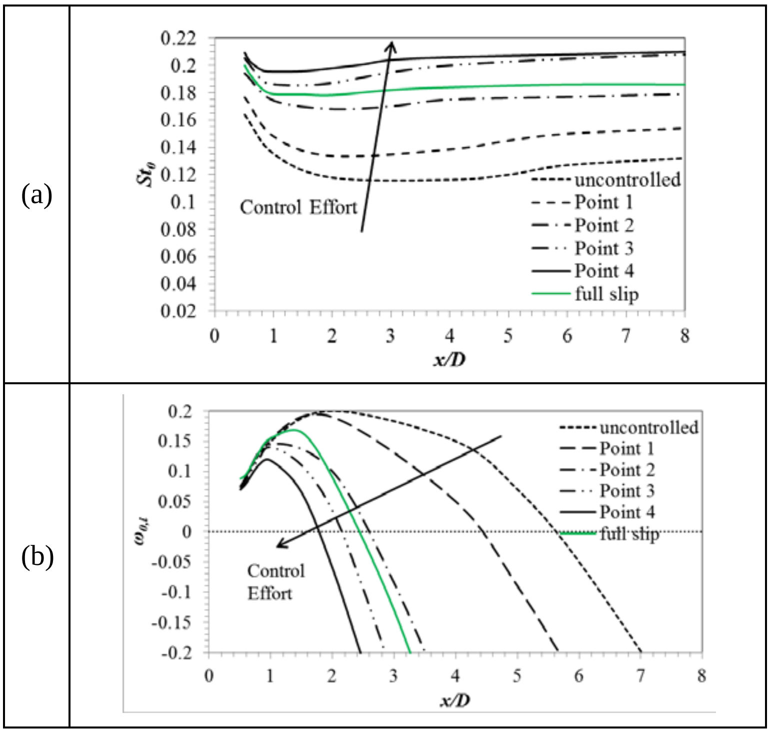

Fig. 31. *Re*=90: values of local stability properties vs. streamwise coordinate, for solutions 1 to 4, the uncontrolled case and the case of stabilized flow with full slip, depicted in Fig. 24. These solutions correspond to different levels of control effort, expressed in terms of the objective function J_2. (a) Absolute frequency, and (b) absolute growth rate.

3.4.2 Linear global instability analysis

Transient lift coefficient signals are analyzed following the signal analysis procedure outlined in section 1.4.2, yielding the values of global linear growth rate, σ_r, and global linear frequency, σ_i. Results are presented in Table 5, and are in accordance with the numerical simulation results (positive and negative growth rate values for oscillatory and steady flow, respectively). Table 5 indicates that the global linear frequency of Pareto front solutions increases at increasing control effort, in accordance with the trend in Strouhal number. The present results also illustrate the proximity of linear and non-linear global frequency in the limit of global flow stabilization.

Table 5. Quantities characterizing the flow local and global stability, for representative solutions of the optimization problem at *Re*=90.

Case	Global linear frequency, $s=\sigma_r+i\sigma_i$		*St*	Local linear frequency range (*x/D*<10)		$I_g=\int_{x_a}^{x_b}\sqrt{\omega_{0,i}(x)}dx$ $\omega_{0,i}(x)>0$		
	σ_r	$St_{g,l}=\frac{\sigma_i}{2\pi}$		$St_{0,\min}$	$St_{0,\max}$	$\omega_{0,i\,max}$	x_b-x_a	I_g
Uncontrolled Flow	0.0898	0.1282	0.158	0.118	0.165	0.200	5.3	1.89
Point 1	0.0715	0.1351	0.161	0.135	0.178	0.195	4.1	1.35
Point 2	0.0002	0.1601	0.163	0.168	0.195	0.140	2.3	0.65
Point 3	-0.0357	0.1739	-	0.185	0.207	0.145	1.7	0.48
Point 4	-0.0651	0.1851	-	0.195	0.210	0.120	1.3	0.34
Full slip	-0.0078	0.1754	-	0.178	0.200	0.168	2.1	0.59

3.5 Summary of chapter 3

In this chapter we investigated computationally the problem of passive control of flow past a circular cylinder at low Reynolds numbers, by means of partial (and full) slip. Guided by initial CFD simulations, an optimization problem was formulated aiming at partially or fully suppressing the Kármán vortex street at a minimum control effort. To this end, a multi-objective optimization tool was developed, by coupling a CFD code with an optimization code based on genetic algorithms. Here, the control effort has been quantified in terms of the product of slip length and the extent of the hydrophobic regime. The optimization results have demonstrated that optimal application of partial slip is more effective than full slip in suppressing flow unsteadiness. In particular, compared to full slip, optimal application of partial slip can result in a decrease of control effort by up to 50%. The stability properties of the computed optimal base flow fields have been characterized by both local and global stability calculations. It was demonstrated that the increase of the control effort results in decreased values of velocity ratio and vorticity thickness in the near wake region. As a consequence, both the streamwise extent of absolute instability and local absolute growth rates are decreased, leading to suppression of non-linear flow oscillations, and global flow stabilization at a critical level of control effort.

Chapter 4: Flow control by means of mass transpiration

In the present chapter an active open-loop control scheme is implemented by means of mass transpiration (suction/blowing) on the cylinder surface. First, suction/blowing is applied on three regimes of the cylinder surface, in particular: (a) in the front stagnation point region, (b) in the sideway region, and (c) in the rear stagnation point region; the effects of suction/blowing on the global flow stability are assessed. Guided by these results, an optimization problem is formulated and solved, aiming at the partial or full suppression of the Kármán vortex street at a minimal control effort. Here, proper combinations of uniform suction and blowing profiles are utilized, under the constraint of a zero net transpiration flow rate; the latter is associated with the goal of minimizing the pumping requirements. The goal of optimization is to arrive at proper transpiration profiles (on the entire cylinder surface), which minimize simultaneously two appropriate objective functions. The first objective function characterizes the flow unsteadiness, whereas the second one quantifies the control effort in terms of the absolute value of the suction/blowing flow rate. Finally, the computed optimal solutions are characterized by means of local and global instability calculations.

4.1. Implementation of piecewise uniform suction/blowing

The present implementation of mass transpiration (suction/blowing) builds on ideas introduced in previous literature studies (Delaunay and Kaiktsis, 2001, Dong et al., 2008). In order to validate the present control scheme, a steady control action is implemented, corresponding to the one of Delaunay and Kaiktsis (2001). In particular, a uniform (top-hat) suction/blowing profile is implemented for an angle of $\pm 22.5^o$ with respect to the rear stagnation. It is noted that, in the work of Delaunay and Kaiktsis (2001), the suction/blowing velocity profile is uniform over most of the arc used, whereas a smooth profile (cubic function of the angle, with zero derivatives at the two boundaries) is prescribed close to the two boundaries. For *Re*=90 and blowing implemented in the rear stagnation point regime, results of the present simulations are presented in Table 6 in terms of the Strouhal number and the time-averaged value of the drag coefficient for four values values of the suction coefficient, C_{suc}, and are compared against those of Delaunay and Kaiktsis (2001). The very good agreement obtained validates the present results, and also shows that the two set-ups are effectively the same, i.e. the present uniform transpiration velocity profile induces the same dynamics as the smooth profile of Delaunay and Kaiktsis (2001).

Table 6. *Re*=90: Computed values of statistical flow quantities, at different values of the suction coefficient, C_{suc}, for the present and a previous study (Delaunay and Kaiktsis, 2001); computed values: time-averaged drag coefficient and Strouhal number.

	Present study		Delaunay and Kaiktsis, 2001	
C_{suc}	$<C_D>$	*St*	$<C_D>$	*St*
0	1.380	0.158	1.392	0.159
-0.050	1.275	0.151	1.321	0.154
-0.100	1.210	0.142	1.232	0.144
-0.145	1.175	-	1.185	-

In the present study, a combination of suction and blowing is implemented on the cylinder surface, aiming at the cancelation of the vortex street. In particular, three regimes on the cylinder surface are considered, whose limits have been identified based on a preliminary computational investigation: (a) the front stagnation point region, $0^o<\theta<40^o$, (b) the sideway region, $40^o<\theta<150^o$, and (c) the rear stagnation point region, $150^o<\theta<180^o$. Uniform suction or blowing is applied on these three regimes, as illustrated in Fig. 32. The suction/blowing velocity is specified on the cylinder boundary, i.e., on the circle, and the direction of velocity vectors is radial. The overall flow configuration is perfectly symmetric with respect to the domain centerline. In Fig. 32a suction/blowing is applied on the front stagnation point region, in Fig. 32b on the sideway region, and in Fig. 32c on the rear stagnation point region. Here, simulations are performed for a representative value of Reynolds number, Re=90.

Following relative literature studies (Delaunay and Kaiktsis, 2001), we define a suction flow rate, Q_{suc}, a reference flow rate, Q_{ref}, and the suction coefficient, C_{suc}, as follows:

$$Q_{suc} = -\int_{-\pi}^{\pi} u(\theta) R d\theta \tag{36}$$

$$Q_{ref} = U_{inf} D \tag{37}$$

$$C_{suc} = \frac{Q_{suc}}{Q_{ref}} \tag{38}$$

where R is the cylinder radius. A positive suction coefficient corresponds to suction, whereas a negative suction coefficient corresponds to blowing.

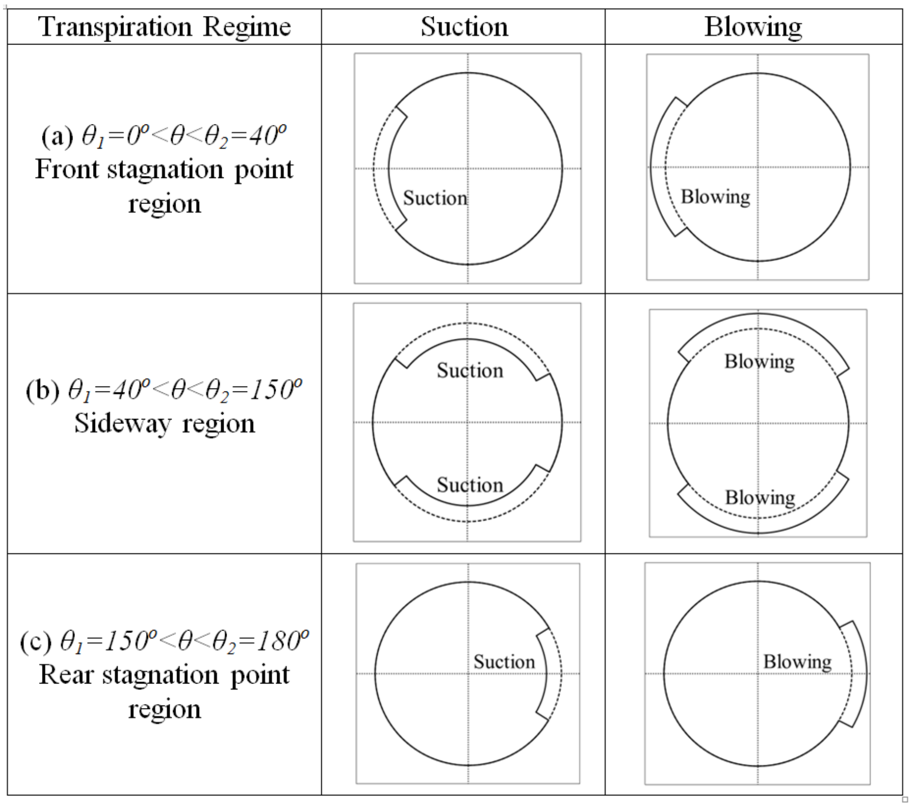
Transpiration Regime
Suction
Blowing
(a) θ1=0°<θ<θ2=40°
Front stagnation point region
Suction
Blowing
(b) θ1=40°<θ<θ2=150°
Sideway region
Suction
Suction
Blowing
Blowing
(c) θ1=150°<θ<θ2=180°
Rear stagnation point region
Suction
Blowing

Fig. 32. Sketch of uniform suction and blowing profiles applied on different regions of the cylinder surface: (a) front stagnation point region, $\theta_1=0^o<\theta<\theta_2=40^o$, (b) sideway region, $\theta_1=40^o<\theta<\theta_2=150^o$, and (c) rear stagnation point region, $\theta_1=150^o<\theta<\theta_2=180^o$.

4.1.1 Application of suction and blowing on the front stagnation point region, $0^o<\theta<40^o$

When uniform symmetric suction or blowing is applied on the front stagnation point region (Fig. 32a), extending (in the upper half plane) between $\theta_1=0^o$ and $\theta_2=40^o$, the suction coefficient, C_{suc}, and the normalized suction/blowing velocity, U_1/U_{inf}, become:

$$\begin{aligned} Q_{suc} &= -2\int_{\theta_1}^{\theta_2} U_1 R d\theta = -0.698 \cdot U_1 \cdot D \\ C_{suc} &= \frac{Q_{suc}}{Q_{ref}} = \frac{-0.698 \cdot U_1}{U_{inf}} \\ \frac{U_1}{U_{inf}} &= -1.433 \cdot C_{suc} \end{aligned} \tag{39}$$

Here, both the non-linear flow state and the base flow are computed, and results are presented subsequently.

4.1.1.1 Non-linear flow state

Here, the results of non-linear flow state calculations, when suction/blowing is applied on the front stagnation point region, are presented. Fig. 33 presents important flow statistics, computed by averaging over a number of shedding cycles. As illustrated in Fig. 33a, the shedding frequency decreases at increasing blowing flow rate, whereas it exhibits a mild increase at increasing suction. Fig. 33b shows that the time-averaged drag decreases at increasing blowing, while characterized by a mild increase for small to moderate suction flow rates; the trends are consistent with the suppression and enhancement of pressure stresses in the front stagnation point region caused by blowing and suction, respectively. Fig. 33c and Fig. 33d, presenting the dependence of lift and drag coefficient oscillation amplitude on suction coefficient, demonstrate in both cases an increase of force amplitude with blowing and a decrease with suction. Thus, these trends show that implementing blowing on the front stagnation point region destabilizes the flow, whereas implementing suction has a stabilizing effect. These effects on the force statistics are consistent with the intensity of instantaneous vorticity distributions, presented in Fig. 34.

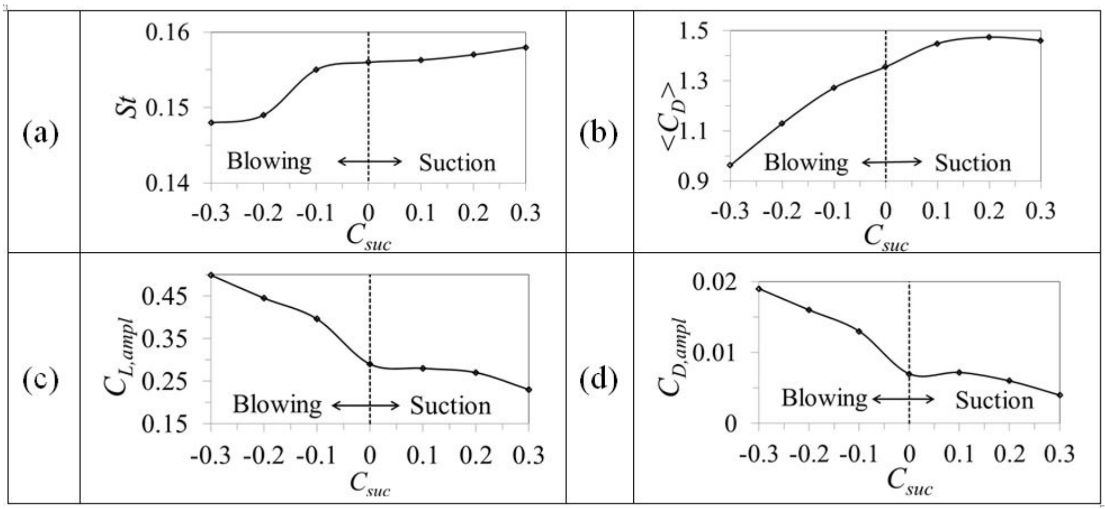

Fig. 33. *Re*=90: flow statistics versus suction coefficient, for suction/blowing applied on the front stagnation point region: (a) Strouhal number, *St*, (b) time-averaged drag coefficient, $<C_D>$, (c) amplitude of lift coefficient, $C_{L,ampl}$, and (d) amplitude of drag coefficient, $C_{D,ampl}$.

Control Action	C_{suc}	Vorticity Isocontours
Blowing	-0.3	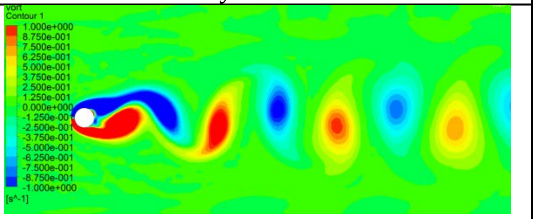
	-0.2	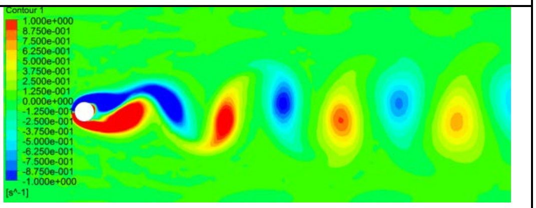
	-0.1	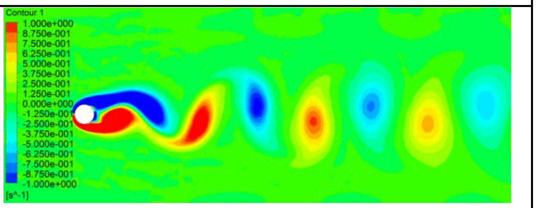
----	0	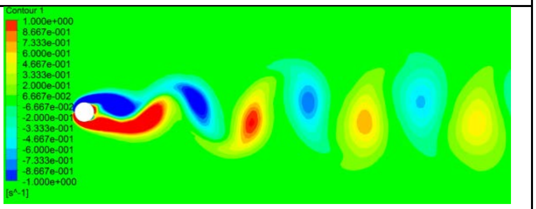
Suction	0.1	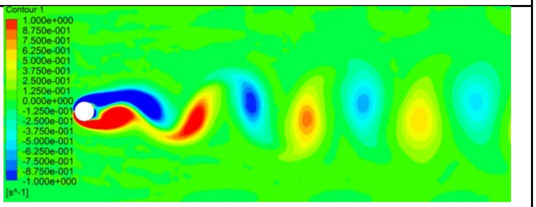
	0.2	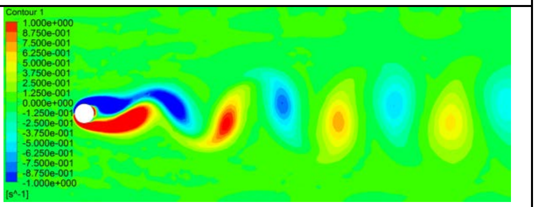
	0.3	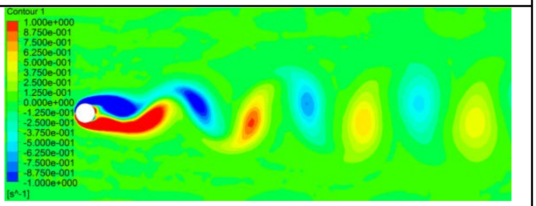

Fig. 34. *Re*=90: colour-coded contours of instantaneous vorticity, for different values of suction coefficient, C_{suc}, for suction/blowing applied on the front stagnation point region. (Negative values of C_{suc} correspond to blowing, and positive values to suction.)

4.1.1.2 Base flow

Here, results of base flow calculations are presented, in terms of important quantities characterizing the flow. The separation point angle, θ_s, is found to be an increasing function of C_{suc} (Fig. 35), indicating that the wake becomes thinner with the increase of suction, and thicker with the increase of blowing. This is in accordance with the tendency of decreasing velocity ratio, *R*, with suction, and the corresponding increasing tendency with blowing (Fig. 36). It is noted that a decreased region of positive velocity ratios (recirculation zone) results at increased suction, and the trend is reversed at increased blowing (Fig. 36). The narrower wakes corresponding to increased suction are associated with decreased levels of vorticity thickness, while the wakes corresponding to increased blowing exhibit higher vorticity thickness.

Further, the local instability properties are characterized, by associating the wake parameters with the results reported in Monkewitz and Nguyen (1987); in their work, wake profiles have been parametrized in terms of two parameters, *R*, *N*, where *N* is a profile parameter, associated with the vorticity thickness (steep profiles are characterized by high values of *N*). For a wide range of profiles corresponding to combinations of *R*, *N*, Monkewitz and Nguyen (1987) have characterized the profile instability as absolute or convective. In the present study, streamwise velocity profiles are extracted from the computed base flow fields, and are curve-fitted with the two-parameter (*R*, *N*) equation introduced by Monkewitz and Nguyen (1987). Here, to characterize the profile stability, the *R*, *N* pairs (points) are placed on the *R-1/N* plane, in which the convectively and absolutely unstable regios are identified; results are presented in Fig. 38, for data corresponding to the flow regime between x/D=0.5 (rear stagnation point) and x/D=8. The present results demonstrate that an increase in suction results in a decrease of the absolutely unstable area (Fig. 38a), whereas an increase in blowing results in a more pronounced increase of absolute instability (Fig. 38b). These observations verify the trends of suction/blowing implemented on the front stagnation point region as identified by the non-linear flow calculations.

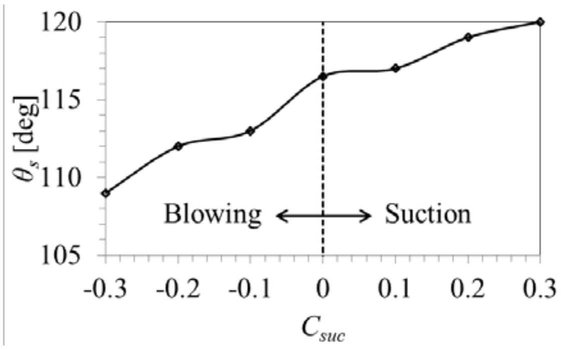

Fig. 35. *Re*=90, suction/blowing applied from θ_1=0° to θ_2=40°: base flow separation point angle, θ_s, vs. suction coefficient, C_{suc}.

Control Action	(a) Suction	(b) Blowing
Velocity Ratio, *R*	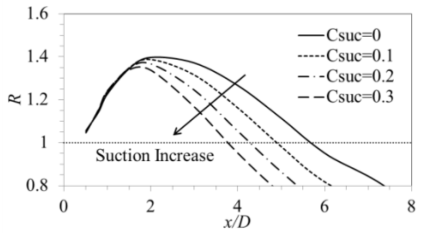	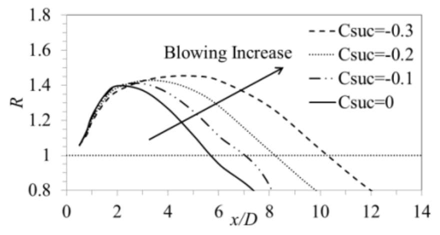

Fig. 36. Re=90, suction/blowing applied from θ_1=0° to θ_2=40°: base flow velocity ratio, R, vs. streamwise coordinate, for different values of suction coefficient, C_{suc}, for (a) suction, and (b) blowing.

Control Action	(a) Suction	(b) Blowing
Vorticity Thickness δ_w/D	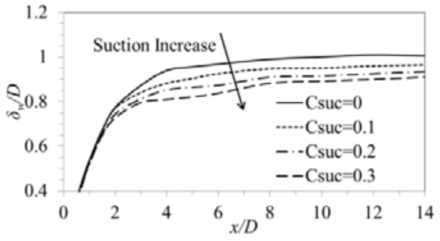	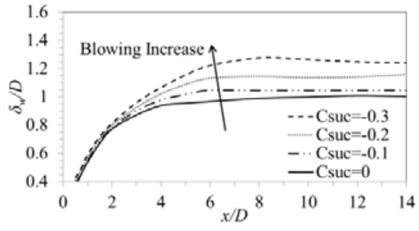

Fig. 37. Re=90, suction/blowing applied from θ_1=0° to θ_2=40°: base flow vorticity thickness, δ_w/D, vs. streamwise coordinate, for different values of suction coefficient, C_{suc}, for (a) suction, and (b) blowing.

Control Action	(a) Suction	(b) Blowing
R vs. *1/N*	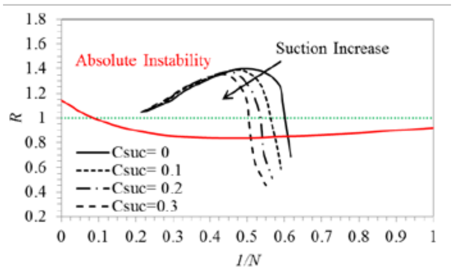	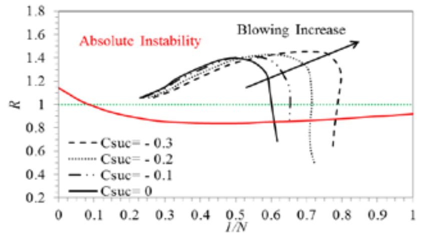

Fig. 38. Re=90, suction/blowing applied from θ_1=0° to θ_2=40°: base flow velocity ratio, R, vs. profile parameter 1/N, for different values of suction coefficient, C_{suc}, for (a) suction, and (b) blowing. Absolute instability boundary is illustrated by the red line (Monkewitz and Nguyen, 1987).

4.1.2 Application of suction and blowing on the sideway region, $40^o<\theta<150^o$

When symmetric uniform suction or blowing is applied on the sideway region (Fig. 32b), extending in the upper half plane between θ_1=40^o and θ_2=150^o, the suction coefficient, C_{suc}, and the non-dimensional suction/blowing velocity, U_2/U_{inf}, become:

$$Q_{suc} = -2\int_{\theta_1}^{\theta_2} U_2 R d\theta = -1.919 \cdot U_2 \cdot D$$
$$C_{suc} = \frac{Q_{suc}}{Q_{ref}} = \frac{-1.919 \cdot U_2}{U_{\inf}} \tag{40}$$
$$\frac{U_2}{U_{\inf}} = -0.521 \cdot C_{suc}$$

4.1.2.1 Non-linear flow state calculations

Here, non-linear flow state calculations are presented for the case where suction/blowing is applied on the sideway region. Important flow statistics are presented in Fig. 39. As illustrated in Fig. 39a, the Strouhal number is an increasing function of suction coefficient, i.e. it decreases at increased blowing and increases with suction. Fig. 39c and Fig. 39d demonstrate that force fluctuations increase with blowing and decrease with suction, while they vanish for C_{suc}=0.3 (full cancellation of the vortex street). These trends are the same with those obtained for transpiration in the front stagnation point region (Fig. 33c and Fig. 33d). The effects of transpiration on force statistics are consistent with the intensity of instantaneous vorticity distributions presented in Fig. 40. Finally, Fig. 39b shows a monotonic decrease of time-averaged drag with suction coefficient.

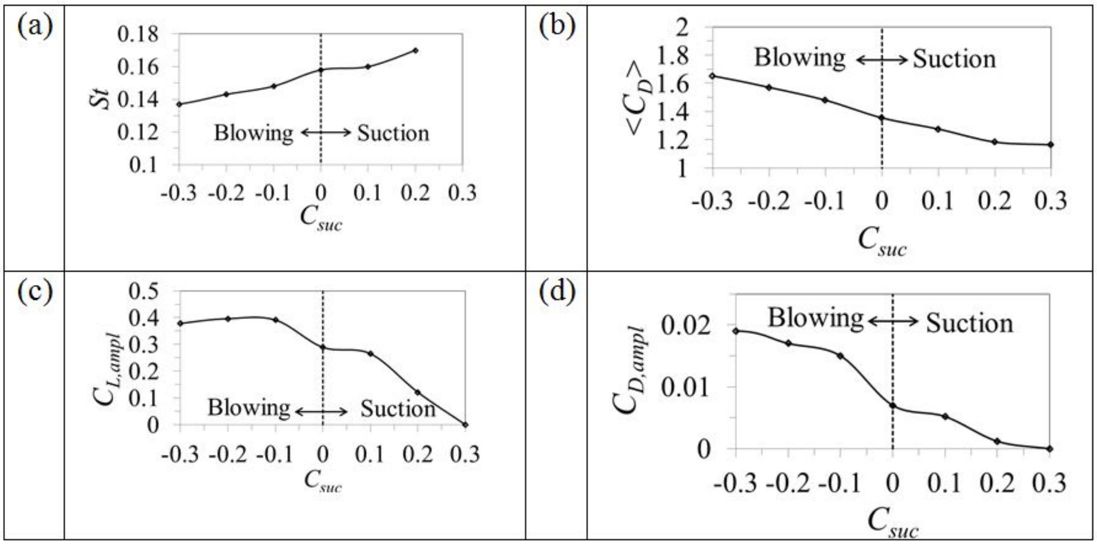

Fig. 39. *Re*=90: flow statistics versus suction coefficient, for suction/blowing applied on the cylinder sideway region: (a) Strouhal number, *St*, (b) time-averaged drag coefficient, $<C_D>$, (c) amplitude of lift coefficient, $C_{L,ampl}$, and (d) amplitude of drag coefficient, $C_{D,ampl}$.

Control Action	C_{suc}	Vorticity Isocontours
Blowing	-0.3	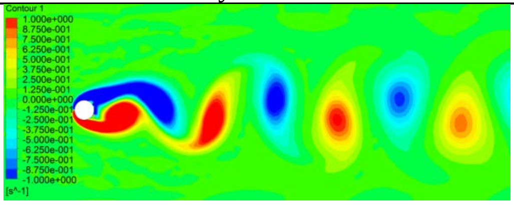
	-0.2	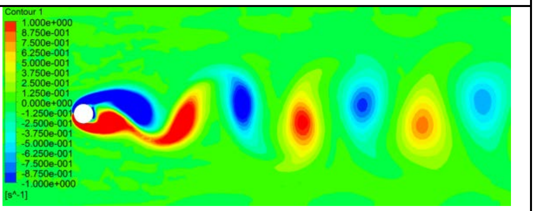
	-0.1	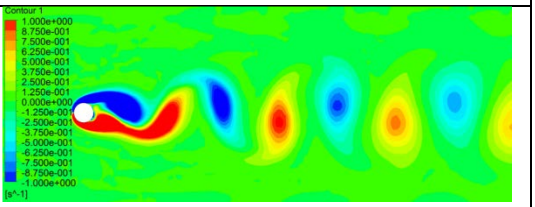
----	0	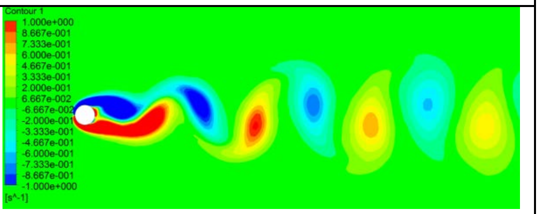
Suction	0.1	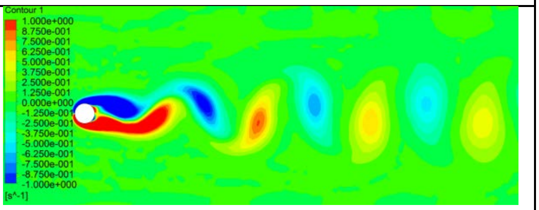
	0.2	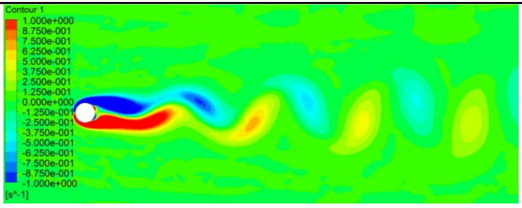
	0.3	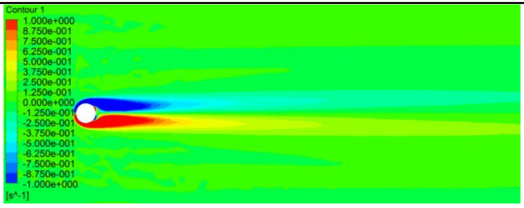

Fig. 40. Re=90: colour-coded contours of instantaneous vorticity, for different values of suction coefficient, C_{suc}, for suction/blowing applied on the cylinder sideway region. (Negative values of C_{suc} correspond to blowing, and positive values to suction.)

4.1.2.2 Base flow calculations

Here, base flow calculations are performed for the case of suction/blowing application on the sideway region. The present results show that the separation point angle, θ_s, (Fig. 41) is increasing with the increase of both suction and blowing flow rate. When suction is increased, both the velocity ratio, *R*, (Fig. 42a) and the vorticity thickness, δ_w/D, (Fig. 43a) are decreased, resulting overall in the formation of a narrower wake, and thus in the stabilization of the global flow. It is worth noting, that, at C_{suc}=0.3, the extent of the area where *R*>1 (equivalently: the extent of the recirculation regions) is substantially reduced. This observation is in agreement with the corresponding calculations of non-linear flow; the latter demonstrate that the vortex street is fully supressed at C_{suc}=0.3. On the other hand, when blowing is increased, both the the velocity ratio, *R*, (Fig. 42b) and the vorticity thickness, δ_w, (Fig. 43b) increase, resulting overall in the formation of a longer and thicker wake; this further destabilizes the flow.

Furthermore, curve-fitting of the streamwise velocity profiles extracted from the base flow field with the two-parameter (*R*, *N*) profile equation of Monkewitz and Nguyen (1987), and placement of the solutions on the *R-1/N* plot (Fig. 44) demonstrates that an increase in suction in the sideway region results in a significant decrease of the extent of the absolutely unstable region, whereas an increase in blowing results in a substantial increase of the extent of absolute instability. These results verify the strong stabilizing effects of suction, as well as the strong destabilizing effects of blowing.

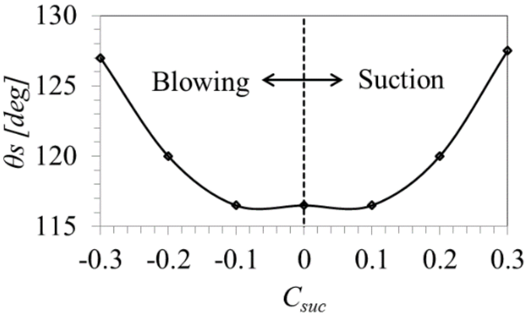

Fig. 41. *Re*=90, with suction/blowing applied from θ_1=40° to θ_2=150°: base flow separation point angle, θ_s, vs. suction coefficient, C_{suc}.

<table>
<tr><th>Control Action</th><th>(a) Suction</th><th>(b) Blowing</th></tr>
<tr><td>Velocity Ratio, R</td><td>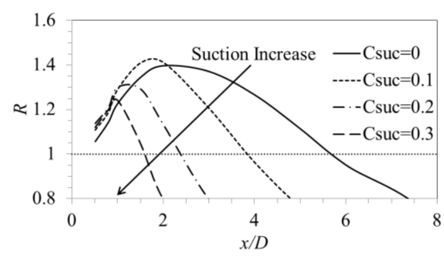
</td><td>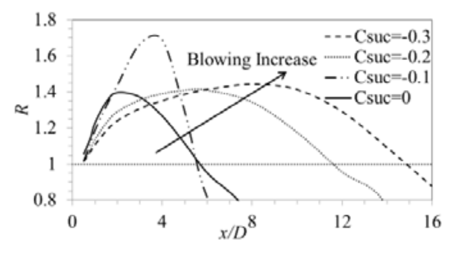
</td></tr>
</table>

Fig. 42. *Re*=90, suction/blowing is applied from θ_1=40° to θ_2=150°: base flow velocity ratio, *R*, vs. streamwise coordinate, for different values of suction coefficient, C_{suc}, for (a) suction, and (b) blowing.

Control Action	(a) Suction	(b) Blowing
Vorticity Thickness, δ_w/D	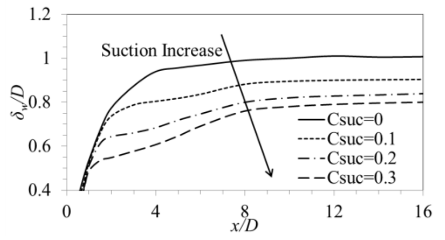	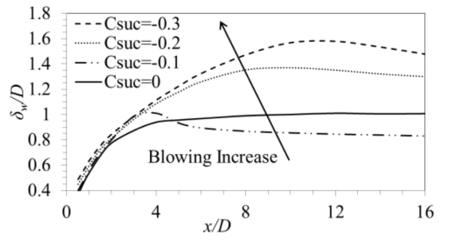

Fig. 43. *Re*=90: suction/blowing applied from θ_1=40° to θ_2=150°: base flow vorticity thickness, δ_w/D, vs. streamwise coordinate, for different values of suction coefficient, C_{suc}, for (a) suction, and (b) blowing.

Control Action	(a) Suction	(b) Blowing
Velocity Ratio vs. *1/N*	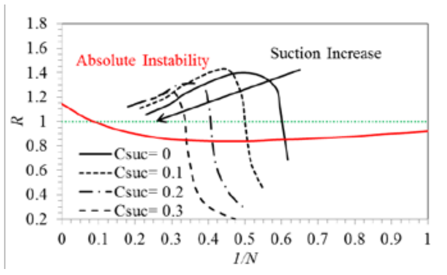	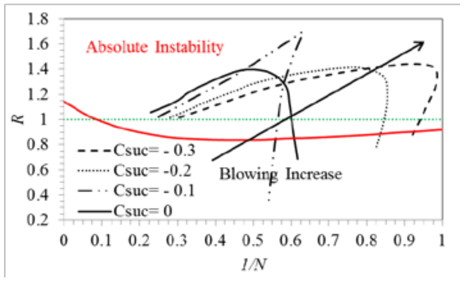

Fig. 44. *Re*=90: suction/blowing is applied from θ_1=40° to θ_2=150°: base flow velocity ratio, *R*, vs. profile parameter 1/*N*, for different values of suction coefficient, C_{suc}, for (a) suction, and (b) blowing. Absolute instability boundary is illustrated by the red line (Monkewitz and Nguyen, 1987).

4.1.3 Application of suction and blowing on the rear stagnation point region, 150°<θ<180°

When symmetric uniform suction or blowing is applied on the rear stagnation point region, extending in the upper half plane between θ_1=150° and θ_2=180°, the suction coefficient, C_{suc}, and the non-dimensional suction/blowing velocity, U_3/U_{inf}, become:

$$\begin{aligned} Q_{suc} &= -2\int_{\theta_1}^{\theta_2} U_3 R d\theta = -0.523\cdot U_3\cdot D \\ C_{suc} &= \frac{Q_{suc}}{Q_{ref}}\frac{-0.523\cdot U_3}{U_{\inf}} \\ \frac{U_3}{U_{\inf}} &= -1.909\cdot C_{suc} \end{aligned} \tag{41}$$

4.1.3.1 Non-linear flow state calculations

Here, non-linear flow state calculations are performed for the case of suction/blowing application in the rear stagnation point region, and the corresponding results are presented and analyzed. In Fig. 32c, a sketch of the suction and blowing profiles in the rear stagnation point regime is presented. Important flow statistics, computed by averaging over a number of shedding cycles, are presented in Fig. 45. As illustrated in Fig. 45a, the shedding frequency decreases at increasing blowing flow rate, until vortex street cancellation at $C_{suc} \approx -0.2$, whereas it exhibits a similar decrease at increasing suction, for approximately C_{suc}>0.06. Fig. 45b shows that the time-averaged drag is characterized by a mild decrease for small to moderate blowing flow rates, while it exhibits a substantial increase for suction. Fig. 45c and Fig. 45d, presenting the variation of lift and drag coefficient oscillation amplitude, demonstrate an enormous increase of force fluctuations with suction, while also showing the wake stabilization at a moderate blowing flow rate ($C_{suc} \approx -0.2$). Thus, these trends show that implementing suction on the rear stagnation point region destabilizes the non-linear flow, whereas implementing blowing has a strong stabilizing effect. These effects on the force statistics are in accordance with the intensity of instantaneous vorticity distributions, presented in Fig. 46.

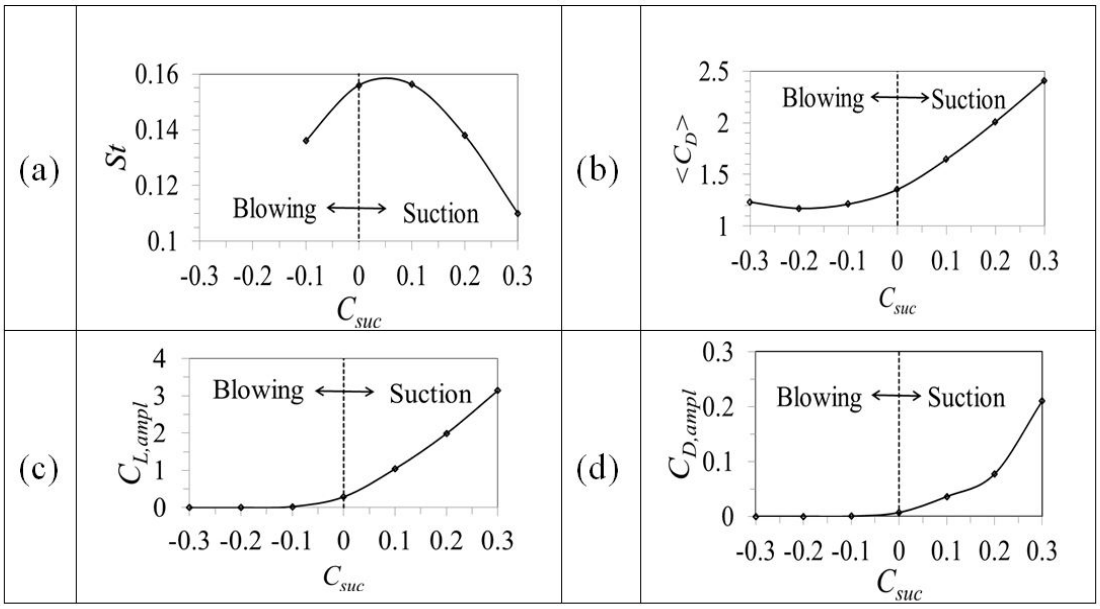

Fig. 45. *Re*=90: flow statistics versus suction coefficient, for suction/blowing applied on the rear stagnation point region: (a) Strouhal number, *St*, (b) time-averaged drag coefficient, $<C_D>$, (c) amplitude of lift coefficient, $C_{L,ampl}$, and (d) amplitude of drag coefficient, $C_{D,ampl}$.

Control Action	C_{suc}	Vorticity Isocontours
Blowing	-0.3	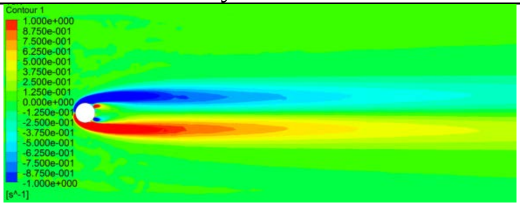
	-0.2	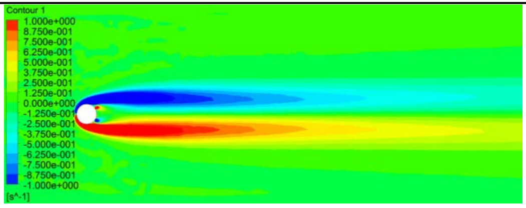
	-0.1	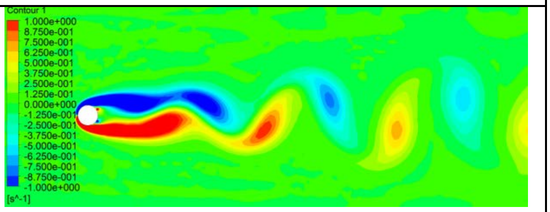
----	0	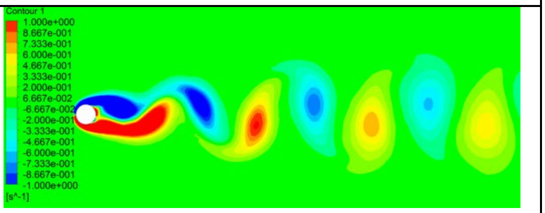
Suction	0.1	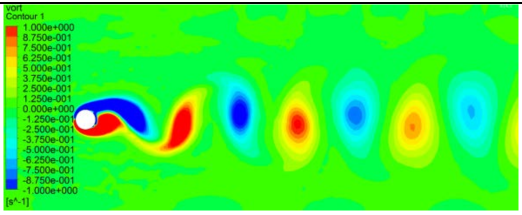
	0.2	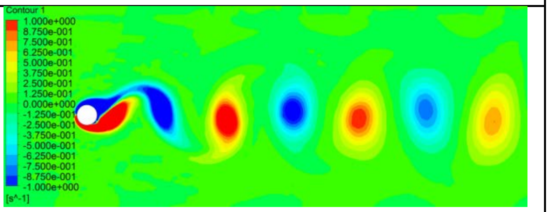
	0.3	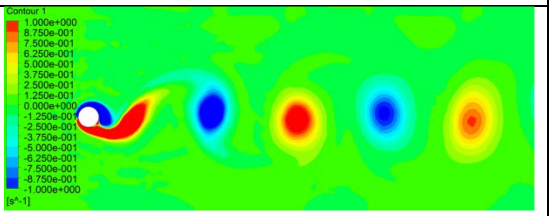

Fig. 46. *Re*=90: colour-coded contours of instantaneous vorticity, for different values of suction coefficient, C_{suc}, for suction/blowing applied on the rear stagnation point region. (Negative values of C_{suc} correspond to blowing, and positive values to suction.)

4.1.3.2 Base flow calculations

Here, base flow calculations are performed for the case of implementing suction/blowing on the rear stagnation point region. It is found that the separation point angle, θ_s, (Fig. 47) remains practically constant when blowing is increased, while it is a mildly increasing function of C_{suc}. When suction is increased, the extent of the area characterized by velocity ratio R>1 (recirculation zones) is reduced, whereas the magnitudes of negative velocities are significantly increased (Fig. 48a). The decreased region of backflow corresponds to a stabilizing effect. Nonetheless, the higher levels of negative velocities correspond to stronger absolute instability, which, as shown by the non-linear calculations reported above, overcome the stabilizing effects. On the other hand, as blowing is increased (Fig. 48b), the recirculation zones initially tend to be pushed downstream and reduce in size (C_{suc} = -0.1), while they disappear at higher blowing flow rates (C_{suc} = -0.2, -0.3); as illustrated by the non-linear flow calculations, the latter results in stabilization of the global flow. The variation in vorticity thickness, presented in Fig. 49, shows that it decreases with suction (Fig. 49a), and increases with blowing (Fig. 49b). However, the corresponding range in the profile parameter 1/N is such that the change in vorticity thickness is not expected to affect the stability properties of these profiles (Fig. 50). The results presented in Fig. 50 demonstrate that an increase in suction increases the intensity of absolute instability in the near wake while also reducing the extent of the absolutely unstable region (Fig. 50a). On the other hand, an increase in blowing decreases both the intensity and the spatial extent of absolute instability (Fig. 50b); no local absolute instability is present in the wake of base flow for $C_{suc} \leq -0.3$. It is undelined that the effects of implementing suction/blowing in the rear stagnation point region are opposite to those associate with implementing mass transpiration in the sideway region, reported in section 4.1.2.

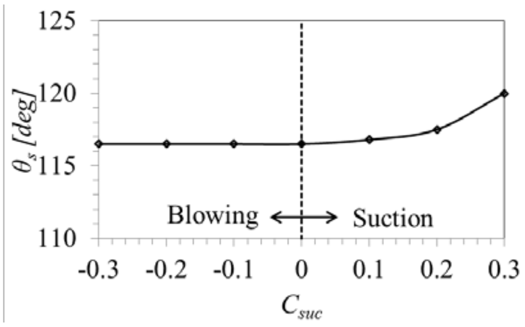

Fig. 47. Re=90, suction/blowing applied from θ_1=150° to θ_2=180°: base flow separation point angle, θ_s, vs. suction coefficient, C_{suc}.

Control Action	(a) Suction	(b) Blowing
Velocity Ratio, R	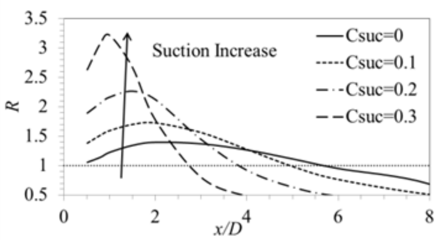	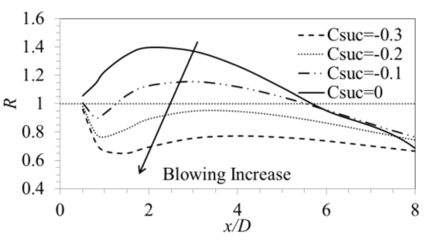

Fig. 48. Re=90: suction/blowing applied from θ_1=150° to θ_2=180°: base flow velocity ratio, R, vs. streamwise coordinate, for different values of suction coefficient, C_{suc}, for (a) suction, and (b) blowing.

<table>
<tr><th>Control Action</th><th>(a) Suction</th><th>(b) Blowing</th></tr>
<tr><td>Vorticity Thickness, δ_w/D</td><td>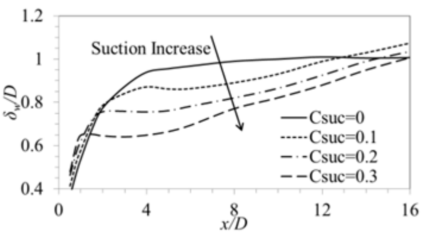
</td><td>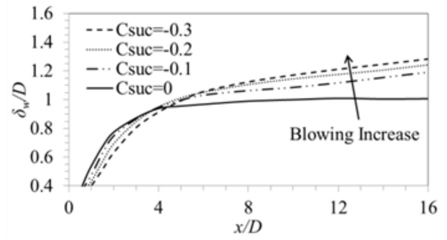
</td></tr>
</table>

Fig. 49. Re=90, suction/blowing applied from θ_1=150° to θ_2=180°: base flow vorticity thickness, δ_w/D, vs. streamwise coordinate, for several values of suction coefficient, C_{suc}, for (a) suction, and (b) blowing.

<table>
<tr><th>Control Action</th><th>(a) Suction</th><th>(b) Blowing</th></tr>
<tr><td>Velocity Ratio vs. $1/N$</td><td>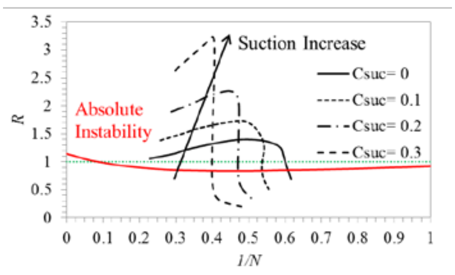
</td><td>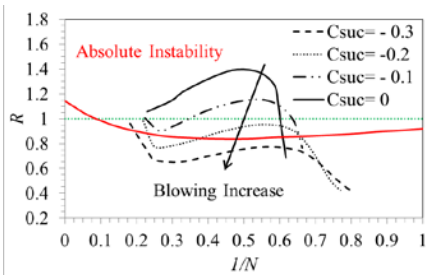
</td></tr>
</table>

Fig. 50. Re=90, suction/blowing applied from θ_1=150° to θ_2=180°: base flow velocity ratio R, vs. profile parameter $1/N$, for different values of suction coefficient, C_{suc}, for (a) suction, and (b) blowing. Absolute instability boundary is illustrated by the red line (Monkewitz and Nguyen, 1987).

4.1.4 Overall evaluation of results for piecewise uniform suction/blowing

In the previous sections, the effects of implementing mass transpiration on different regions of the cylinder surface on the flow dynamics and global stability have been assessed. It was demonstrated that: (a) application of suction on the front stagnation point region has a mild stabilizing effect, (b) application of suction on the sideway region has a strong stabilizing effect, and (c) application of blowing on the rear stagnation point region has a strong stabilizing effect. An effective control scheme may thus result from the combination of suction on the sideway region, as well as on the front stagnation point region, and blowing on the rear stagnation point region. Further, from the point of view of an actual implementation, it is attractive if mass transpiration is characterized by a zero net flow rate, and thus no net pumping requirements. Thus, a passive control scheme is developed next, aiming at the optimal (partial or full) cancellation of the vortex street, at a net mass flow rate of zero.

4.2 Formulation of optimization problem with piecewise uniform suction/blowing profile

The goal in the present section is to determine optimal piecewise uniform suction/blowing profiles which suppress (partially or fully) the von Kármán vortex street at a minimal control effort. Here, the term optimal is associated with the minimization of properly defined objective functions. To this end, a two-objective optimization problem is formulated; the first objective function is associated with the flow global stability, while the second one quantifies the control effort, in a way related to the mass flow rate of suction/blowing.

The suction/blowing profile is defined parametrically, so as to correspond to a zero total net transpiration flow rate. The investigation presented in the previous section has indicated that stabilizing effects are induced by applying: (a) suction on the sideway region and on the front stagnation point region, and (b) blowing on the rear stagnation point region. For an optimal overall effect, a combination of the three control measures is implemented here, in order to suppress flow unsteadiness at a minimal control effort. In view of an actual implementation without net pumping requirements, the total suction flow rate equals the total blowing flow rate. Thus, for Q_1 and Q_2 being the (suction) flow rates in the front stagnation point region and in the sideway region, respectively, and Q_3 the (blowing) flow rate in the rear stagnation point region: $Q_1+Q_2=Q_3$. Consequently, in the present setup, a suction coefficient can be defined as follows:

$$C_{suc} = \frac{Q_1 + Q_2}{Q_{ref}} = \frac{Q_3}{Q_{ref}} \tag{42}$$

By denoting with θ_1 and θ_2 the angles delimiting the sideway region (in the upper half plane), U_1 and U_2 the suction velocities in the front stagnation point region and in the sideway region, respectively, and U_3 the blowing velocity in the rear stagnation point region, the suction/blowing flow rates are readily calculated as follows:

$$Q_{suc} = Q_1 + Q_2 = 2\int_0^{\theta_1} U_1 R d\theta + 2\int_{\theta_1}^{\theta_2} U_2 R d\theta \tag{43}$$

yielding:

$$\begin{aligned} Q_{suc} &= \left(\theta_1 U_1 + (\theta_2 - \theta_1) U_2\right) D \\ Q_{blow} &= Q_3 = 2\int_{\theta_2}^{\pi} U_3 R d\theta = (\pi - \theta_2) U_3 D \end{aligned} \tag{44}$$

The constraint of zero net transpiration flow rate dictates a given relation between the flow rates Q_1, Q_2, or, equivalently, between the suction velocities U_1, U_2:

$$U_1 = c \cdot U_2 \tag{45}$$

where c is a proper constant. Determination of the constant c should account for the finding, reported above, that suction on the front stagnation point region should be milder than suction on the sideway region.

Thus, a piecewise uniform transpiration velocity profile, as the one illustrated in Fig. 51, can be fully defined in terms of four parameters: C_{suc}, θ_1, θ_2, c.

$$
\begin{aligned}
\frac{U_1}{U_{\inf}} &= \frac{c \cdot C_{suc}}{\left(\theta_1 \cdot (c-1) + \theta_2\right)} \\
\frac{U_2}{U_{\inf}} &= \frac{C_{suc}}{\left(\theta_1 \cdot (c-1) + \theta_2\right)} \\
\frac{U_3}{U_{\inf}} &= \frac{C_{suc}}{\left(\pi - \theta_2\right)}
\end{aligned}
\tag{46}
$$

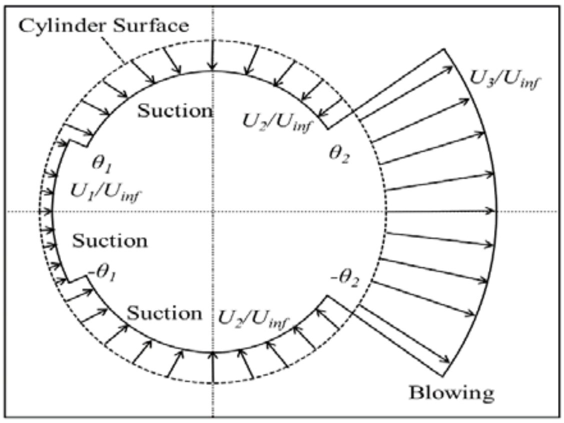

Fig. 51. Sketch of transpiration velocity profile.

4.2.1 Design variables and search space

As the transpiration velocity profile is symmetric with respect to the domain centerline (y=0), it is sufficient if it is defined in the upper x-y plane. Here, the transpiration profile is defined in terms of a piecewise constant parametric function, whose parameters form the design variables for optimization:

$$
\frac{U(\theta)}{U_{\inf}} = \begin{cases} \dfrac{U_1}{U_{\inf}} = \dfrac{c \cdot C_{suc}}{\left(\theta_1 \cdot (c-1) + \theta_2\right)}, & 0^o < \theta < \theta_1 \\ \dfrac{U_2}{U_{\inf}} = \dfrac{C_{suc}}{\left(\theta_1 \cdot (c-1) + \theta_2\right)}, & \theta_1 < \theta < \theta_2 \\ \dfrac{U_3}{U_{\inf}} = \dfrac{C_{suc}}{\left(\pi - \theta_2\right)}, & \theta_2 < \theta < \pi \end{cases}
\tag{47}
$$

Thus, the transpiration velocity profile is defined parametrically in terms of four design variables, namely, the suction coefficient, C_{suc}, the angles delimiting the sideway region, θ_1, θ_2 (expressed in radians), and the constant c. It should be noted that θ_2 is the angle defining the boundary between the suction and the blowing region. In the present implementation, wide limits have been considered for the corresponding search space:

$$
\begin{aligned}
& 0 < C_{suc} < 0.5 \\
& 0^o < \theta_1 < 40^o \\
& 140^o < \theta_2 < 165^o \\
& 0 < c < 0.5
\end{aligned}
\tag{48}
$$

Regarding the selection of the search space of θ_2, it is noted that, to avoid a destabilizing effect due to blowing, its lower limit has been set higher than the corresponding separation angle of the uncontrolled base flow (117^o for Re=90, according to our simulation results).

4.2.2 Objective functions

Two objective functions are considered.

(a) First objective function:

The first objective function, J_1, related to the flow global stability, is the same one introduced in the optimization problem studied in Chapter 3 (see eqs. 32, 33, 34).

(b) Second objective function:

The suction coefficient, C_{suc} (see eq. 38), quantifying the total control effort, is the second objective function.

4.2.3 Optimization process

The present work aims at arriving at states of controlled flow which correspond to partially or fully suppressed vortex streets, at a minimal control effort. To this end, a two-objective minimization problem is formulated, aiming at a simultaneous minimization of proper measures of flow instability and control effort (here: J_1 and C_{suc}, respectively). Thus, the goal of optimization is to find optimum combinations of the design variables (C_{suc}, θ_1, θ_2, c), which define transpiration profiles that simultaneously minimize objective functions J_1 and C_{suc}. It is noted that here C_{suc} is used both as design variable and objective function.

The final set of optimal solutions for the two-objective minimization problem of the present study is obtained by evolving an initial generation of 20 individuals. Here, the same genetic algorithm utilized in the optimization problem considered in Chapter 3 was used. All generations consisted of 20 individuals; a total 15 generations has been utilized, and convergence to the final Pareto verified. The procedure is sketched in Fig. 52. An individual CFD run has required approximately 2.5 hours of turnaround time on 24 cores of a parallel cluster.

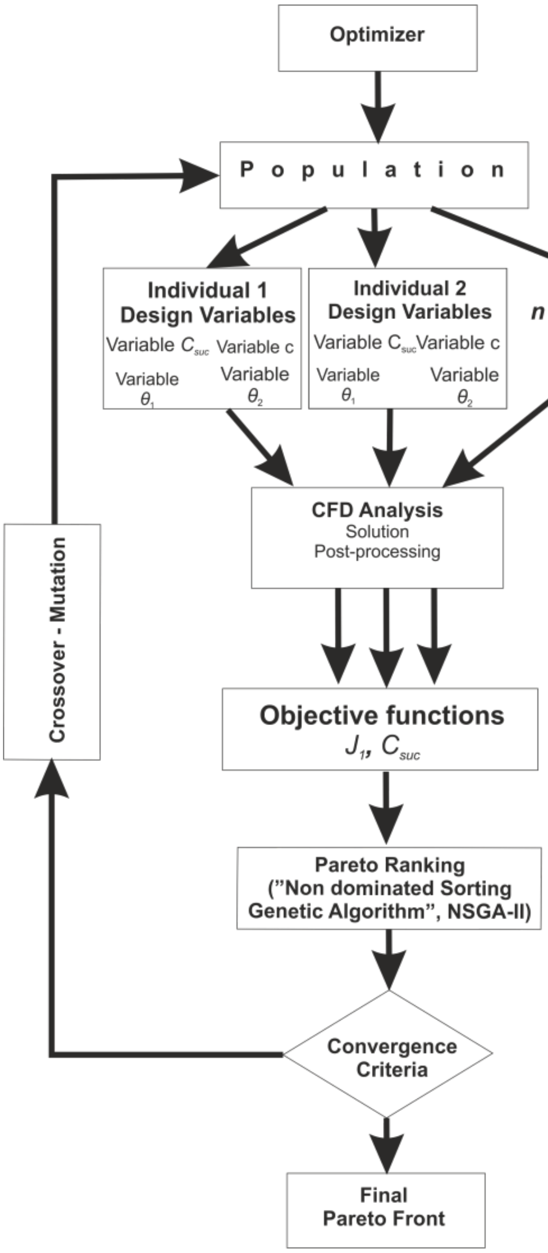
Optimizer
Population
Individual 1 Design Variables
Variable C_{suc} Variable c
Variable θ_1 Variable θ_2
Individual 2 Design Variables
Variable C_{suc} Variable c
Variable θ_1 Variable θ_2
n individuals
CFD Analysis
Solution
Post-processing
Objective functions
J_1, C_{suc}
Pareto Ranking
("Non dominated Sorting Genetic Algorithm", NSGA-II)
Convergence Criteria
Final Pareto Front
Crossover - Mutation

Fig. 52. Optimization flow chart.

4.2.4 Optimization results

4.2.4.1 Optimization results for Re=90

The optimization results for *Re*=90 are presented in Fig. 53, in terms of the values of the problem objective functions, J_1, C_{suc}. Results corresponding to blowing in the rear stagnation point region, utilizing the problem setup of Delaunay and Kaiktsis (2001), have been also added in Fig. 53. Each combination of the problem design variables (C_{suc}, θ_1, θ_2, c) corresponds to a different transpiration profile, resulting in either unstable or stable flow (values of function J_1 positive or zero, respectively). Fig. 53 demonstrates that, in the set of optimal solutions, an increase in control effort results in a more stable flow (decrease of J_1).

Four representative solutions, as well as the case of uncontrolled flow, are highlighted in Fig. 53 with colored squares. The corresponding values of design variables and objective functions are reported in Table 7. For these representative solutions, Fig. 54 presents the distribution of suction/blowing velocity, as well as instantaneous vorticity isocontours, while Fig. 55 presents the computed signals of drag and lift coefficient. As illustrated in Fig. 55, at increasing control effort, the time-averaged drag coefficient decreases, whereas the drag and lift oscillation amplitudes decrease, becoming zero in the limit of global flow stabilization, due to the combined stabilizing effects of suction in the sideway and front stagnation point regions, and blowing in the rear stagnation point region. The variation of the three design variables, as a function of the suction coefficient, C_{suc}, along the Pareto front is presented in Fig. 56 (the red squares correspond to Point 4 of Fig. 53). The corresponding dependence of the transpiration velocities is presented in Fig. 57. Fig. 56b shows that at increasing control effort (C_{suc}) the extent of the blowing is reduced; from mass conservation, this corresponds to a more pronounced increase of the blowing velocity, U_3 (Fig. 57c).

Thus, the combination of suction in the sideway and front stagnation point regions and blowing in the rear stagnation point region enhances the individual stabilizing effects, resulting in global flow stabilization (solution depicted by Point 4 in Fig. 53); stabilization is attained at the low value of C_{suc} = 0.102. An important observation regarding solutions in the limit of global flow stabilization is that the blowing region has become rather narrow, which is associated with strong blowing, in a near wake which is thin due to sideway suction. Thus, the minimum control effort required for global flow stabilization using the present approach (C_{suc} = 0.102) is significantly lower than the corresponding one reported in Delaunay and Kaiktsis (2001) for the case of pure blowing ($|C_{suc}|$ = 0.145).

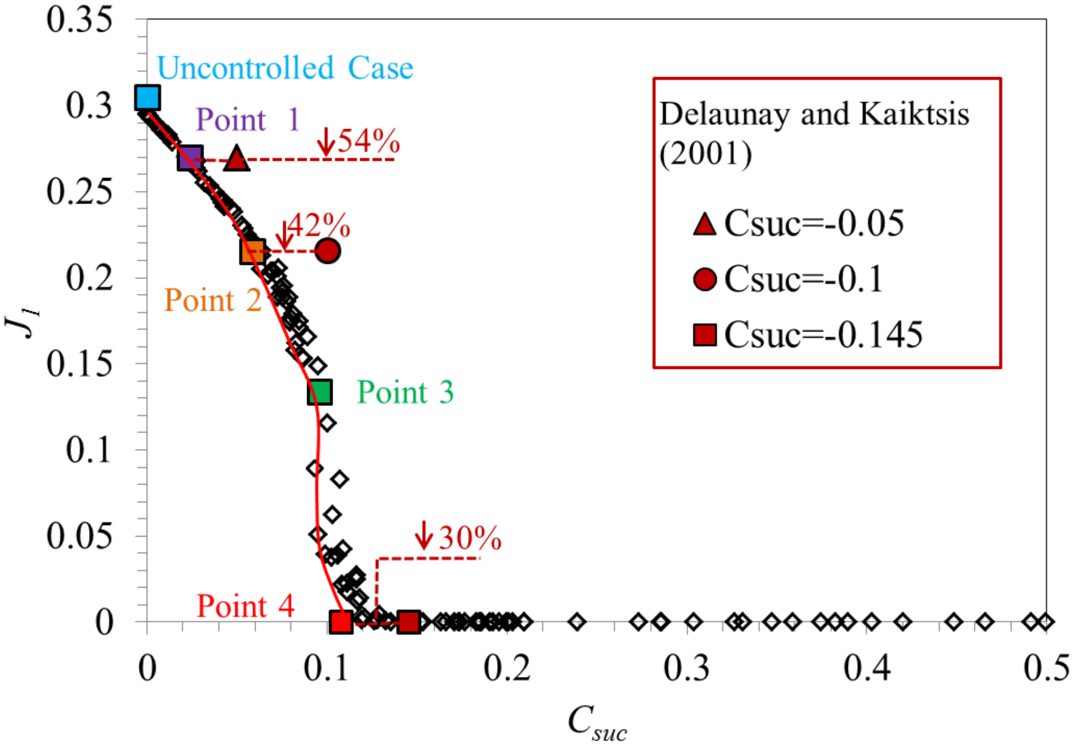

Fig. 53. *Re*=90: objective function J_1 vs. objective function C_{suc} (suction coefficient).

Table 7. Re = 90: design variable values and corresponding objective function values, for the uncontrolled case, as well as for solutions 1-4, depicted in Fig. 53.

Case	C_{suc}	θ_1	θ_2	c	J_1
Uncontrolled	-	-	-	-	0.319
Point 1	0.023	17.36^{o}	158.12^{o}	0.280	0.270
Point 2	0.058	29.59^{o}	149.93^{o}	0.200	0.220
Point 3	0.096	0.00^{o}	151.83^{o}	(0.428)	0.134
Point 4	0.102	11.57^{o}	163.87^{o}	0.380	0.000

Solutions	Transpiration Velocity Profile	Vorticity Isocontours
Uncontrolled Case	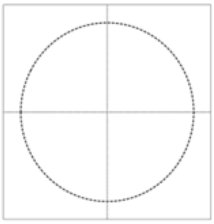	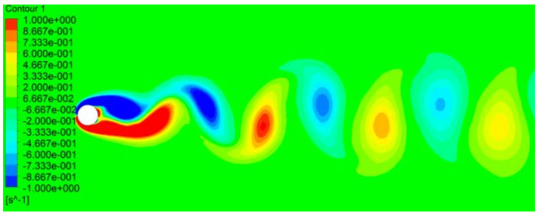
Point 1 C_{suc}=0.023	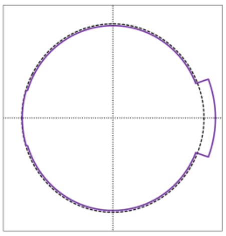	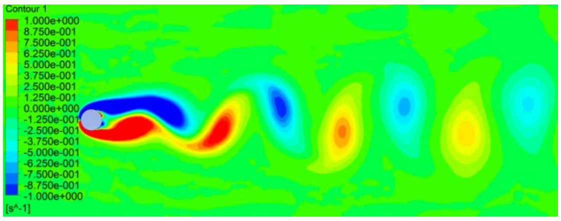
Point 2 C_{suc}=0.058	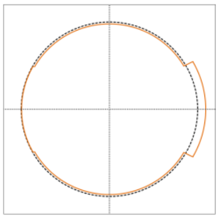	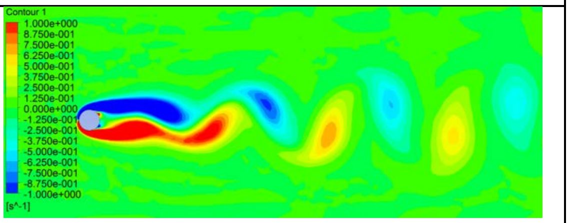
Point 3 C_{suc}=0.096	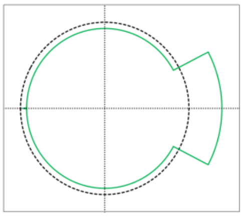	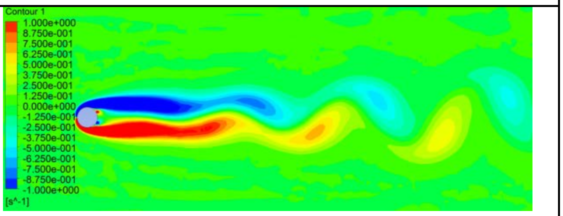
Point 4 C_{suc}=0.102	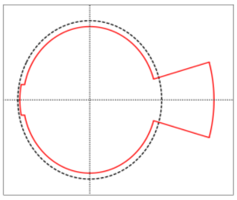	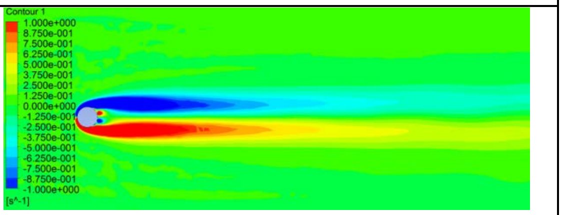

Fig. 54. Re=90: computed transpiration velocity profiles corresponding to solutions 1-4, depicted in Fig. 53 (left column), and corresponding color-coded contours of instantaneous vorticity (right column). The case of uncontrolled flow is also included.

Solutions	Drag Coefficient, C_D	Lift Coefficient, C_L
Uncontrolled Case	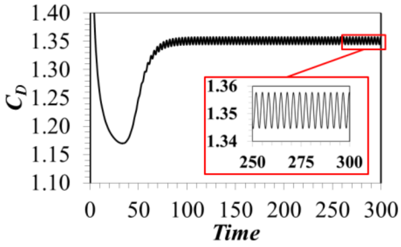	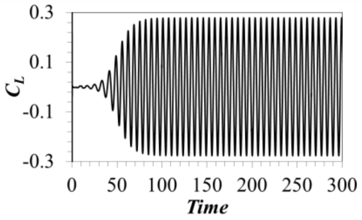
Point 1 C_{suc}=0.023	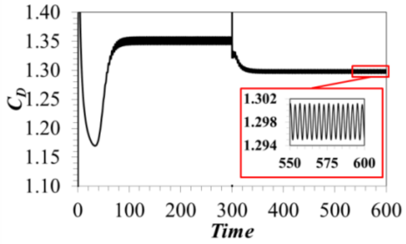	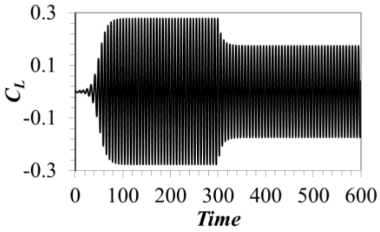
Point 2 C_{suc}=0.058	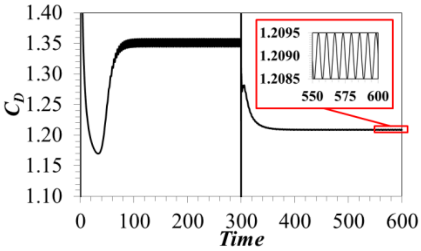	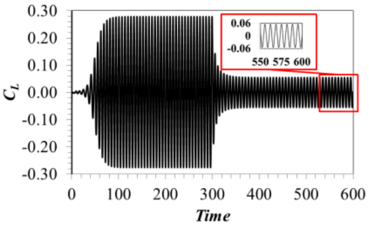
Point 3 C_{suc}=0.096	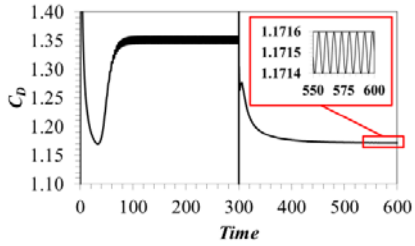	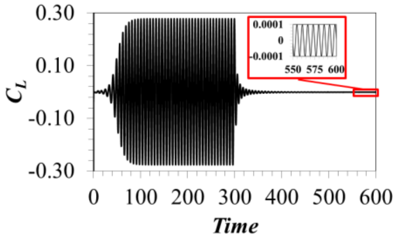
Point 4 C_{suc}=0.102	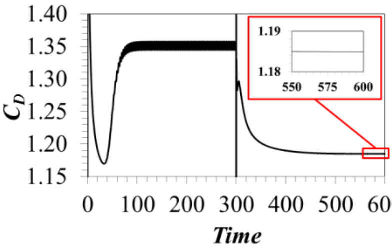	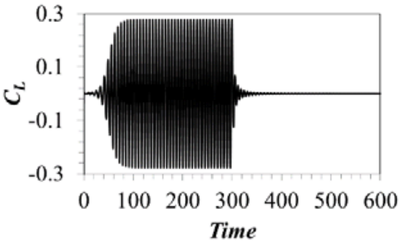

Fig. 55. *Re*=90: drag and lift coefficient signals for solutions 1-4, depicted in Fig. 53, and for the case of uncontrolled flow. Active open-loop control in terms of suction/blowing is implemented at *t*=300.

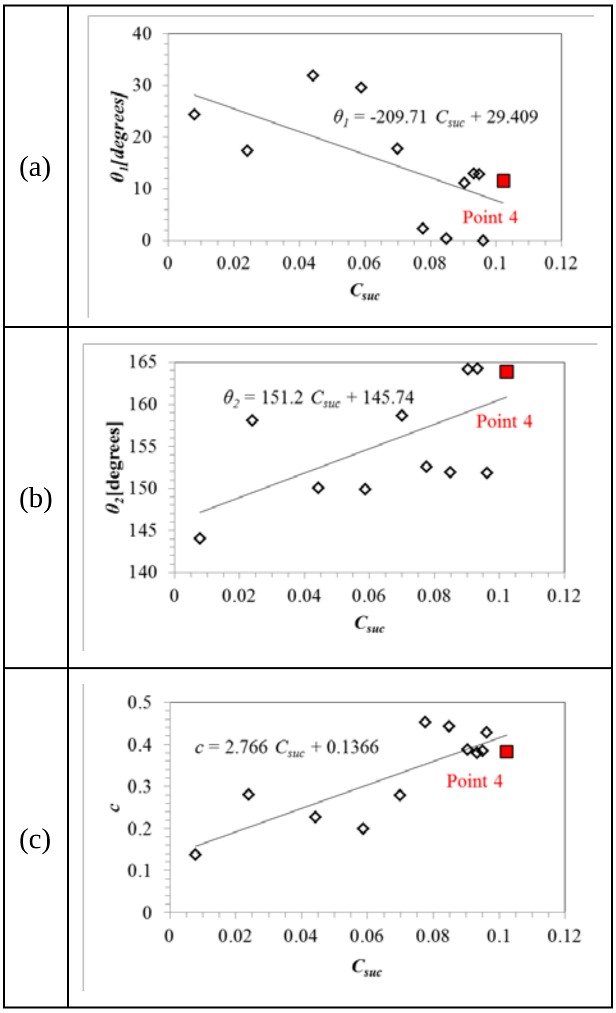

Fig. 56. *Re*=90: design variables versus objective function C_{suc}, for solutions along the Pareto front. The red square corresponds to stabilized flow at the minimal control effort, depicted by Point 4 in Fig. 53.

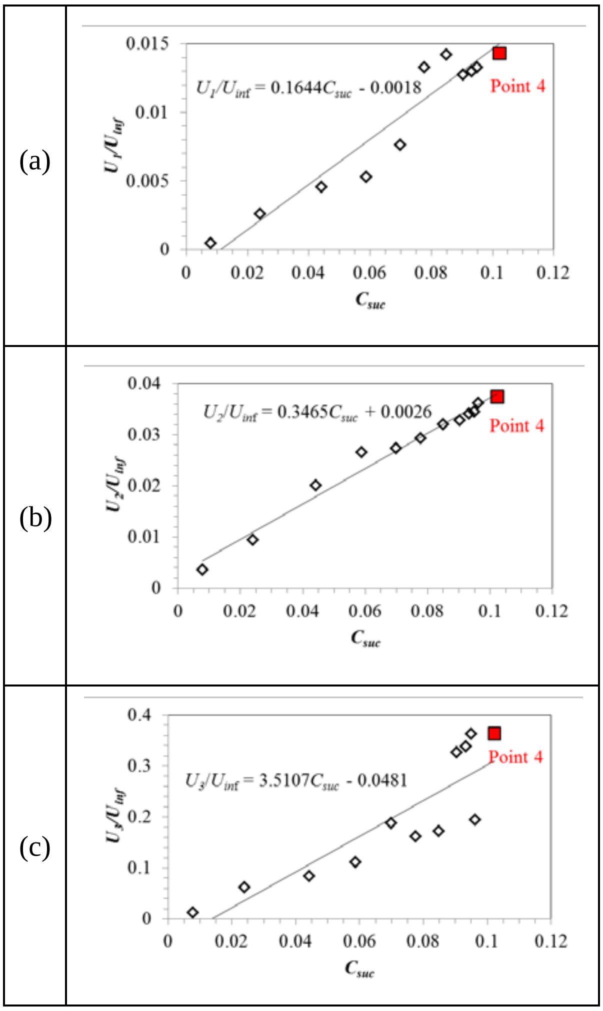

Fig. 57. *Re*=90: transpiration velocities versus objective function C_{suc}, for solutions along the Pareto front. The red square corresponds to stabilized flow at the minimal control effort, depicted by Point 4 in Fig. 53.

4.5.1.2 Optimization results for Re=180

Fig. 58 presents the computed objective function values for *Re*=180, also including a sketch of the Pareto front. In comparison to *Re*=90 (Fig. 53), a higher control effort (Csuc) to arrive at a corresponding flow state, expressed by the value of J_1, is confirmed. Four representative solutions of the Pareto front, as well as the one corresponding to uncontrolled flow, are depicted in Fig. 58. The corresponding values of design variables and objective functions are reported in Table 8. For these representative solutions, Fig. 59 presents the spatial distribution of suction/blowing velocity, as well as instantaneous vorticity isocontours, while Fig. 60 presents the computed signals of drag and lift coefficient. The optimal transpiration profiles (Fig. 59) are similar to the optimal transpiration profiles for *Re*=90, presented in Fig. 54. For solutions close to the limit of global flow stabilization, the blowing region is wider in comparison to the corresponding solutions at *Re*=90. Fig. 60 demonstrates that, by increasing control effort, the time-averaged drag coefficient decreases, and so do the fluctuating drag and lift components. With reference to the uncontrolled flow, the decrease in time-averaged drag is higher than the corresponding one at *Re*=90. For *Re*=180, the present optimization results have shown that a full cancellation of the vortex street is attained at a value of C_{suc}=0.163 (solution depicted by Point 4 in Fig. 58). In comparison to *Re*=90, this corresponds to an increase in control effort by 37%.

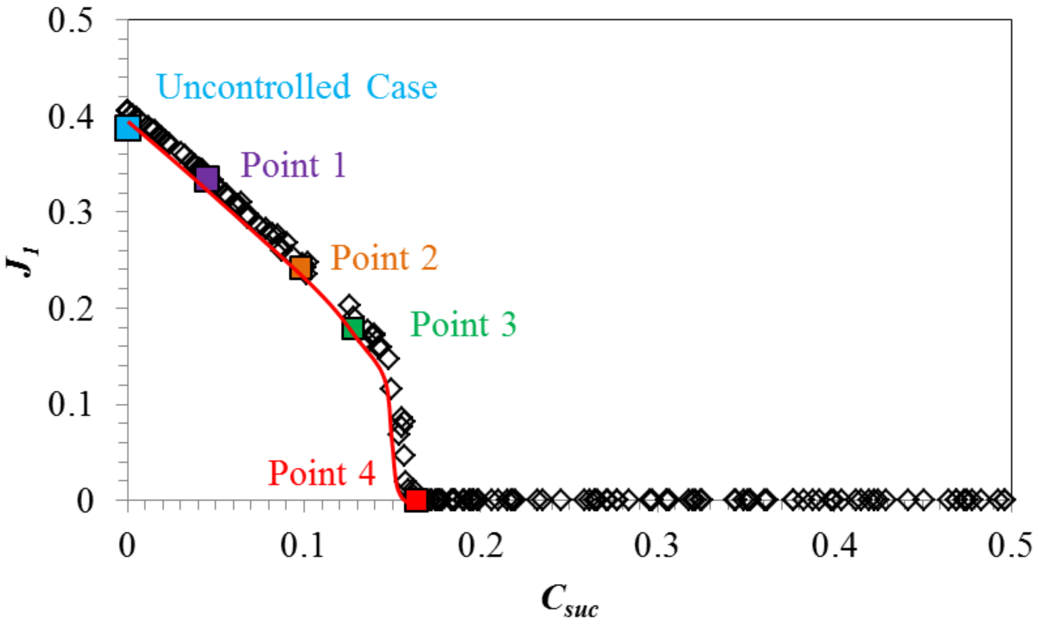

Fig. 58. *Re*=180: objective function J_1 vs. objective function C_{suc} (suction coefficient).

Table 8. *Re*=180: design variable values and corresponding objective function values, for the uncontrolled case, as well as for solutions 1-4, depicted in Fig. 58.

Case	C_{suc}	θ_1	θ_2	c	J_1
Uncontrolled	-	-	-	-	0.387
Point 1	0.043	30.61°	150.88°	0.059	0.343
Point 2	0.098	18.49°	145.41°	0.046	0.242
Point 3	0.128	22.30°	145.09°	0.152	0.179
Point 4	0.163	25.81°	144.18°	0.215	0.000

Solutions	Transpiration Velocity Profile	Vorticity Isocontours
Uncontrolled Case	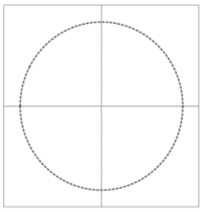	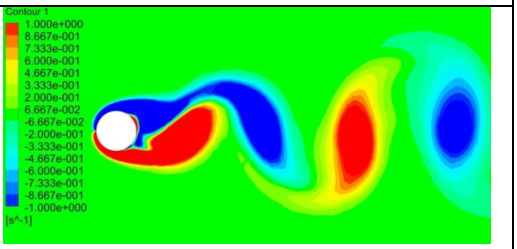
Point 1 C_{suc}=0.043	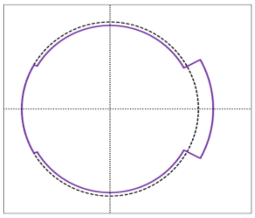	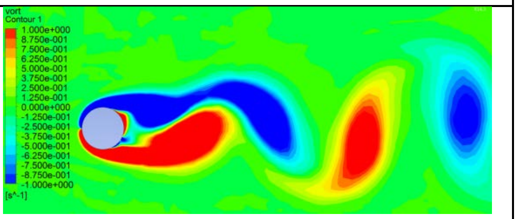
Point 2 C_{suc}=0.098	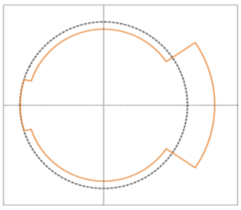	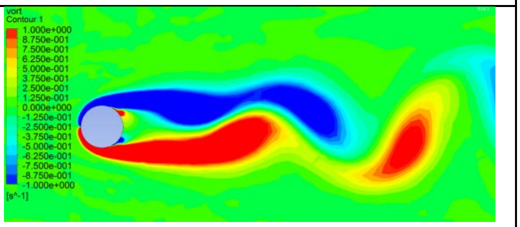
Point 3 C_{suc}=0.128	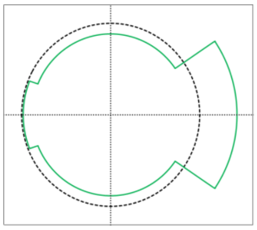	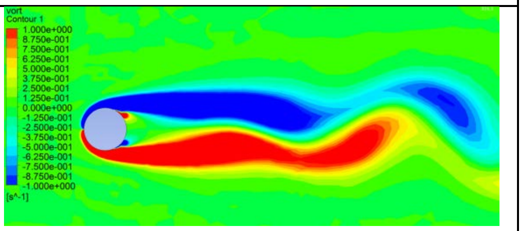
Point 4 C_{suc}=0.163	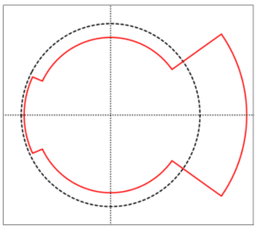	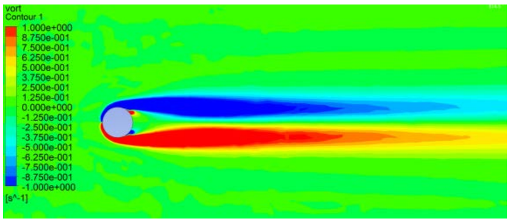

Fig. 59. *Re*=180: computed transpiration velocity profiles corresponding to solutions 1-4, depicted in Fig. 58 (left column), and corresponding color-coded contours of instantaneous vorticity (right column). The case of uncontrolled flow is also included.

Solutions	Drag Coefficient, C_D	Lift Coefficient, C_L
Uncontrolled Case	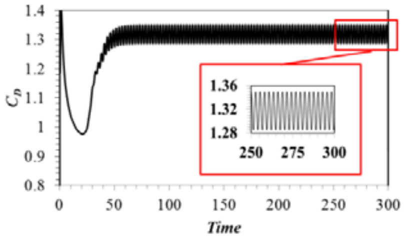	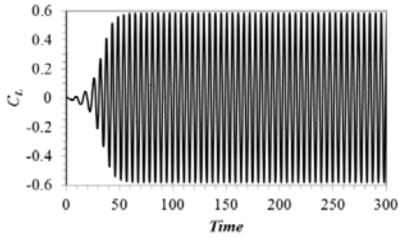
Point 1 C_{suc}=0.043	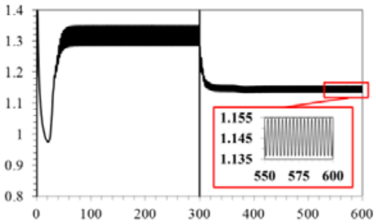	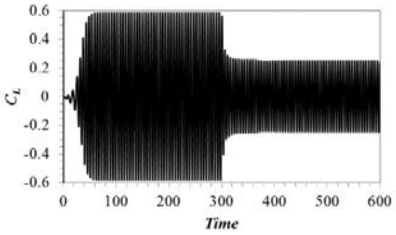
Point 2 C_{suc}=0.098	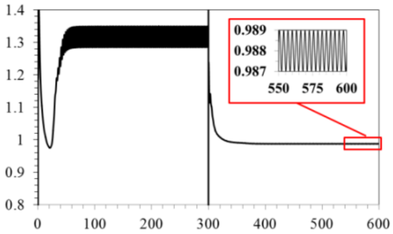	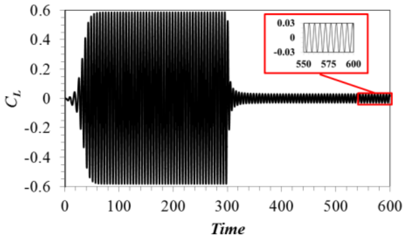
Point 3 C_{suc}=0.128	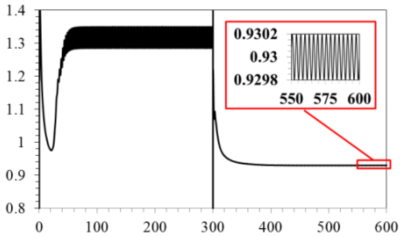	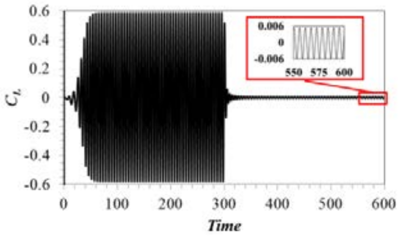
Point 4 C_{suc}=0.163	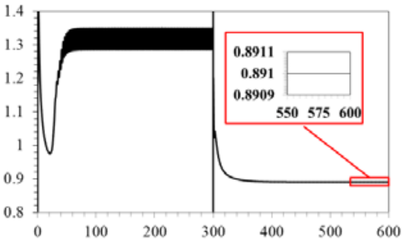	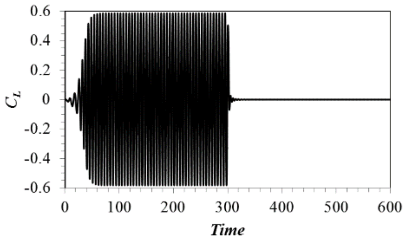

Fig. 60. *Re*=180: drag and lift coefficient signals for solutions 1-4, depicted in Fig. 58, and for the case of uncontrolled flow. Active open-loop control in terms of suction/blowing is implemented at *t*=300.

4.2.5 Optimal solutions: characterization of flow instability

Base flow calculations are performed for Re=90, for the four representative optimal solutions highlighted in Fig. 53 with colored squares, as well as for the case of uncontrolled flow. Fig. 61a,b presents the values of non-dimensional vorticity thickness, δ_w/D, and velocity ratio, R, at different streamwise locations, x/D. Clearly, an increase in control effort, C_{suc}, results in a mild decrease in vorticity thickness, as well as in a substantial decrease in the velocity ratio (reduced backflow). Further, curve-fitting of velocity profiles extracted from the base flow field (x/D=0.5 to 8.0) with the two-parameter (R, N) profile equation introduced by Monkewitz and Nguyen (1987), and placement of the solutions on the R-$1/N$ plot (Fig. 61c) demonstrates a consistent decrease in the intensity and extent of absolute instability at increasing control effort.

Next, local instability analysis calculations are performed for these four representative base flows, as well as for the uncontrolled base flow. The computed values of absolute local linear frequency, $St_0=\omega_{0,r}/(2\pi)$, and asolute growth rate, $\omega_{0,i}$, are presented in Fig. 62. Fig. 62a shows that an increase in control effort, C_{suc}, results in an increase of local linear frequency, throughout the near wake ($x/D < 8$); its maximum and minimum values, $St_{0,max}$ and $St_{0,min}$, are reported in Table 9. Fig. 62b demonstrates a substantial decrease of both the extent of the absolutely unstable regime and the local absolute growth rates, as the control effort (C_{suc}) increases; stable flow is attained at a critical level of control effort.

Further, the stability of global flow is characterized by analyzing transient lift signals in the frame of the Stuart-Landau equation. Results are reported in Table 9 in terms of the global growth rate and linear frequency, confirming a negative growth rate for Point 4. The linear global frequency is consistently lower than the corresponding non-linear one (St), also reported in Table 9. Both global frequencies lie within the range of local linear frequencies, for all fields considered in Table 9. Table 9 also shows that the maximum local growth rate, $\omega_{0i,max}$, the extent of absolute instability, as well as the integral I_g, are decreasing at increasing control effort (C_{suc}).

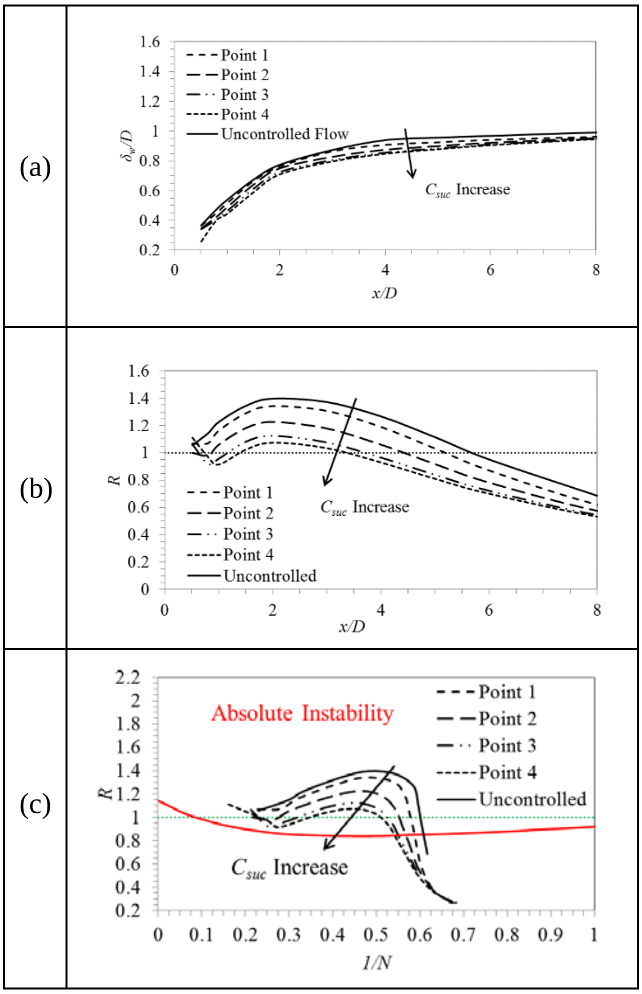

Fig. 61. *Re*=90: characterization of streamwise velocity profiles, for solutions 1 to 4, depicted in Fig. 53, and for the case of uncontrolled flow. (a) Velocity ratio vs. streamwise coordinate, (b) vorticity thickness vs. streamwise coordinate, and (c) velocity ratio vs. profile parameter 1/*N*.

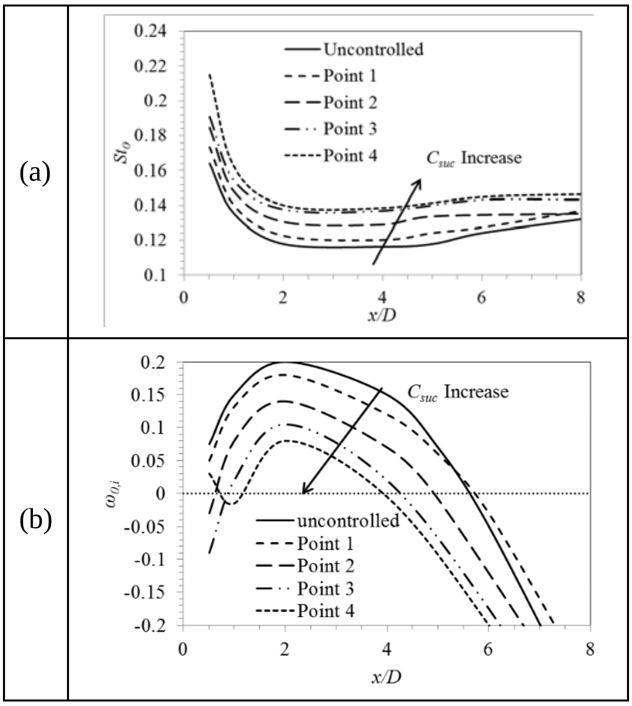

Fig. 62. *Re*=90: values of local stability properties vs. streamwise coordinate, for solutions 1 to 4, depicted in Fig. 53, and for the case of uncontrolled flow. (a) Absolute frequency, and (b) absolute growth rate.

Table 9. Quantities characterizing the flow local and global stability, for representative solutions of the optimization problem at *Re*=90.

Case	Global Linear Frequency, $s=\sigma_r+i\sigma_i$		*St*	Local Linear Frequency Range (*x/D*<8)		$I_g=\int_{x_a}^{x_b}\sqrt{\omega_{0,i}(x)}dx$ $\omega_{0,i}(x)>0$		
	σ_r	$St_{g,l}=\frac{\sigma_i}{2\pi}$		$St_{0,\min}$	$St_{0,\max}$	$\omega_{0,i\,max}$	x_b-x_a	I_g
Uncontrolled Flow	0.0898	0.128	0.158	0.118	0.165	0.200	5.30	1.89
Point 1	0.0727	0.127	0.155	0.123	0.178	0.180	5.20	1.72
Point 2	0.0555	0.129	0.150	0.132	0.188	0.135	4.30	1.09
Point 3	0.0033	0.120	0.143	0.139	0.192	0.105	3.37	0.61
Point 4	-0.0151	0.141	-	0.140	0.218	0.075	2.80	0.29

4.4 Summary of chapter 4

The present chapter has addressed the problem of optimal suppression of the vortex street in flow past a cylinder, at low Reynolds numbers, by means of an active open-loop control scheme. Here, a piecewise uniform suction/blowing profile was applied on the entite cylinder surface. First, parametric computational studies were performed, regarding application of suction/blowing in three regimes of the cylinder surface, namely: (a) the front stagnation point region, (b) the sideway region, and (c) the rear stagnation point region. The results have demonstrated that application of suction in the sideway or in the front stagnation point region, and blowing in the rear stagnation point region induce flow stabilization. Guided by these results, an optimization problem was formulated and solved, consisting in the partial or full suppression of the Kármán vortex street, at a minimal control effort, under the constraint of zero net mass transpiration. Complete vortex street cancelation was attained at a control effort 30% lower, in comparison to previous studies. Analysis of of the optimal solutions by means of local stability calculation has shown a decrease in both the extent and intensity of local absolute instability with control effort (C_{suc}), resulting in stabilization of the global flow at a critical level of control effort.

Chapter 5: Feedback flow control: optimization of control schemes

In the two previous chapters, a passive and an active open-loop control scheme were implemented, aiming at suppressing the Kármán vortex street in flow past a circular cylinder. The passive control scheme consisted in implementing surface hydrophobicity, whereas the active open-loop control scheme consisted in applying mass transpiration. In the context of both control schemes, vortex street cancelation has been attained at a minimal control effort, by formulating and solving properly defined optimization problems. However, due to the substantial costs associated with implementation and operation, it is essential to investigate whether a partial or complete suppression of flow unsteadiness can be attained by means of even lower levels of control effort. To this end, in the frame of the above control measures, two feedback control schemes are developed and optimized, utilizing: (a) time-dependent mass transpiration, and (b) time-dependent slip conditions. In both schemes, actuation is based on proportional feedback control, utilizing the transverse velocity signal in the wake, at a point on the domain centerline. The optimization results demonstrate a substantial reduction in control effort with feedback control, in the frame of the present feedback control schemes.

5.1 Feedback control using mass transpiration: validation test

In flow control applications, the realization of a feedback control scheme can be achieved by implementing: (a) one or more sensors measuring appropriate signals, and (b) actuators providing the desired control action. In flow past a cylinder, appropriate quantities to be measured are the pressure on the cylinder surface via pressure sensors (Aamo and Krstic, 2003), or the vector velocity in the near wake regime via hot wire sensors (Roussopoulos, 1993). Actuation consisting in mass transpiration can be realized by means of tiny holes on the cylinder wall, and may utilize zero net mass flux (ZNMF) actuators or micro/synthetic jet actuators; for an extensive review see Glezer and Amitay (2002), and Cattafesta and Sheplak (2011).

In the present study, we consider a closed loop control scheme, proposed by Park et al. (1994), utilizing time-dependent mass transpiration through two slots on the cylinder surface (Fig. 63). The slots are located symmetrically around the front stagnation point, on an arc extending from $\theta_{min}=97^{o}$ to $\theta_{max}=113^{o}$ in the upper half plane; the choice of slot location takes into account the location of separation point. In the present study, the scheme is tested for $Re=60$, for which separation in base flow corresponds to an angle of $\theta_s=120^{o}$ with respect to the front stagnation point (see section 3.1). To control the (antisymmetrical) shedding mode, an antisymmetrical transpiration is implemented from the two slots, i.e. the instantaneous transpiration flow rate is zero. Uniform transpiration velocity profiles are implemented (whereas parabolic profiles have been used in Park et al. (1994)). In practice, the physical actuation can be provided by ZNMF actuators (Cattafesta and Sheplak, 2011) properly distributed on the area of interest, taking into account the constraint of zero net flow rate. Here, the instantaneous velocity of blowing/suction, $u_{SB}(t)$, considered as the control input signal, $u(t)$, is calculated based on the proportional feedback control scheme of Park et al. (1994), in which the input of a transverse velocity sensor located at $(x_s, 0)$, i.e. on the domain centerline, is used as the sensor signal. In an actual implementation, the velocity signal can be provided by a hot-wire sensor, measuring the vector velocity at the location of its placement (Roussopoulos, 1993).

In the present work, the feedback control law is defined as follows:

$$u(t) = u_{SB}(t) = k_p \frac{V(x_s,t)}{V_{\max}(t)} \tag{49}$$

$$V_{max}(t) = \max_{\tau \le t} |V(x_s,\tau)| \tag{50}$$

where $V(x_s,t)$ is the instantaneous velocity input, $V_{max}(t)$ is its actual maximal absolute value, and k_p the value of the proportional feedback gain. Since the sensor of the measured signal is located on the domain centerline, the feedback action diminishes as the desired state of reduced unsteadiness is approached. Evidently, different values of the sensor location, x_s, correspond to different values of phase shift of the feedback signal.

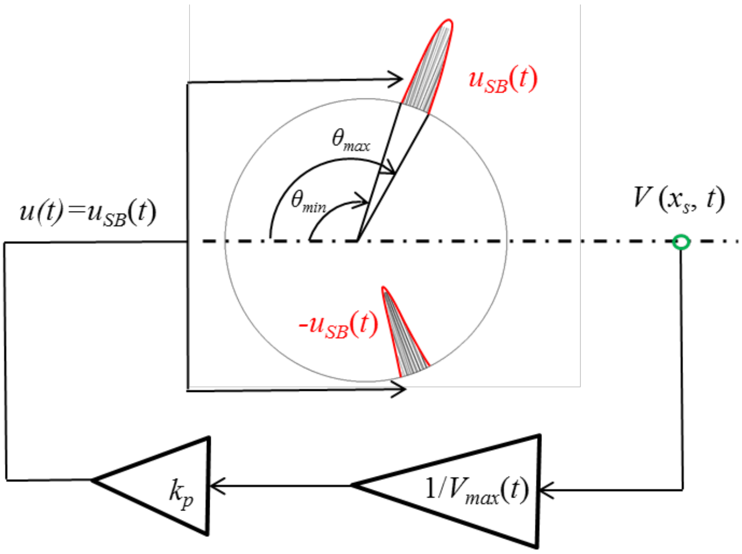

Fig. 63. Proportional feedback loop control scheme (Park et al., 1994): the location of the feedback sensor, x_s, the extent of a transpiration slot, delimited by angles θ_{min} and θ_{max}, the proportional gain, k_p, as well as the control input signal, $u(t)$, are depicted.

Here, a simulation is performed for flow under feedback control, for the velocity sensor located x_s=2.75, and a proportional gain value k_p=0.35, as in Park et al. (1994). Fig. 64 presents the results of the present study, as well as those of Park et al. (1994), verifying a very good agreement. In particular, Fig. 64a, presenting the streamline pattern at a large time, demonstrates the complete cancelation of the Kármán vortex street, as illustrated by the formation of the steady recirculation zones. Further, the streamwise velocity signal, u, at x=2.5, y=0.5 attains a constant value at large times (Fig. 64b). Finally, the full suppression of force fluctuations is verified by the drag and lift coefficient signals, presented in Fig. 65.

Case	(a) Streamline pattern	(b) Streamwise velocity, u, at x=2.5, y=0.5
Present study	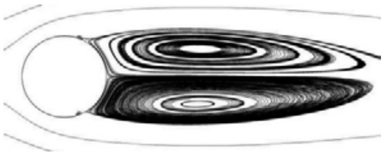	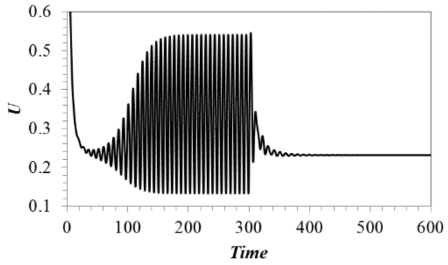
Park et al. (1994)	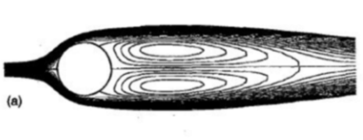	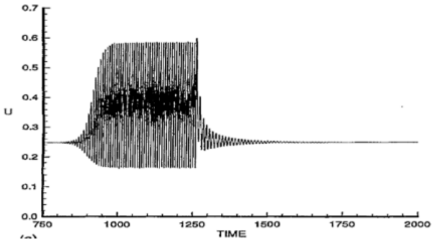

Fig. 64. Computational results of the present study and of Park et al. (1994) for Re=60, k_p=0.35, x_s=2.75: (a) instantaneous streamline pattern at a large time, and (b) signal of streamwise velocity, u, at x=2.5, y=0.5. In the present simulation active feedback control in terms of time-dependent suction/blowing is implemented at t=300, and in the one of Park et al. (1994) at t=1200.

(a)	(b)
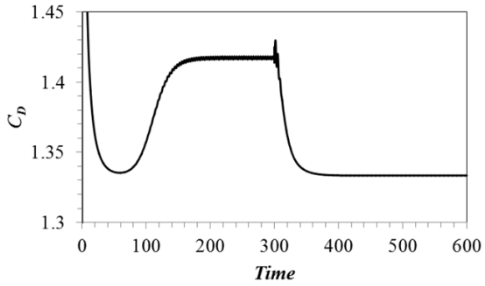	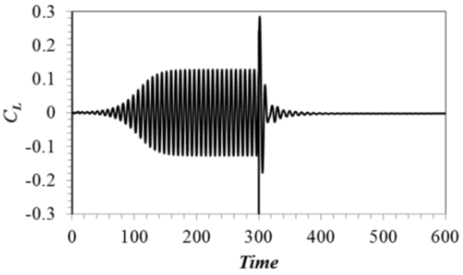

Fig. 65. Re=60, k_p=0.35, x_s=2.75: drag and lift coefficient signals. Active feedback control in terms of time-dependent suction/blowing is implemented at t=300.

5.2 Optimization of feedback control with time-dependent mass transpiration

Park et al. (1994) performed a large number of simulations, for different values of the feedback control parameters, i.e. the sensor location, x_s, and the value of proportional gain, k_p. They concluded that cancelation of the vortex street is only feasible at low Reynolds numbers, in particular for $Re \leq 60$. However, even in this regime, flow stabilization has been found to be extremely sensitive to small modifications of the feedback control parameters. In particular, for Re=60 and values of proportional gain k_p=0.2 and k_p=0.35, vortex street cancelation could only be attained for a sensor located within the narrow region $2.7<x_s<3$.

The goal of the present section is to implement the control scheme proposed by Park et al. (1994) within the frame of a systematic optimization approach, and to investigate whether improved solutions can be attained. To this end, a two-objective minimization problem is formulated, aiming at partial or complete cancelation of the vortex street, at a minimal control effort. Here, the first objective function is associated with the flow global stability, while the second one quantifies the control effort. Optimization results are reported for *Re*=60.

5.2.1 Design variables and search space

Four design variables are utilized in the present implementation: the streamwise location of the transverse velocity sensor, x_s, the proportional gain, k_p, and the arcs θ_{min} and θ_{max}, defining the extent of the mass transpiration slots. A broad domain of definition is considered for each of the four design variables:

$$1 \le x_s \le 5,\ 0.1 \le k_p \le 0.5,\ 99^o \le \theta_{\min} \le 104^o,\ 111.6^o \le \theta_{\max} \le 120.6^o \tag{51}$$

The selection of the search space boundaries is guided by the results of Park et al. (1994).

5.2.2 Objective functions

Two objective functions are introduced.

(a) First objective function, J_1:

The first objective function, J_1, related to the flow global stability, is the same one introduced in the optimization problem studied in Chapter 3 (see eqs. 32, 33, 34).

(b) Second objective function, J_2:

The control effort increases with the transpiration velocity (determined from the product of the transverse velocity signal and the proportional feedback gain, k_p) and the arc of the transpiration slot. Thus, a corresponding objective function, J_2, is defined as follows:

$$J_2 = S_{V_{x_s}} k_p (\theta_{\max} - \theta_{\min}) \tag{52}$$

where the standard deviation of the transverse velocity, $S_{V_{x_s}}$ at the sensor point, x_s, is defined as:

$$S_{V_{x_s}} = \sqrt{\frac{1}{N-1}\sum_{i=1}^{N}\left(V_{t_i,x_s}\right)^2} \tag{53}$$

where V_{t_i,x_s} is the transverse velocity at the sensor point, x_s, calculated at time instant t_i.

5.2.3 Optimization problem

The present optimization problem is stated as follows: find the optimum combinations of the problem design variables (x_s, k_p, θ_{min}, θ_{max}), which simultaneously minimize objective functions J_1, J_2. The optimization problem, as formulated here, is solved for a representative Reynolds number value, *Re*=60 (for which the flow is two-dimensional), also considered in the study of Park et al (1994).

5.2.4 Optimization results

The results of the optimization problem are presented in Fig. 66, in terms of the problem objective functions, J_1 and J_2. Each combination of the four design variables (k_p, θ_{min}, θ_{max}, x_s) corresponds to a different implementation, resulting in either unstable or stable flow (values of function J_1 positive or zero, respectively). It is noted that full flow stabilization is feasible for Re=60 at very low levels of control effort; the stabilized flow remains stable when maintaining the same (low) level of control effort.

In Fig. 66, four stabilized solutions are depicted by Points 1-4; all of them are characterized by near zero values for both objective functions. The corresponding values of design variables and objective functions are reported in Table 10. Table 10 demonstrates that global flow stabilization is feasible for locations of the velocity sensor in the region $2.879 \leq x_s \leq 3.168$, for proportional gain values in the range $0.138 \leq k_p \leq 0.413$. Thus, the present optimization gives a regime for the velocity sensor practically coinciding to the one suggested by Park et al. (1994), and a wider k_p range. Further, the present results illustrate that a reduction of the extent of the transpiration slot ($\varphi = \theta_{max} - \theta_{min}$) from $\varphi=16^o$ to $\varphi=11^o$ is feasible (solution depicted by Point 4 in Fig. 66). The lift and drag coefficient signals corresponding to Points 1-4 verify convergence to stabilized flow after the onset of feedback control (see Fig. 67). In summary, the present optimization scheme verifies global flow stabilization at Re=60, while also extending the range of proper design parameters, in comparison to the results of Park et al. (1994).

In order to investigate in more detail the global flow stability of the optimal solutions, depicted in Fig. 66 by points 1-4, the corresponding lift coefficient signals, presented in Fig. 67, are analyzed following the signal analysis procedure outlined in section 1.4.2, yielding the components of the global frequency, $s=\sigma_r+i\sigma_i$, i.e. the global linear growth rate, σ_r, and the linear frequency, σ_i; the results are included in Table 10. Following the global linear instability analysis and corresponding discussion of Park et al. (1994), in the frame of feedback control, global frequencies define the poles of the system. It should be noted that the present study considers only the fundamental global frequency (pole), which satisfies the Stuart-Landau equation (Schumm et al., 1994). Fig. 68 presents the fundamental global frequencies on the complex plane (σ_r-σ_i) for the uncontrolled flow (open loop pole), as well as for the optimal solutions depicted by Points 1-4 in Fig. 66 (closed loop poles). On one hand, considering the uncontrolled flow at Re=60, the positive value of the global linear growth rate, σ_r, verifies the global flow instability. On the other hand, for the optimal solutions depicted by Points 1-4 in Fig. 66, the negative values of the global linear growth rate, σ_r, verifiy the complete cancellation of the Kármán vortex street. Further, the substantial reduction in the value of σr from Point 1 to Point 4 demonstrates a corresponding increase of the stabilizing effects. The latter is in accordance with the corresponding decrease of transition time (between the uncontrolled flow and the stabilized flow), as demonstrated by the transient lift coefficient signals (Fig. 67).

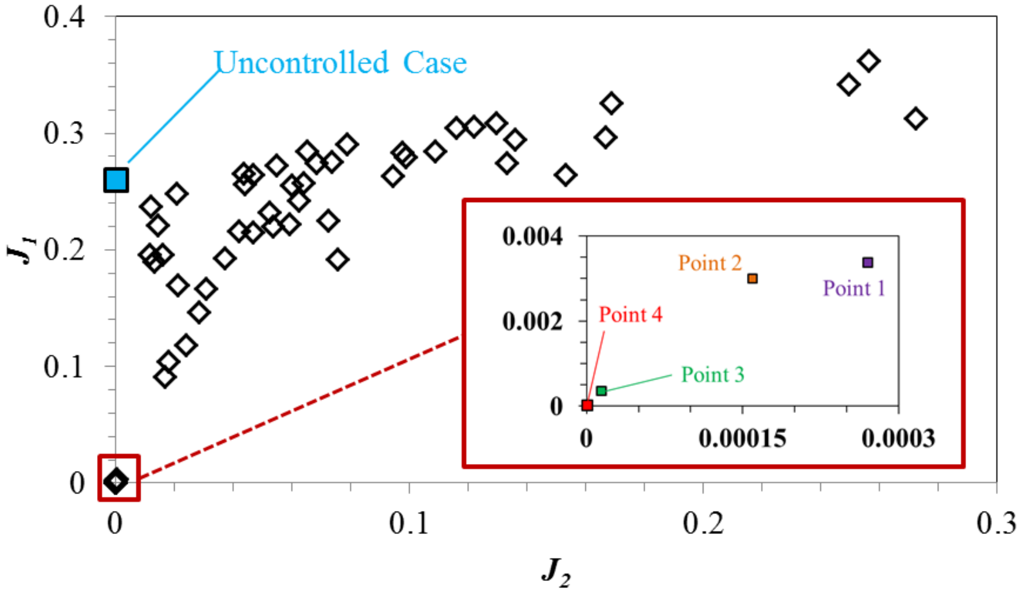

Fig. 66. *Re*=60: objective function J_1 vs. objective function J_2.

Table 10. *Re*=60: design variable values and corresponding objective function values, for the uncontrolled flow, as well as for optimal solutions 1-4, depicted in Fig. 66; the values of the components of the global linear frequency, *s*, i.e. the global linear growth rate, σ_r, and the linear frequency, σ_i, are also reported.

Case	k_p	θ_{min}	θ_{max}	x_s	J_1	J_2	σ_r	σ_i
Uncontrolled	-	-	-	-	0.2600000	0.00000000	0.041	0.762
Point 1	0.253	103^{o}	118^{o}	3.168	0.0033746	0.00027006	-0.014	0.897
Point 2	0.138	99^{o}	116^{o}	2.986	0.0030299	0.00015949	-0.016	0.785
Point 3	0.281	104^{o}	119^{o}	2.879	0.0003550	0.00001420	-0.022	0.661
Point 4	0.413	102^{o}	113^{o}	2.942	0.0000064	0.00000031	-0.026	0.837

Case	Drag Coefficient, C_D	Lift Coefficient, C_L
Point 1	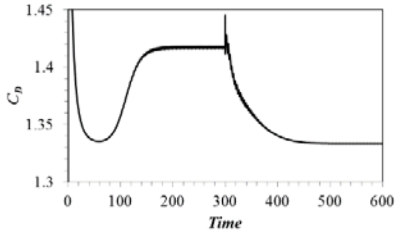	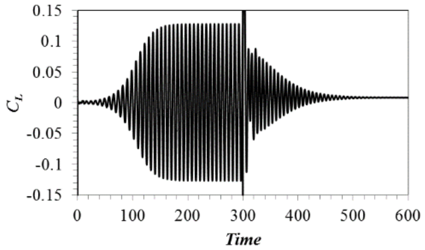
Point 2	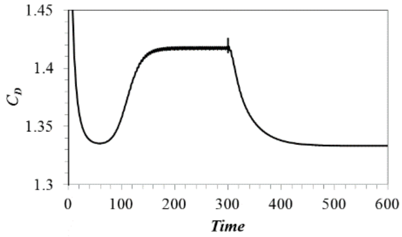	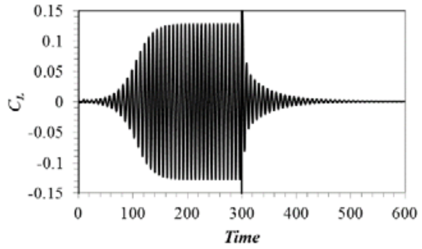
Point 3	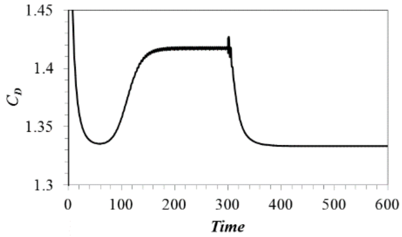	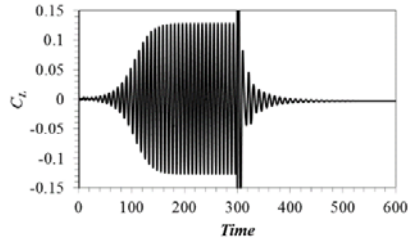
Point 4	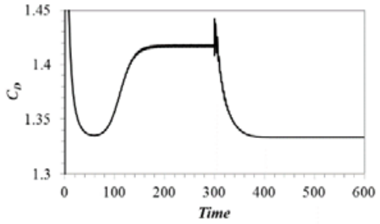	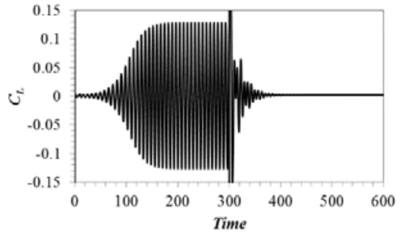

Fig. 67. *Re*=60: drag and lift coefficient signals for solutions 1-4, depicted in Fig. 66. Active feedback control in terms of time-dependent suction/blowing is implemented at *t*=300.

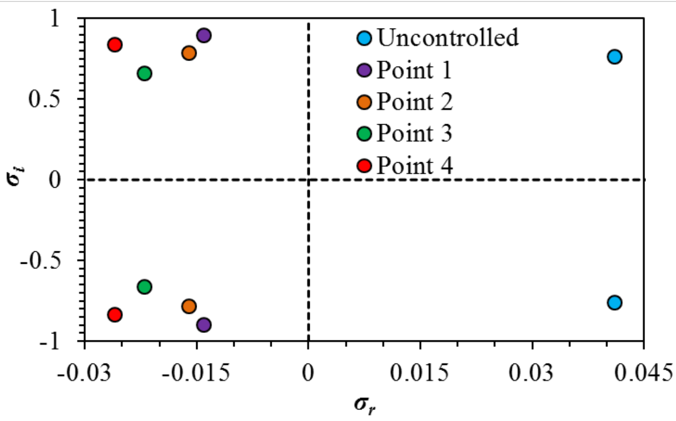

Fig. 68. *Re*=60: global frequencies for the uncontrolled case (open loop pole), as well as for optimal solutions 1-4 (closed loop poles), depicted in Fig. 66.

5.3 Feedback control utilizing time-dependent slip conditions

5.3.1 Proportional control concept utilizing controllable wetting properties

In chapter 3 it was demonstrated that implementing surface hydrophobicity on the entire cylinder surface results in decreased drag and lift forces, whereas vortex street cancellation can be attained at a critical level of control effort. Furthermore, the corresponding optimization study established that an optimal application of slip on a part of the cylinder surface may lead to a decrease in control effort of up to 50%, in comparison to implementing slip on the entire cylinder surface. Nonetheless, as the manufacturing of hydrophobic and superhydrophobic surfaces is still quite expensive, a further reduction in control effort is desired.

In order to achieve vortex street cancellation at even lower levels of control effort, using materials with controllable wetting properties appears as a possible choice. These materials modify their wetting properties when an external forcing is applied, e.g. optical, magnetic, mechanical, chemical, thermal or electrical; for an extensive review see Verplanck et al. (2007). Among these materials, those with controllable electro-wetting properties have been recently used in microelectromechanical systems (MEMS) applications, as for example in optical switches, in cooling of electronic circuits and in transport and mixing of micro-drops for purposes of printing (Mugele and Baret, 2005). Electrowetting actuators are based on the fact that it is possible, using an external electric field, with no mechanical parts, to control movement or quick change (within hundredths of a second). Further, it is should be noted that electrowetting actuators can be miniaturized to scales of less than a millimeter, and still be controlled with great precision using substantially low levels of energy (Mugele and Baret, 2005). Thus, materials with controllable (electro-)wetting properties can enable the application of time-dependent slip conditions on a surface, for feedback control studies.

The work of Park et al. (1994), as well as the results presented here (see previous section), demonstrated that in flow past a cylinder the application of an active feedback control scheme contributes to a substantial reduction in control effort, in comparison to an active feedforword control strategy. Guided by these results, the application of time-dependent slip conditions in the context of a feedback control scheme may lead to partial or complete suppression of the vortex street at a substantially lower level of control effort, in comparison to the corresponding passive control scheme with slip, presented in chapter 3.

In the present feedback control scheme, sketched in Fig. 69, an instantaneous transverse velocity at a point along the domain centerline, $V(x_s,t)$, is used as the sensor signal. A proper value of slip length, $b^*(t)$, is used as the control input signal, $u(t)$, calculated based on a proportional feedback control law within the frame of the Navier model, as follows:

$$u(t) = b^*(t) = \frac{1}{Re \cdot \tau^*} k_p \left| V(x_s, t) \right| \tag{54}$$

where k_p is the proportional feedback gain value. It should be noted that eq. 70 is in accordance with the passive slip condition, introduced in section 2.1 (see eq. 25).

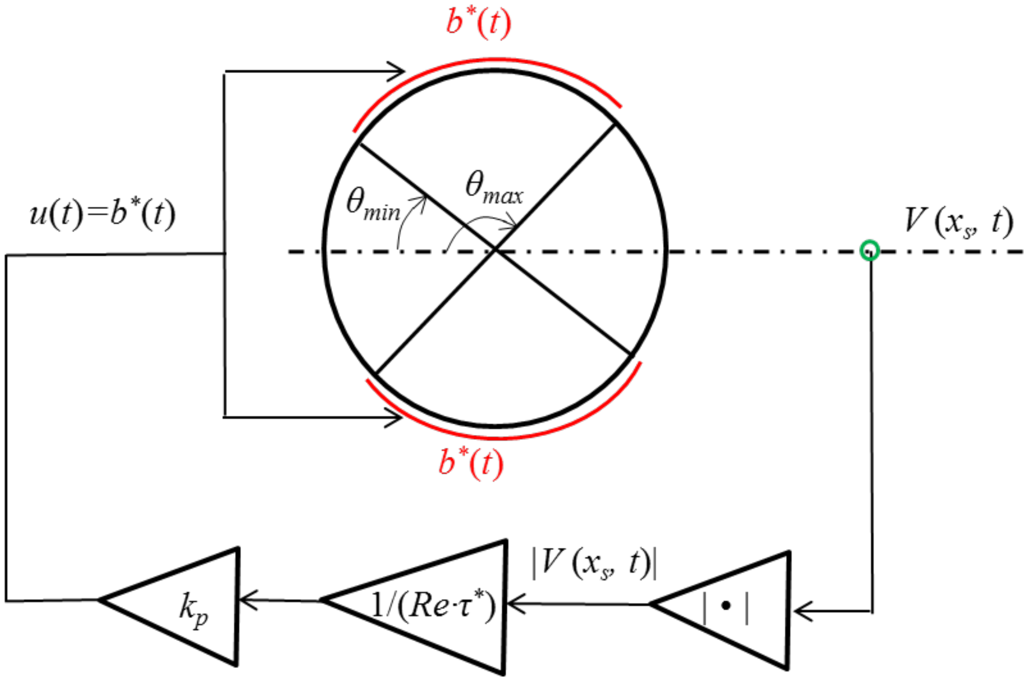

Fig. 69. Sketch of the present proportional feedback loop control scheme. The non-dimensional location of the sensor, x_s/D, the actuation regime (hydrophobic area extends between θ_{min} and θ_{max}), the proportional gain, k_p, as well as the control input signal, $u(t)$, are depicted.

5.3.2 Application of controllable wettability on the entire cylinder surface

The feedback control approach of Park et al. (1994), as well as the present optimization results (see section 5.2), demonstrated the strong sensitivity of the flow instability to the feedback control parameters. Here, the stabilizing effects of the controllable wettability properties are first investigated for Re=60, in terms of a parametric study. In particular, the sensitivity of results on sensor location, x_s, and on the proportional gain value, k_p, is studied.

In a first step, the proportional gain is fixed at the representative value of 0.5, and the feedback sensor location is considered as a free parameter. Fig. 70 presents representative flow quantities as a function of the streamwise coordinate of the control sensor, x_s, in particular the lift coefficient amplitude, $C_{L,ampl}$ (Fig. 70a), the time-averaged drag coefficient, $<C_D>$ (Fig. 70b) and the maximal value of the (time-dependent) slip length, b^*_{max} (Fig. 70c). Fig. 70a demonstrates the decreasing trend of lift coefficient amplitude, as the sensor is moved farther downstream. When the feedback sensor is placed at x_s=7, the minimal value of the lift coefficient amplitude is attained, corresponding to very low levels of flow unsteadiness; however, vortex street is not fully cancelled. For a sensor location x_s>7, the destabilizing effects are increased. The time-averaged drag coefficient, presented in Fig. 70b, is a decreasing function of the sensor location, for x_s<5, an increasing function of the sensor location, for 5<x_s<7, and finally a decreasing function of the sensor location, for x_s>7; for x_s=7, the time-averaged drag coefficient attains a local maximum. Finally, Fig. 70c verifies that the maximum value of the (time-dependent) slip length reaches a minimum at x_s=7, corresponding to the minimization of control effort.

In order to investigate in more detail the influence of the location of feedback sensor on the flow stability, we present in Fig. 71 and in Fig. 72 the lift coefficient signal, C_L, as well as the time-dependent slip length, b^*_{time}, for several sensor locations (k_p=0.5). Fig. 71 verifies that, as the sensor is moved downstream within the regime $1<x_s<7$, the lift signal amplitude, as well as the maximum value of slip length, are reduced; the minimal values are attained at x_s=7. On the other hand, for $7<x_s<12$, Fig. 72 demonstrates an increasing trend of both the lift signal amplitude and the maximum in time of slip length.

In a second step, utilizing the above results, we fix the feedback sensor location at x_s=7, and vary the proportional gain, k_p; computed values of representative flow quantities are presented in Fig. 73. Fig. 73a and Fig. 73b demonstrate that the lift signal amplitude, $C_{L,ampl}$, as well as the time-averaged drag coefficient, $<C_D>$, are both decreasing functions of the proportional gain. On the other hand, the maximum value of the (time-dependent) slip length, b^*_{max}, is an increasing function of the proportional gain (Fig. 73c). It is worth noting that, for k_p>0.3, further increase of k_p results in an imperceptible modification of flow statistics.

The present parametric study thus generally demonstrates that moving the feedback sensor location downstream and increasing the proportional gain value contribute to a substantial reduction in flow unsteadiness. It is noted that a complete cancelation of flow unsteadiness has not been attained; nonetheless, a comparison with our results of passive flow control reported in chapter 3 suggests a reduction by two orders of magnitude in control effort with feedback control.

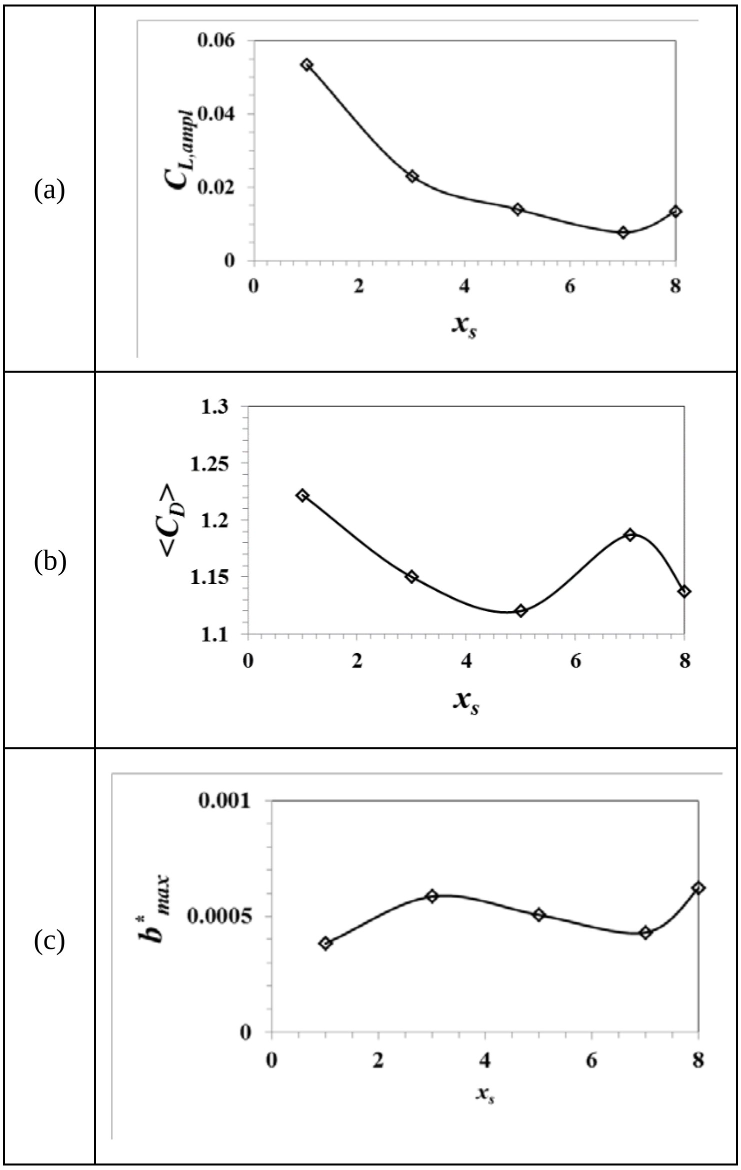

Fig. 70. *Re*=60: flow quantities versus streamwise sensor location, x_s, at a proportional gain value of k_p=0.5: (a) Lift coefficient amplitude, $C_{L,ampl}$, (b) time-averaged drag coefficient, $<C_D>$, and (c) maximum value of non-dimensional slip length, b^*_{max}.

Sensor Location, x_s/D	Lift Coefficient signal, $C_L(t)$	Slip length, b^*_{time}
1.0	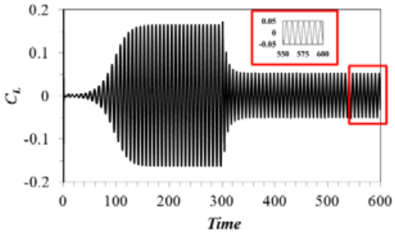	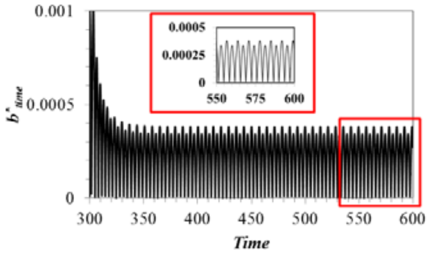
3.0	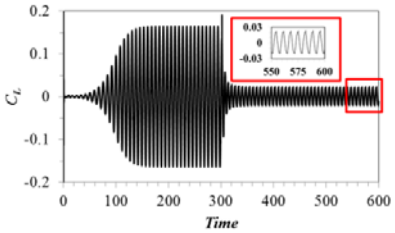	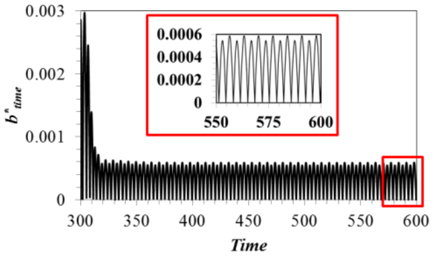
5.0	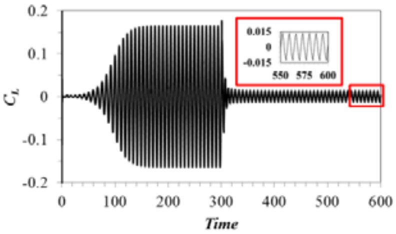	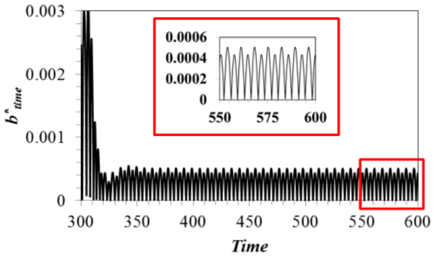
7.0	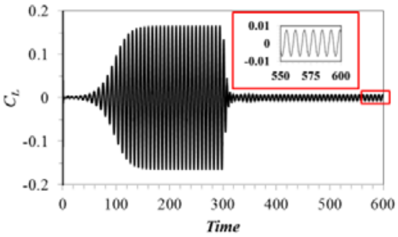	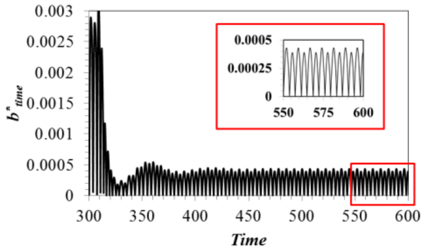

Fig. 71. Re=60, k_p=0.5: lift coefficient and slip length signals, for different streamwise locations of the sensor in the near wake. Active feedback control in terms of time-dependent slip conditions is implemented at t=300.

<table>
<tr><th>Sensor Location, x_s/D</th><th>Lift Coefficient signal, $C_L(t)$</th><th>Slip length, b^*_{time}</th></tr>
<tr><td>8.0</td><td>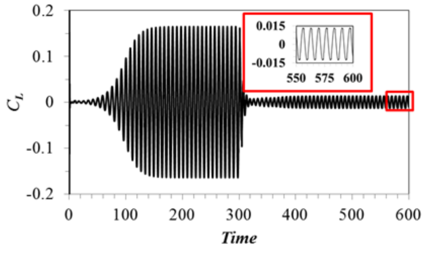
</td><td>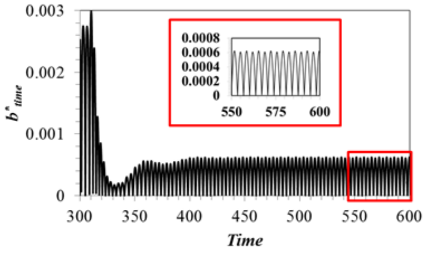
</td></tr>
<tr><td>10.0</td><td>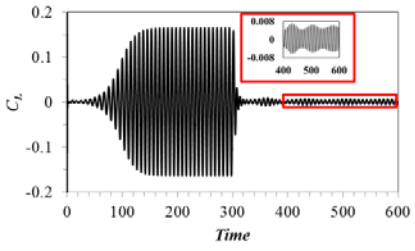
</td><td>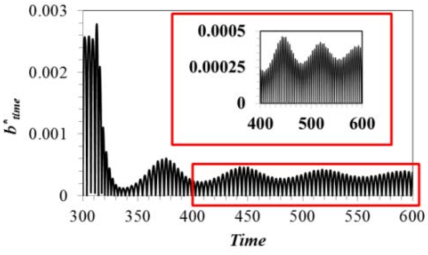
</td></tr>
<tr><td>12.0</td><td>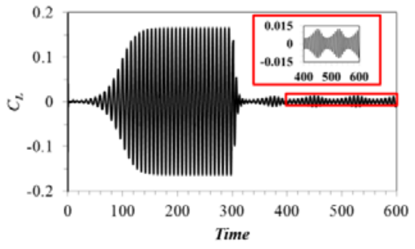
</td><td>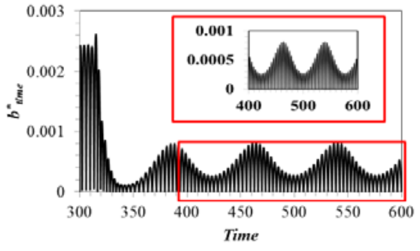
</td></tr>
</table>

Fig. 72. *Re*=60, k_p=0.5: lift coefficient and slip length signals, for different streamwise locations of the sensor in the far wake. Active feedback control in terms of time-dependent slip conditions is implemented at *t*=300.

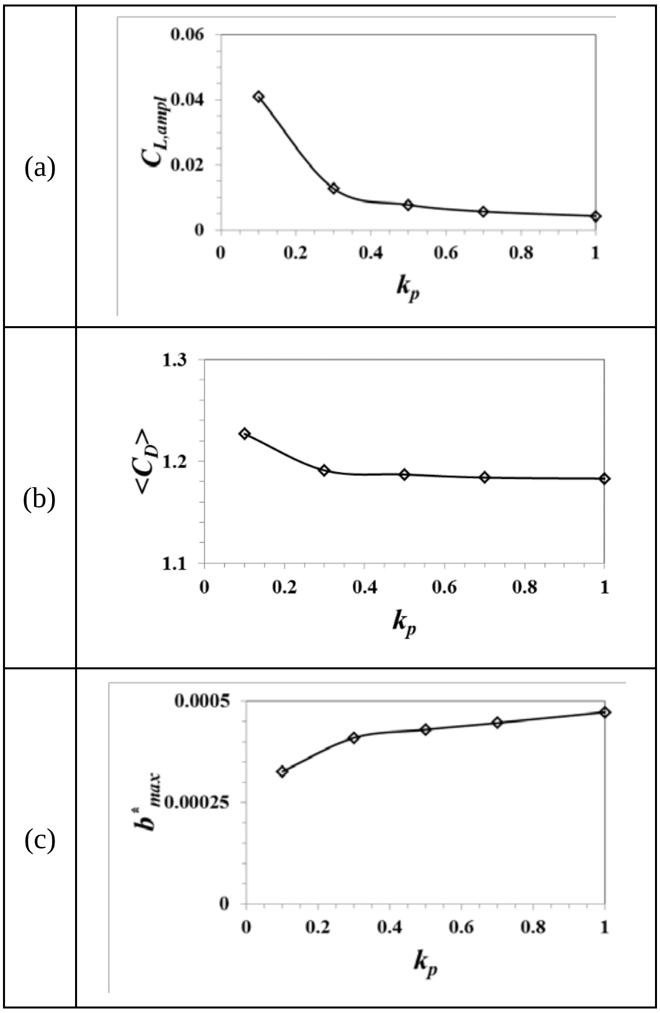

Fig. 73. *Re*=60: flow quantities versus proportional gain value, k_p, when the sensor is located at x_s=7: (a) Lift coefficient amplitude, $C_{L,ampl}$, (b) time-averaged drag coefficient, $<C_D>$, and (c) maximum value of non-dimensional slip length, b^*_{max}.

5.4 Optimization of feedback control with time-dependent slip

In the previous section, a feedback control scheme, utilizing time-dependent slip conditions on the entire cylinder surface, was parametrically investigated. Due to the high cost of implementing controllable surface hydrophobicity, it is of main consideration to reduce the extent of the corresponding regime. In the present section, the feedback control parameters, i.e. the sensor location, x_s, and the proportional gain value, k_p, as well as the angles defining the hydrophobic region, θ_{min} and θ_{max}, are subject to an optimization procedure, aiming at the partial or complete suppression of the Kármán vortex street at a minimal control effort. To this end, a two-objective minimization problem is formulated. The first objective function is associated with the flow's global stability, while the second one quantifies the time-dependent control effort. Optimization results are reported for *Re*=60 and for *Re*=90.

5.4.1 Design variables and search space

Four design variables are utilized in the present implementation: the streamwise location of the transverse velocity sensor, x_s, the proportional gain, k_p, and the angles θ_{min} and θ_{max} defining the extent of the area where the time-dependent slip condition is applied. A broad domain of definition is considered for each of the four design variables:

$$1 \le x_s \le 10,\ 0 \le k_p \le 0.5,\ 0^o \le \theta_{min} \le 70^o,\ 110^o \le \theta_{max} \le 180^o \tag{55}$$

The selection of the search space boundaries for θ_{min}, θ_{max} was guided by the optimization problem with passive slip (see section 3.3.1). Regarding the proportional gain, k_p, and the sensor location, x_s, the definition of search space has been based on the results of the parametric analysis reported in section 5.3.

5.4.2 Objective functions

Two objective functions are introduced.

(a) First objective function, J_1:

The first objective function, J_1, related to the flow global stability, is the same one introduced in the optimization problem studied in Chapter 3 (see eqs. 32, 33, 34).

(b) Second objective function, J_2:

The control effort increases with slip length (determined in terms of the product of the transverse velocity at the sensor location and the proportional feedback gain) and the half-arc of the slip region. Thus, a corresponding objective function, J_2, is defined as follows:

$$J_2 = S_{V_{x_s}} k_p \frac{(\theta_{\max} - \theta_{\min})}{2} \tag{56}$$

where the standard deviation of the transverse velocity, $S_{V_{x_s}}$ at the sensor point, x_s, is defined (at large times) as:

$$S_{V_{x_s}} = \sqrt{\frac{1}{N-1}\sum_{i=1}^{N}\left(V_{t_i,x_s}\right)^2} \tag{57}$$

where V_{t_i,x_s} is the transverse velocity at the sensor point x_s calculated at time instant t_i.

5.4.3 Optimization problem

The optimization problem is stated as follows: find the optimum combinations of the problem design variables (x_s, k_p, θ_{min}, θ_{max}), which simultaneously minimize objective functions J_1, J_2.

The optimization problem, as formulated here, is solved for two representative Reynolds number values, *Re*=60 and *Re*=90, for which the flow is two-dimensional.

5.4.4 Optimization results

5.4.4.1 Optimization results for Re=60

The optimization results for *Re*=60 are presented in Fig. 74, in terms of the values of the problem objective functions, J_1, J_2. Each combination of the problem design variables (k_p, x_s, θ_{min}, θ_{max}) corresponds to a different implementation of the present feedback control scheme. Fig. 74 demonstrates that the application of time-dependent slip condition by means of feedback control results in partial suppression of flow unsteadiness. However, it should be noted that the control effort used, quantified by the objective function J_2, attains near zero levels.

Four representative solutions of the Pareto front, as well as the case of uncontrolled flow, are depicted in Fig. 74 with colored squares. The corresponding design variables and objective function values are reported in Table 11. Table 11 indicates that, for the optimal solutions considered, the decrease of flow unsteadiness is a result of the increase of the proportional gain value, k_p, as well as of the shift of the streamwise sensor location, x_s, farther downstream. For these representative solutions, Fig. 75 presents the computed signals of lift coefficient and slip length. As the control effort increases, the amplitude of the lift signal is reduced, reaching its minimal value at the solution depicted by Point 4 in Fig. 74; however flow unsteadiness is not fully suppressed.

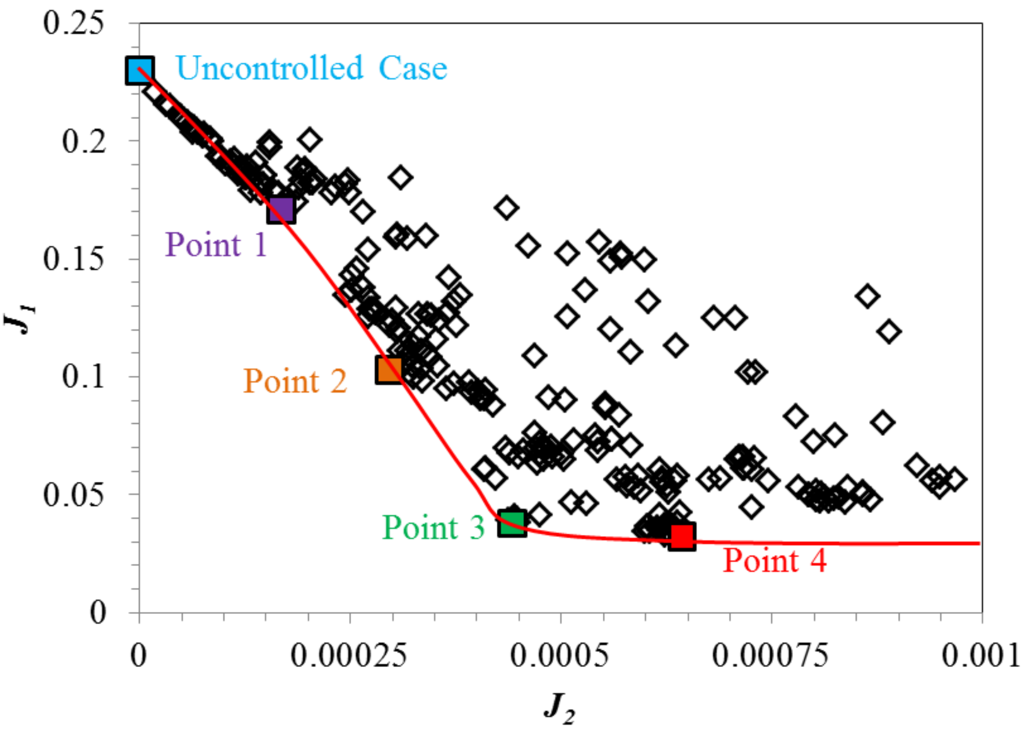

Fig. 74. *Re*=60: objective function J_1 vs. objective function J_2, and sketch of the corresponding Pareto front.

Table 11. *Re*=60: design variable values and corresponding objective function values, for the uncontrolled case, as well as for optimal solutions 1-4, depicted in Fig. 74.

Case	k_p	θ_{min}	θ_{max}	x_s	J_1	J_2
Uncontrolled	-	-	-	-	0.260	0.00000
Point 1	0.222	61°	125°	0.853	0.171	0.00017
Point 2	0.181	53°	120°	4.772	0.106	0.00031
Point 3	0.385	28°	127°	9.81	0.037	0.00044
Point 4	0.461	43°	167°	9.95	0.035	0.00064

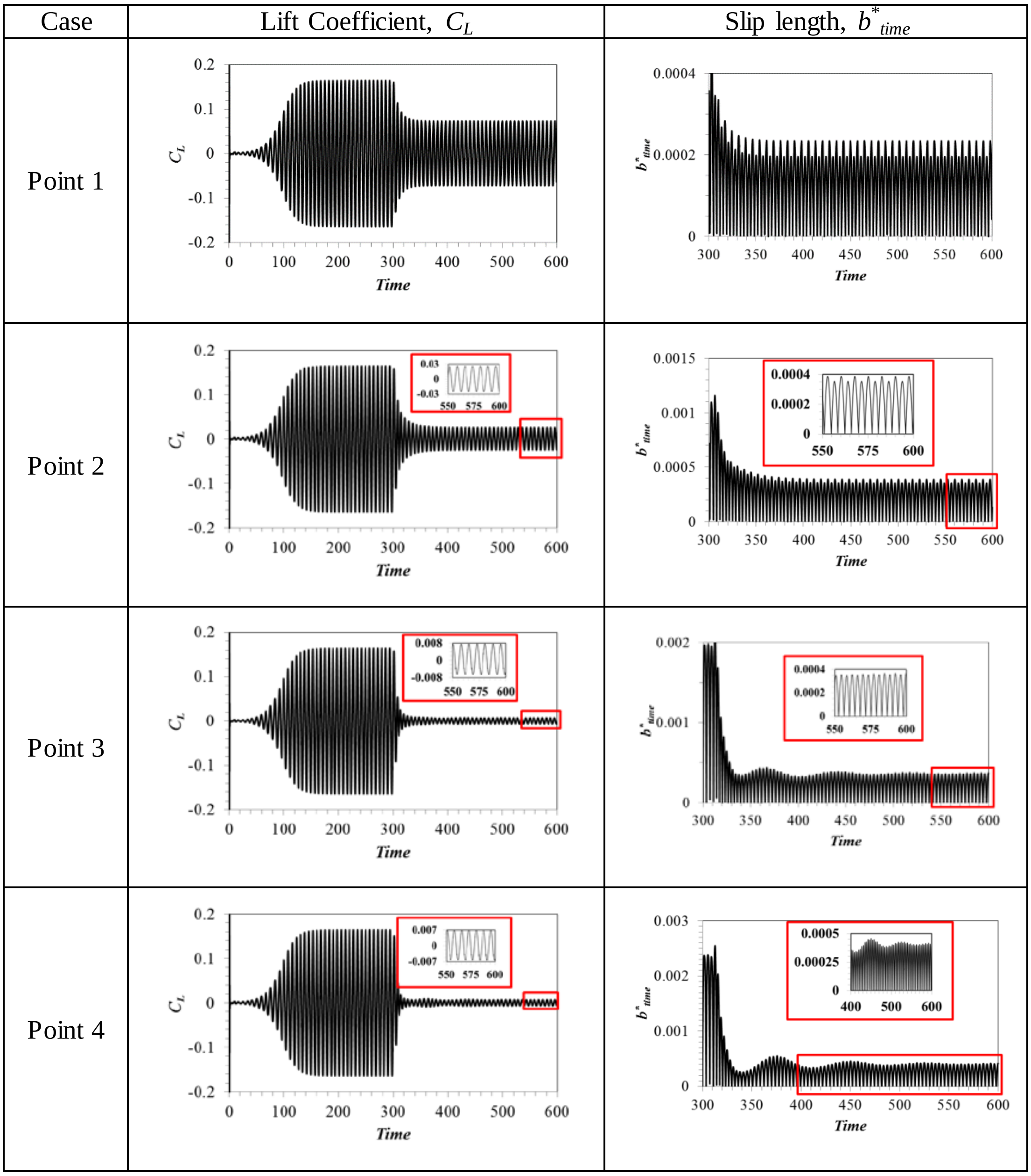

Fig. 75. *Re*=60: lift coefficient and slip length signals for optimal solutions 1-4, depicted in Fig. 74. Active feedback control in terms of time-dependent slip is implemented at *t*=300.

5.4.4.2 Optimization results for Re=90

Fig. 76 presents the computed values of objective functions for *Re*=90, accompanied by a sketch of the Pareto front. Two representative solutions, namely Point a and Point b, lying on the Pareto front, as well as the case of uncontrolled flow, are depicted in Fig. 76; the corresponding values of design variables and objective functions are reported in Table 12. Table 12 also includes passive control optimal solutions of the partial slip setup (Point 1 and Point 2 depicted in Fig. 24) presented in chapter 3; a solution corresponding to steady slip conditions on the entire cylinder surface (Legendre et al. 2009) is also reported. Table 11 indicates that, for the optimal solutions obtained for *Re*=90, the decrease of flow unsteadiness is mainly a result of the increase of the proportional gain value, k_p, and of the hydrophobic area, and secondarily of the shift of the sensor location, x_s, farther downstream. For these representative optimal solutions, Fig. 77 presents the computed signals of lift coefficient and slip length. It is demonstrated that, for the solution depicted by Point b in Fig. 76, the amplitude of lift signal attains a minimal value.

Finally, Table 12 highlights the fact that the control effort, also quantified by the product ½$b^*(\theta_{max}-\theta_{min})$ introduced in chapter 3, is reduced by more than two orders of magnitude, in comparison to the optimal solutions of the passive control scheme, i.e. flow unsteadiness is reduced substantially with very low levels of control effort. To interpret this important result, one should consider that, in the case of passive control, the control action is implemented on the non-linear flow state, which is characterized by self-sustained oscillations at high amplitudes. Thus, a high control effort is necessary. In the case of feedback flow control, the control action gradually brings the flow state close to a base flow state. The flow may thus exhibit low amplitude fluctuations with reference to this flow state; these fluctuations are controlled by the feedback control scheme implemented, using a corresponding (low) control effort.

As indicated in chapter 3, a realistic value of slip length with current superhydrophobic materials is of the order of 100 μm. The present results have shown that, in the case of implementing time-dependent slip conditions, an effective suppression of flow unsteadiness can be attained for b^*=0.0005 (or lower); this corresponds to cylinder diameters of about *D*=200 mm.

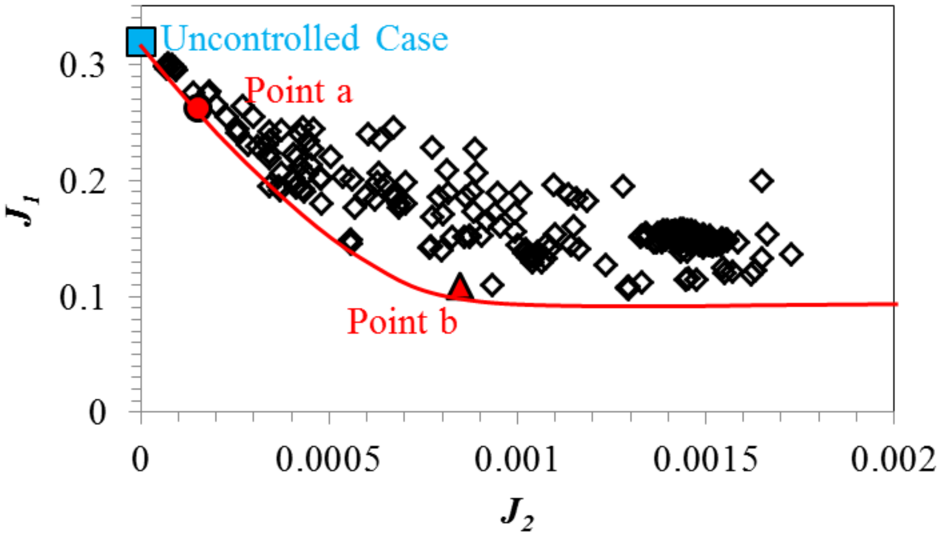

Fig. 76. *Re*=90: objective function J_1 vs. objective function J_2, and sketch of the corresponding Pareto front.

Table 12. *Re*=90: values of design variables and objective functions, for the uncontrolled case, for solutions depicted by Points a and b in Fig. 76, as well as for solutions corresponding to the passive control scheme, utilizing steady slip conditions on a part (Points 1 and 2 of Fig. 24) and on the entire cylinder surface (Legendre et al. 2009); the values of $½b^*\varphi$ magnitude, quantifying the control effort, are also reported.

Case	k_p	x_s	θ_{min}	θ_{max}	J_1	J_2	b^*	$\varphi=\theta_{max}-\theta_{min}$	$1/2b^*\varphi$
Uncontrolled	-	-	-	-	0.319	0.00000	0.00000	0^o	0.0000
Point a	0.043	8.2	56^o	119^o	0.261	0.00015	0.00018	63^o	0.0001
Point b	0.263	8.6	20^o	153^o	0.112	0.00085	0.00060	133^o	0.0007
Point 1	-	-	41^o	129^o	0.261	-	0.04100	88^o	0.0310
Point 2	-	-	34^o	146^o	0.112	-	0.19600	122^o	0.1560
b^*=0.15	-	-	0^o	180^o	0.112	-	0.15000	180^o	0.2350

Case	Lift Coefficient, C_L	Slip length, b^*_{time}
Point a	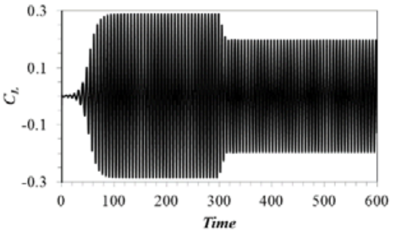	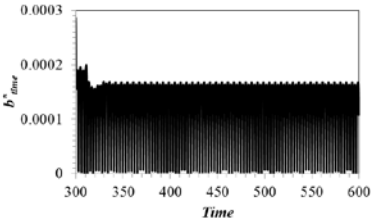
Point b	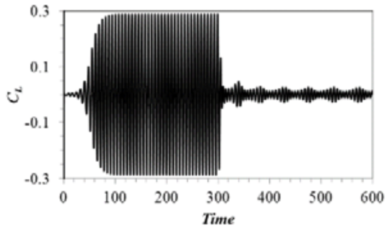	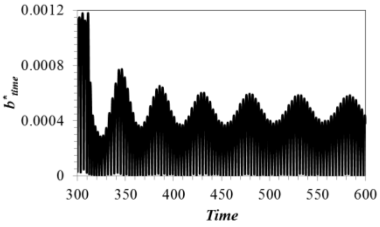

Fig. 77. *Re*=90: lift coefficient and slip length signals for solutions depicted in Fig. 78 by Point a and Point b. Active feedback control in terms of time-dependent slip is implemented at *t*=300.

5.5 Summary of chapter 5

The present chapter has addressed the problem of optimal suppression of the vortex street in flow past a cylinder at low Reynolds numbers, by means of two active feedback control schemes; for both schemes the feedback signal was obtained by a proportional control law based on the signal of a velocity sensor, properly placed in the near wake. In the first scheme, time-dependent mass transpiration was applied through two actuation slots on the cylinder surface. The optimization results have demonstrated the sensitivity of global flow stability to the choice of control parameters (proportional gain value, sensor location). In the frame of optimization, stabilization has been attained for a larger number of combinations of the control parameters, in comparison to the approach of Park et al (1994). In the second scheme, time-dependent slip conditions have been applied on the entire or on a part of the cylinder surface, as enabled by materials with controllable wettability properties. First, in the frame of a parametric study, application of controllable hydrophobicity on the entire cylinder surface has demonstrated that, by proper selection of the sensor location, as well as of the proportional gain value, the vortex street is effectively suppressed, leading to low levels of flow unsteadiness. Guided by these simulations, an optimization problem was formulated, aiming at suppressing the vortex street at a minimum control effort. The optimization results have demonstrated that vortex street can be suppressed using a control effort two orders of magnitude lower than that required in corresponding passive control schemes.

Chapter 6: Novelty of the present work and contribution to scientific research

The present computational study addresses the control of global stability in the prototype flow past a circular cylinder, for low Reynolds numbers, by optimizing passive, active open-loop and active feedback control schemes. A main novelty of the present work consists in proposing a systematic methodology for the optimal design of passive and active (both open-loop and feedback) flow control schemes, also including proper interpretation of results by means of stability analysis calculations. The present chapter summarizes the proposed methodology and the new findings of this thesis.

6.1 Proposed methodology

For each problem considered, the proposed methodology utilizes the following steps:

Step 1: Formulation of the CFD model
First, a computational model is developed, taking into account the parameters of the uncontrolled flow problem, as well as the parameters defining the control action. In the present study, implementation of a control strategy corresponds to a proper (steady or time-dependent) boundary condition on the cylinder surface. For each control scheme, spatial and temporal resolution tests guarantee grid- and time step independence.

Step 2: Parametric analysis
A parametric CFD analysis is performed in order to investigate the dependence of flow stability and the corresponding control effort on the control scheme parameters, and identify a proper range of the optimization problem design variables.

Step 3: Formulation and solution of multi-objective optimization problem
The goal of the present study is to attain partial or complete vortex street cancelation at a minimal control effort. To this end, for each control scheme considered, a multi-objective optimization problem is formulated and solved; the two optimization goals (vortex street cancelation and minimization of control effort) are quantified by proper objective functions. The solution of the optimization problems is achieved by coupling a CFD code (here ANSYS CFX) with an optimization code based on genetic algorithms. The solution of each optimization problem gives the set of optimal solutions (Pareto front).

Step 4: Characterization of optimal flow fields
Representative optimal solutions of the Pareto front (flow fields and force signals) are further processed, yielding flow statistics. These results are correlated to the intensity of flow unsteadiness and to the control effort.

Step 5: Local linear instability analysis of optimal solutions
For representative optimal solutions, local instability analysis of the corresponding base flow field is performed, utilizing a normal mode solver. Computed local absolute growth rates and frequencies are related to local values of velocity ratio and vorticity thickness, as well as to the results of non-linear CFD calculations.

Step 6: Calculation of global linear growth rates of optimal solutions

For representative optimal solutions, computed lift coefficient signals are processed in the frame of the Stuart-Landau equation, and results are related to those of non-linear CFD calculations.

6.2 New findings of the present thesis

The methodology outlined in the previous section has been applied in order to identify optimal solutions of four control schemes, in flow past a circular cylinder. The new findings for each control scheme can be summarized as follows:

(A) Passive control by means of steady hydrophobicity
The present thesis has demonstrated for the first time that implementation of hydrophobicity in both the front- and the rear stagnation point regime introduces destabilizing effects. This suggests that utilizing hydrophobicity in these areas should be avoided in flow stabilization schemes (use of partial slip), thus leading to a reduced cost in an actual implementation. Guided by this finding, a passive control scheme utilizing surface hydrophobicity on only a part of the cylinder surface has been implemented (partial hydrophobicity). The optimal extent of the hydrophobic regime on the cylinder surface has been identified for the first time by means of a systematic optimization procedure. The optimization results have highlighted a substantial decrease of the control effort in comparison to the full slip case, of up to 50%.

(B) Active feedback control by means of time-dependent hydrophobicity
In the present thesis, the use of materials exhibiting time-dependent wetting properties was considered for the first time for flow stabilization. Here, the specific time-dependent hydrophobicity of the (entire) cylinder surface has been regulated in the frame of a properly designed feedback control scheme, the parameters of which have been optimized. The optimization results have demonstrated that flow unsteadiness can be suppressed at a control effort reduced by two orders of magnitude, in comparison to the optimal implementation of steady hydrophobicity, a reduction which makes the proposed feedback control scheme attractive for future implementation in actual applications.

(C) Active open-loop control by means of steady mass transpiration
In the present thesis, the effects of implementing steady suction/blowing on three regimes of the cylinder surface (front stagnation point region, sideway region, and rear stagnation point region) have been systematically investigated for the first time. Guided by the results of the present investigation, a proper optimization problem was formulated and solved, imposing a zero net flow rate, associated with minimal pumping requirements. The optimization results give the full profile of mass transpiration on the cylinder surface, and demonstrate a decrease in control effort of up to nearly 50%, in comparison to previous literature studies.

(D) Active feedback control by means of time-dependent mass transpiration
A time-dependent mass transpiration control scheme utilizing feedback control has been implemented. For the first time, the control parameters have been identified by a systematic optimization study. The optimization results have demonstrated a significant reduction in control effort, in comparison to the optimal implementation of steady mass transpiration. Further, the present optimized schemes results in an improvement in robustness of literature feedback control schemes.

Chapter 7: Conclusions

7.1 Conclusions

The present work has investigated computationally the optimal suppression of the Kármán vortex street in flow past a circular cylinder at low Reynolds numbers (*Re*<180), by use of passive, active open-loop, and active feedback control schemes. To this end, a multi-objective optimization tool has been developed, by coupling a CFD code with an optimization tool based on genetic algorithms. Two control measures have been considered in the present work, in particular: (a) application of slip conditions, and (b) implementation of mass transpiration on the cylinder surface. The optimal results have been interepreted by means of local and global instability calculations utilizing an Orr-Sommerfeld solver, as well as force signal processing in the frame of the Stuart-Landau model.

First, the problem of passive control of flow past a circular cylinder has been investigated, by means of partial (and full) slip. It has been demonstrated that implementation of hydrophobicity in both the front- and the rear stagnation point regimes enhances destabilizing effects. Guided by this observation, an optimization problem was formulated aiming at partially or fully suppressing the Kármán vortex street at a minimum control effort, in terms of partial slip. Here, the control effort has been quantified as the product of the slip length and the extent of the hydrophobic regime. The optimization results have demonstrated that optimal application of partial slip is substantially more effective than full slip in suppressing flow unsteadiness. In particular, compared to full slip, optimal application of partial slip can result in a decrease of control effort by up to 50%. The local instability calculations of optimal solutions have demonstrated that the increase of the control effort results in decreased values of velocity ratio and vorticity thickness in the near wake region. Thus, both the streamwise extent of absolute instability and local absolute growth rates are decreased, leading to suppression of non-linear flow oscillations, and complete cancelation of the vortex street at a critical level of control effort.

Next, an active open-loop control scheme has been implemented by means of steady mass transpiration (suction/blowing) on the cylinder surface. Initially, suction/blowing has been applied in three regimes of the cylinder surface, namely: (a) the front stagnation point region, (b) the sideway region, and (c) the rear stagnation point region. The results have demonstrated that application of suction in the sideway or in the front stagnation point region, and blowing in the rear stagnation point region induce flow stabilization. Guided by these results, an optimization problem was formulated and solved, aiming at the partial or full suppression of the Kármán vortex street, at a minimal control effort, under the constraint of zero net mass transpiration. Here, the total control effort has been quantified by the suction coefficient, C_{suc}. Complete vortex street cancelation has been attained at a control effort 30% lower, in comparison to previous studies (Delaunay and Kaiktsis, 2001). The results of local instability analysis have shown a decrease in both the extent and intensity of local absolute instability with control effort (C_{suc}), resulting in stabilization of the global flow at a critical level of control effort.

Finally, in order to attain global flow stabilization at even lower levels of control effort two feedback control schemes have been developed and optimized, utilizing: (a) time-dependent mass transpiration, and (b) time-dependent slip conditions. For both schemes, the feedback signal has been obtained by a proportional control law based on the signal of a transverse velocity sensor, properly placed in the near wake, at a point on the domain centerline. In the first feedback scheme, time-dependent mass transpiration has been applied through two actuation slots on the cylinder surface. The optimization results have demonstrated the sensitivity of global flow stability to the choice of control parameters (proportional gain value, sensor location), whereas stabilization has been attained for a larger number of combinations of the control parameters, in comparison to the approach of Park et al. (1994). In the second feedback scheme, time-dependent slip conditions have been applied on the entire or on a part of the cylinder surface, by using materials with controllable wetting properties. The initial parametric study has demonstrated that implementation of controllable hydrophobicity on the entire cylinder surface may lead to low levels of flow unsteadiness; the latter has been attained by a proper selection of the control parameters. Guided by the results of the parametric study, an optimization problem was formulated, aiming at suppressing the vortex street at a minimal control effort. The optimization results have demonstrated that vortex street can be effectively suppressed utilizing a control effort lower by more than two orders of magnitude than that required in corresponding optimized passive control schemes.

7.2 Suggestions for future work

The present thesis has investigated computationally the control of flow past a cylinder at low Reynolds number values, by means of: (a) surface hydrophobicity, and (b) mass transpiration. In the present section, suggestions for future research that arise from the present study are proposed.

Firstly, concerning passive control by means of surface hydrophobicity, the present computational work can be extended to higher values of Reynolds number, for which the flow is three-dimensional. As three-dimensional computations are expected to be substantially more expensive, optimization should be as efficient as possible. To this end, hybrid optimization schemes, utilizing both genetic algorithms and gradient methods, as well as metamodels, can be implemented. In particular, regarding the use of partial slip, it should be investigated to what extent the results in terms of flow stabilization are superior in comparison to full slip (as has been demonstrated in the present thesis for low Reynolds numbers). In all cases, optimal computational solutions can be compared against experimental results, based, for example, on Particle Image Velocimetry (PIV).

Secondly, concerning active open-loop control by means of steady mass transpiration, the present computational work could also be extended to high Reynolds numbers, utilizing three-dimensional computations. Here, mass transpiration can depend on the spanwise direction, to account for the three-dimensionality of uncontrolled flow. The present scheme of a zero net flow rate can be maintained, to minimize pumping requirements. Optimal solutions should be compared against experiments.

Thirdly, the active control scheme utilizing materials with controllable wettability properties proposed in the present thesis should be elaborated on with experiments, both at low and high Reynolds numbers. The drastic reduction in control effort illustrated in the present work should be tested in an actual implementation.

Finally, it is noted that the systematic methodology for passive and active flow control proposed in the present thesis can be utilized to optimize control schemes in shear flow applications. For wake flows, in particular, such schemes can involve cylinder rotary oscillations, proper placement of control wires, and cylinder heating. In this context, it is also noted that the present approach, which has focused on flow stabilization, can be utilized to attain different control goals, such as maximizing heat transfer rates.

Appendix A: Validation tests of instability analysis calculations

A.1 Local linear instability analysis calculations

The local linear instability analysis calculations of the present study utilize an Orr-Sommerfeld solver based on high-order finite differences, developed by G.S. Triantafyllou (see Triantafyllou et al., 1986). The calculations are performed for wake profiles of the base (unperturbed flow), extending from $y=-10D$ to $y=+10D$; beyond these limits, the flow is found to be irrotational. Here, the present local instability analysis results are compared against published literature data. In particular, for an uncontrolled base flow at *Re*=90, local linear absolute frequency, St_0, and local linear absolute growth rate, $\omega_{0,i}$, where calculated for several streamwise locations of the cylinder wake, *x/D*. The results, presented in Fig. 79, are compared to those of Pier (2002), illustrating an overall very good agreement.

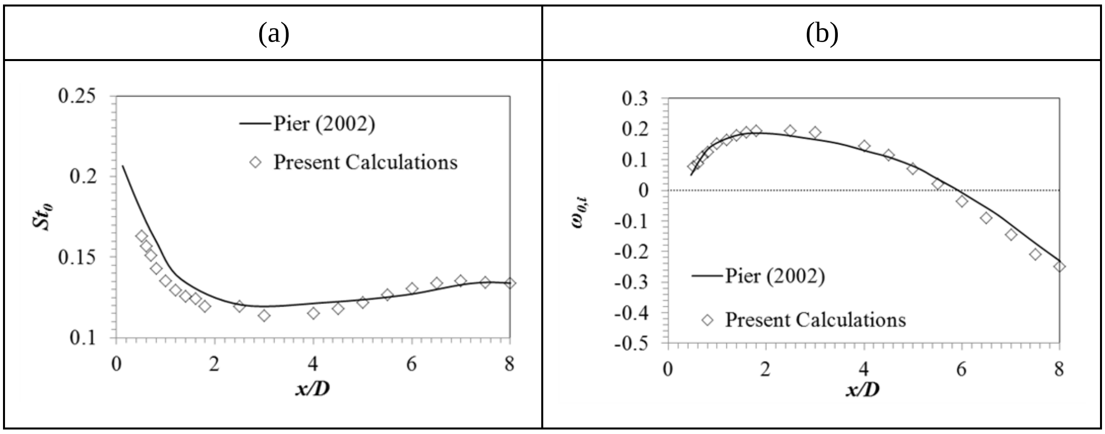

Fig. 78. *Re*=90: flow quantities vs. streamwise coordinate, for the base flow field of uncontrolled flow: (a) local linear absolute frequency, St_0, and (b) local linear absolute growth rate, $\omega_{0,i}$. The present results are compared against those of Pier (2002).

A.2 Calculations of global linear growth rates

Here, results of the present global linear growth rate calculations are reported for uncontrolled flow at *Re*=50 and *Re*=60 in Table 13. The results are compared to those of Schumm at al. (1994), and Delaunay and Kaiktsis (2001), demonstrating an overall very good agreement.

Table 13. Coefficients of the Stuart-Landau equation at *Re*=50 and *Re*=60, corresponding to the present (computational) and previous, experimental (Schumm at al., 1994) and computational (Delaunay and Kaiktsis, 2001) studies.

	Re=50	*Re*=60
$(\sigma_r D^2)/v$ (present work)	0.73	2.482
$(\sigma_r D^2)/v$ (Delaunay and Kaiktsis, 2001)	0.70	2.90
$(\sigma_r D^2)/v$ (Schumm et al., 1994)	0.69±0.08	2.80±0.1
$(\sigma_i D^2)/v$ (present work)	37.4	45.69
$(\sigma_i D^2)/v$ (Delaunay and Kaiktsis, 2001)	37.1	45
$(\sigma_i D^2)/v$ (Schumm et al., 1994)	35.7±0.6	42.1±0.8

References

1. Aamo OM, Krstic M. Flow Control by Feedback: Stabilization and Mixing 2003. Springer Science & Business Media.
2. Acrivos A, Leal LG, Snowden DD, Pan F. Further experiments on steady separated flows past bluff objects. J Fluid Mech 1968; 34 (01): 25–48.
3. Andreadis P, Zompanakis A, Chryssakis C, Kaiktsis L. Effects of the fuel injection parameters on the performance and emissions formation in a large-bore marine diesel engine. Int J Engine Res 2011; 12 (01).
4. Barkley D, Henderson RD. Three-dimensional Floquet stability analysis in the wake of a circular cylinder. J Fluid Mech 1996; 322: 215-241.
5. Bewley TR. Flow control: new challenges for a new renaissance 2001. Progress in Aerospace Sciences; 37: 21–58.
6. Braza M, Chassaing P, Minh H. Numerical study and physical analysis of the pressure and velocity fields in the near wake of a circular cylinder. J Fluid Mech 1986; 165: 79–130.
7. Cahon S, Melab N, Talbi EG. ParadisEO: A framework for the reusable design of parallel and distributed metaheuristics. J. Heuristics 2004; 10: 357–380.
8. Cattafesta N, Sheplak M. Actuators for active flow control. Ann Rev Fluid Mech 2011; 43 (1): 247–72.
9. Chen Z, Aubry N. Active control of cylinder wake. Communications in Nonlinear Science and Numerical Simulation 2003; 10: 205–216.
10. Choi H, Jeon W-P, Kim J. Control of flow over a bluff body. Ann Rev Fluid Mech 2008; 40:113–139.
11. Chomaz JM. Global instabilities in spatially developing flows: non-normality and nonlinearity. Ann Rev Fluid Mech 2005; 37 (1): 357–92.
12. Chomaz JM, Huerre P, Redekopp LG. The effect of nonlinearity and forcing on global modes. New Trends in Nonlinear Dynamics and Pattern-Forming Phenomena, edited by P. Coullet and P. Huerre (Plenum, New York, 1990), 259-274.
13. Deb K. Multi-objective optimization using evolutionary algorithms 2001, Chichester, U.K.: Wiley.
14. Deb K, Pratap A, Agarwal S, Meyarivan T. A fast and elitist multiobjective genetic algorithm: NSGA-II. IEEE Transactions on Evolutionary Computation 2002; 6: 182-197.
15. Delaunay Y, Kaiktsis L. Control of circular cylinder wakes using base mass transpiration. Phys Fluids 2001; 13(11): 3285–3302.
16. Dennis SCR, Chang GZ. Numerical solutions for steady flow past a circular cylinder at Reynolds numbers up to 100. J Fluid Mech 1970;42(03):471–89.
17. Dong S, Triantafyllou GS, Karniadakis GE (2008). Elimination of vortex streets in bluff-body flows. Physical Review Letters, 100, 20, 204501.
18. Drazin PG, Reid WH. Hydrodynamic stability 2004 2nd edition. Cambridge, UK ; New York: Cambridge University Press.
19. Evangelinos C, Karniadakis GE. Dynamics and flow structures in the turbulent wake of rigid and flexible cylinders subject to vortex-induced vibrations. J Fluid Mech 1999; 400: 91–124.
20. Fey U, König M, Eckelmann H. A new Strouhal–Reynolds number relationship for the Circular Cylinder in the Range 47<*Re*<2x105. Phys Fluids 1998; 10(7):1547
21. Fonseca CM, Fleming PJ. An overview of evolutionary algorithms in multiobjective optimization. Evol. Comput. 1995; 3:1–16.
22. Fornberg B. A numerical study of steady viscous flow past a circular cylinder. J Fluid Mech 1980; 98 (04): 819–55.

23. Fornberg B, Steady viscous flow past a circular cylinder up to Reynolds number 600. J Comp Phys 1985; 61: 297.
24. Fornberg B. Computing incompressible flows past blunt bodies - A historical overview. Numerical Methods for Fluid Dynamics (edited by Baines ML and Morton KW) 1993; 15.
25. Gad-el-Hak M. Flow control: passive, active, and reactive flow management 2007. Cambridge University Press.
26. Giannetti F, Luchini P. Structural sensitivity of the first instability of the cylinder wake." J Fluid Mech 2007; 581: 167–97.
27. Glezer A, Amitay M. Synthetic jets. Ann Rev Fluid Mech 2002; 34 (1): 503–29.
28. Green RB, Gerrard JH. Vorticity measurements in the near wake of a circular cylinder at low Reynolds numbers. J Fluid Mech 1993; 246: 675–91.
29. Hammache M, Gharib M.An experimental study of the parallel and oblique vortex shedding from circular cylinders. J Fluid Mech 1991; 232: 567.
30. Henderson RD. Details of the drag curve near the onset of vortex shedding. Phys. Fluids 1995; 7: 2102–2104.
31. Huerre P, PA Monkewitz. Local and global instabilities in spatially developing flows. Annu Rev Fluid Mech 1990; 22 (1):473–537.
32. Jackson CP. A finite-element study of the onset of vortex shedding in flow past variously shaped bodies. J Fluid Mech 1987; 182: 23–45.
33. Kaiktsis L, Triantafyllou GS, Özbas M. Excitation, inertia, and drag forces on a cylinder vibrating transversely to a steady flow. J Fluids and Structures 2007; 23:1–21.
34. Lecordier JC, Hamma L, and Paranthoen P. The control of vortex shedding behind heated circular cylinders at low Reynolds numbers. Exp Fluids 1991; 10: 224–229.
35. Lee SB, Baek SJ, Sung HJ. Feedback control of a circular cylinder wake with rotational oscillation. Fluid Dyn Res 2009; 41 (01): 011403.
36. Legendre D, Lauga E, Magnaudet J. Influence of slip on the dynamics of two-dimensional wakes. J Fluid Mech 2009; 633: 437–447.
37. Mathis C, Provansal M, Boyer L. The Benard-von Karman instability: an experimental study near the threshold. Phys Lett (Paris) 1984; 45: 483.
38. Milano M, Koumoutsakos P. A clustering genetic algorithm for cylinder drag optimization. J Comp Phys 2002; 175: 79–107.
39. Min C, Choi H. Suboptimal feedback control of vortex shedding at low Reynolds numbers. J Fluid Mech 1999; 401: 123–156.
40. Mittal S. Global linear stability analysis of time-averaged flows. Int J Num Meth Fluids 2008; 58 (1): 111–18.
41. Mittal S, Kumar B. Flow past a rotating cylinder. J Fluid Mech 2003; 476: 303–34.
42. Mittal S, Raghuvanshi A. Control of vortex shedding behind circular cylinder for flows at low Reynolds numbers. Int J Num Meth Fluids 2001; 35 (4): 421–447.
43. Monkewitz PA. The absolute and convective nature of instability in two-dimensional wakes at low Reynolds numbers. Phys. Fluids 1988; 31: 999–1006.
44. Monkewitz PA, Nguyen LN. Absolute instability in the near-wake of two-dimensional bluff bodies. J Fluids and Structures 1987; 1 (2): 165–84.
45. Mugele F, Baret JC. Electrowetting: From basics to applications. J Phys: Condens. Matter 2005; 17 (28): 705–74.
46. Muralidhar P, Ferrer N, Daniello R, and Rothstein JP. Influence of Slip on the Flow Past Superhydrophobic Circular Cylinders. J Fluid Mech 2011; 680: 459–476.
47. Park DS, Ladd DM, Hendricks EW. Feedback control of von Kármán vortex shedding behind a circular cylinder at low Reynolds numbers. Phys. Fluids 1994; 6: 2390–2405.
48. Pier B. On the frequency selection of finite-amplitude vortex shedding in the cylinder wake. J Fluid Mech 2002; 458: 407-417.

49. Pier B, Huerre P. Nonlinear self-sustained structures and fronts in spatially developing wake flows. J Fluid Mech 2001; 435: 145–74.
50. Provansal M, Mathis, Boyer L. Benard-von Karman instability: transient and forced regimes. J Fluid Mech 1987; 182: 1.
51. Rhie CM, Chow WL. Numerical study of the turbulent flow past an airfoil with trailing edge separation. AIAA Journal 1983; 21 (11): 1525–32.
52. Roshko A. On the wake and drag of bluff bodies. J Aerosp Sci 1955; 22: 124-132.
53. Roussopoulos K. Feedback control of vortex shedding at low Reynolds numbers. J Fluid Mech 1993; 248: 267–96.
54. Rothstein JP. Slip on superhydrophobic surfaces. Ann Rev Fluid Mech 2010; 41: 89-109.
55. Schmid PJ, Henningson DS. Stability and Transition in Shear Flows. Springer, 2001.
56. Schumm M, Berger E, Monkewitz PA. Self-excited oscillations in the wake of two-dimensional bluff bodies and their control. J. Fluid Mech 1994; 271, 17–53.
57. Seo IW, Song CG. Numerical simulation of laminar flow past a circular cylinder with slip conditions. Int J Num Meth in Fluids 2012; 68 (12): 1538–60.
58. Strouhal V. Über eine besondere Art der Tonerregung', Annalen der Physik und Chemie 1878 Bd. 5 Nr. 9.
59. Strykowski PJ, Sreenivasan KR. On the formation and suppression of vortex 'shedding' at low Reynolds numbers. J Fluid Mech 1990; 218: 71-107.
60. Takami H, Keller, H, Steady two-dimensional viscous flow of an incompressible fluid past a circular cylinder. Phys. Fluids 1969; 12: II–51.
61. Tan KC, Khor EF, Lee TH. Multiobjective evolutionary algorithms and applications 2005; Springer Verlag, London.
62. Tokumaru PT, Dimotakis PE. Rotary oscillation control of a cylinder wake. J Fluid Mech 1991; 224: 77–90.
63. Tokumaru PT, Dimotakis PE. The lift of a cylinder executing rotary motions in a uniform flow. J Fluid Mech 1993; 255: 1-10.
64. Triantafyllou GS, Triantafyllou MS, Chryssostomidis C. On the formation of vortex streets behind stationary cylinders.J Fluid Mech 1986; 170: 461–77.
65. Tritton DJ. Experiments on the flow past a circular cylinder at low Reynolds numbers. J Fluid Mech 1959; 6 (04): 547–67.
66. Twiss RQ. Propagation in electron-ion streams. Physical Review 1952; 88 (6): 1392–1407.
67. Verplanck N, Coffinier Y, Thomy V, Boukherroub R. Wettability switching techniques on superhydrophobic surfaces. Nanoscale Res Lett 2007; 12: 577.
68. Von Karman T. Über den mechanismus des widerstandes, den ein bewegter körper in einer flüssigkeit erfährt. Göttingen Nachrichten, Mathematische Physikalische Klasse 1911; 509.
69. Williamson CHK. Vortex dynamics in the cylinder wake. Annu Rev Fluid Mech 1996; 28 (1): 477–539.
70. Wood CJ. The effect of base bleed on a periodic wake. J R Aero Soc 1964; 68: 177.
71. Wu MH, Wen CY, Yen RH, Weng MC, Wang AB. experimental and numerical study of the separation angle for flow around a circular cylinder at low Reynolds number. J Fluid Mech 2004; 515: 233–60.
72. Yildirim I, Rindt CCM, Steenhoven AA. Vortex dynamics in a wire-disturbed cylinder wake. Phys Fluids 2010; 22 (9): 094101.
73. You D, Moin P. Effects of Hydrophobic Surfaces on the Drag and Lift of a Circular Cylinder. Phys Fluids 2007; 31(8):08170.
74. Zebib A. Stability of viscous flow past a circular cylinder. Journal of Engineering Mathematics 1987; 21 (2): 155–65.
75. Zhang, WM, Meng G, Wei X. A review on slip models for gas microflows. Microfluidics and Nanofluidics 2012; 13(6):845–882.